Micromechanical characterization of heterogeneous materials, statistical analysis of nanoindentation data

Zur Erlangung des akademischen Grades einer
DOKTORIN DER INGENIEURWISSENSCHAFTEN
(Dr.-Ing.)

von der KIT-Fakultät für Maschinenbau des
Karlsruher Instituts für Technologie (KIT)

angenommene
DISSERTATION

von

M. Sc. Clémence Bos

Tag der mündlichen Prüfung:	18. April 2019
Referent:	Prof. Dr. Oliver Kraft
Korreferent:	Prof. Dr. Erica Lilleodden

Kurzfassung

Um aktuellen und zukünftigen Herausforderungen gerecht zu werden, steigen die Anforderungen an Effizienz, Leichtigkeit und Umweltfreundlichkeit industrieller Bauteile. Neue Bauteile bestehen immer öfter aus komplexen Werkstoffen wie Legierungen, Verbundwerkstoffe oder Werkstoffverbunde. Diese komplexen Werkstoffe müssen charakterisiert werden, unter anderem auf der Ebene der Heterogenität. Auch bestehende Werkstoffe müssen genauer untersucht werden, damit sie effizienter eingesetzt werden können. Die Struktur heterogener Werkstoffe und ihrer mechanischen Eigenschaften auf unterschiedlichen Längenskalen müssen immer genauer verstanden werden. Die registrierende Härtemessung (die sog. Nanoindentation) ist eine gängige Methode für die mechanische Charakterisierung von Werkstoffen auf der Mikrometer- bis Nanometer-Skala. Gekoppelt mit einer statistischen Analyse kann die Nanoindentation wertvolle Informationen über die Mikrostruktur und Eigenschaften heterogener Werkstoffe liefern, beispielsweise die Anzahl der Phasen in hydrierter Zementpaste, die Eigenschaften der Phasen sowie die Phasenanteile.

In dieser Arbeit werden verschiedene heterogene Werkstoffe untersucht, die zu unterschiedlichen Materialklassen gehören: Haftpads der Kletterpflanze *Passiflora discophora*, Metallverbunde aus Kupfer und Chrom sowie verschiedene Mischungen von Polymer und Zementpasten (kurz: Mörtel und polymer-modifizierter Zement).

Diese Arbeit soll die Anwendbarkeit einer statistischen Methode auf Nanoindentationsergebnisse verschiedener Werkstoffklassen untersuchen. Sie soll auch bestimmen helfen, unter welcher Bedingungen Fits einer großen An-

zahl experimenteller Datenpunkte aus der Nanoindentation (mit z.B. bis zu 10^3–10^4 Indents) Auskunft über die Werkstoffphasen und ihrer Eigenschaften geben können.
Es werden zuerst zwei Metallverbunde aus Kupfer und Chrom untersucht, um die Anwendbarkeit der statistische Analysemethode von Nanoindentationsdaten heterogener Werkstoffe anhand eines Modellwerkstoffes zu überprüfen. Dann wird diese statistische Methode auf verschiedene Werkstoffe angewendet. Dabei werden die Rolle der heterogenen Mikrostruktur des Haftpads für seine Hafteigenschaften diskutiert, die mechanische Alterung von verschiedenen Mörteln sowie der Einfluss der Polymerart und seinem Anteil auf die gesamte Elastizität verschiedener polymer-modifizierten Zementpasten.
Zum Schluss werden einige Empfehlungen zur Anwendung der untersuchten statistischen Analyse von Nanoindentationsdaten geäußert. Ein kritischer Parameter ist die Eindringtiefe, weil sie sowohl von der Materialmikrostruktur, als auch von den Phaseneigenschaften und von der Qualität der Oberfläche abhängt. Darüber hinaus sollen die einzelnen Phasen ausreichend vertreten sein, sodass in der nachfolgenden statistischen Analyse die Eigenschaften jeder Phase mit hoher Genauigkeit aufgelöst werden können. Auch der Einfluss der ausgewählten Modelle soll überprüft werden, wobei das Bayes-Informationskriterium (BIC) empfohlen wird, um nicht nur Fits, sondern auch Fit-Modelle, miteinander zu vergleichen.

Abstract

To meet current and future challenges, industrial components are aiming for more efficiency and more environmental friendliness. Thus, new components increasingly consist of heterogeneous materials at microscopic to mesoscopic scales, such as complex alloys, composites or combinations of materials. These materials must be characterized, also at the scale of the heterogeneity, to improve the understanding of their structure on different length scales and use them more efficiently.

Instrumented indentation (or nanoindentation) is a testing method widely used for the mechanical characterization of materials from the micrometer to the nanometer scale. Nanoindentation in combination with statistical methods can provide valuable information regarding the microstructure and properties of heterogeneous materials, for example the number of phases in hydrated cement paste, as well as the phase properties and the phase fractions.

This work aims to determine the best conditions under which fits of large numbers of nanoindentation data points (typ. up to 10^3–10^4 indents) can provide information about the material phases and their properties.

Selected heterogeneous materials of various material classes are investigated: two copper-chromium composites, attachment pads of the climbing passionflower *Passiflora discophora* and different combinations of polymer and cement pastes, i.e. mortars and polymer-modified cement pastes.

First, the copper-chromium samples are used as a model material to investigate the applicability of the statistical analysis methods for nanoindentation data of heterogeneous materials. Then, the role of the heterogeneous

microstructure of the attachment pads on their attachment properties are discussed, as well as the mechanical aging of a mortar paste and the influence of the polymer's type and concentration on the phases of polymer-modified cement pastes.
Finally, some recommendations for using statistical methods on nanoindentation data are made. For such experiments, the indentation depth must be chosen carefully in order to distinguish between the properties of the different phases and minimize the influence of the surface roughness. Also, the total number of data points must be large enough so that each phase is sufficiently represented in the experimental distribution, and its properties can be accurately resolved in the following statistical analysis. Last but not least, the influence of the selected fitting model must be analyzed. The Bayes Information Criterion (BIC) is recommended to compare fitting models and fit results with each other.

Acknowledgement

This work was conducted between 2013 and 2016 at the Institute for Advanced Materials - Materials and Biomechanics (IAM-WBM) at the Karlsruhe Institute of Technology (KIT) in Germany. I would like to thank all colleagues and friends that helped me during that time, and in particular:

- Prof. Dr. Oliver Kraft for the possibility to conduct this research at his institute, as well as the various conferences and on-the-job training I could attend throughout my work as PhD student.
- The German Federal Ministry of Education and Research (BMBF) which partly funded this project under the contract 03X3587, Project "BioLast".
- Dr. Ruth Schwaiger for the support, regular discussions and the very thorough proof-reading.
- Dr. Joachim Schätzle and Dr. Feng Zhu from fischerwerke GmbH, not only for the various mortar samples and production kits and the visits of the production and development sites in Waldachtal, but mostly for their curiosity for my research topics and the great cooperation.
- Prof. Dr. Thomas Speck, Dr. Holger Bohn and Mrs. Stefanie Schmier from the Plant Biomechanics Group of Freiburg's University for the *Passiflora discophora* samples and the lending of the microtome. I also thank you very much for the close and very friendly cooperation regarding the microstructure and biomechanics of the pads.

- Mrs. Luise Göbel from the F. A. Finger-Institute for Building Materials of the Weimar Bauhaus-University for the nice cooperation on the polymer-modified cement pastes, which extended nicely the range of materials I investigated. I wish you best luck for the rest of your PhD.

- Dr. Heinz Riesch-Oppermann for the help on mathematical topics, in particular Bayesian probabilities.

- Dr. Roland Kappel for the great FE simulations of the pads elastic deformations and the related discussions.

- Mr. Ewald Ernst for the technical support throughout these three years, and most of all for building the long-term loading apparatus for mortar aging experiments, and Mrs. Daniela Exner for all the materialographic help.

- All former and current colleagues of the IAM-WBM. I enjoyed very much the long discussions, the birthday cakes, the hat building events, the conferences and the support on more or less research-related topics. Mr Tobias Neuhauser and Adrian Epprecht for having conducting some experiments for me, in particular with the aging investigations on mortar samples.

- Mrs. Jana Herzog for the friendly talks and the great everyday help.

- My friends from the shared flat in Karlsruhe for the nice living environment, the community life, the open-mindedness and the support.

- My friends Cloé and Constance, my grand-parents, my parents and siblings, and of course Jakob, for their love and support.

Contents

List of Symbols and Abbreviations

Symbols

A	Contact area	m^2
b	Width of a bin in the PDF representation of the Young's modulus or hardness	Pa
D	Characteristic size of heterogeneities	m
E	Young's modulus	Pa
F	Force	N
f	Surface fraction	–
H	Hardness	Pa
h	Indentation depth	m
K	Stiffness	N/m
k	Number of fitting parameters	–
$\hat{L}$	Likelihood of the fitting function with optimized parameters	–
l	Testing length scale	m
M	Mass of indenter	Pa
m	Mean value of a phase	Pa
$\mathcal{N}$	Normal (Gaussian) function	
$\tilde{N}$	Number of phases, equal to n or $\tilde{n}$, depending on the investigated property	–
$\tilde{n}$	Phase number from the hardness distribution	–
N	Number of (valid) indents	–
n	Phase number from the Young's modulus distribution	–
P	Force in indentation context	N

r	Coefficient of determination	–
R_q	Surface roughness	
S	Contact stiffness	N/m
s	Standard deviation	
T	Sample age	d
t	Time	s
w	Uncertainty factor in the ODR fitting procedure	$1/\mathrm{Pa}^2$
$\tilde{X}$	Mean value of a bin in the PDF representation of the property X, either E or H	Pa
x	Longitudinal direction in cartesian coordinate system	m
Y	Yield strength	Pa
y	Transversal direction in cartesian coordinate system	m
z	Vertical direction in cartesian coordinate system	m
γ	Shear strain	–
Δ	Experimental error	
δ	Distance between the empirical and the fitting distributions	–
ν	Poisson's ratio	–
σ	Stress	Pa
τ	Shear stress	Pa
χ^2	Goodness-of-fit parameter	–
Ψ	Phase angle	rad
ω	Angular frequency	rad/s

Indices

0	Initial value, reference
$1/2$	Half time
a	Adjusted

as	Assumed
c	Contact
eq	Equivalent
f	Frame
fit	Fitting function
i	Phase index
in	Indenter
j	Data point index
k	Bin index
l	Loss
max	Maximum
min	Minimum
os	Oscillation
p	Projected
q	Number of bins in PDF representation
r	Reduced
sp	Spring
st	Storage
t	Indenter tip
u	Unloading
X	Property X

Constants

a	Adjustment factor
β	Factor depending on tip geometry
ε	Factor

Abbreviations

AFM	Atomic Force Microscopy
AIC	Akaike Information Criterion
BIC	Bayesian Information Criterion

BSE	Back-Scattered Electron
C-S-H	Calcium Silicate Hydrates
CDF	Cumulative Distribution Frequency
CH	Calcium Hydroxide
CS	Cross Section
CSM	Continuous Stiffness Measurement
DMA	Dynamic Mechanical Analysis
DOF	Degrees of Freedom
ECD	Equivalent Circle Diameter
EDF	Empirical Distribution Frequency
EDX	Energy-Dispersive X-ray spectroscopy
EM	Expectation Maximization
ET	Express Test
FAST	Field Assisted Sintering Technique
FE	Finite Element
FEM	Finite-Element Modeling
FGM	Functionally Graded Materials
FIB	Focused Ion Beam
GUI	Graphical User Interface
HD	High Density
ISE	Indentation Size Effect
LD	Low Density
LM	Levenberg-Macquardt
LSE	Least Square Estimation
MFFT	Minimal Film Forming Temperature
MLE	Maximum Likelihood Estimation
MMC	Metal-Matrix Composite
ODR	Orthogonal Distance Regression
OLE	Object Linking and Embedding
P:C	Polymer-to-Cement ratio
PCC	Polymer-Modified Concretes

PDF	Probability Density Function
PMC	Polymer-Modified Cement paste
RMS	Root-Mean-Square
RSS	Residual Sum of Squares
RVE	Representative Volume Element
SA	Styrene Acrylic acid ester copolymer
SBR	Styrene-Butadiene copolymer
SEM	Scanning Electron Microscopy
SNI	Statistical Nanoindentation
SNT	Statistical Nanoindentation Technique
TEM	Transmission Electron Microscopy
W:C	Water-to-Cement ratio
XRD	X-Ray Diffraction
μ-CT	Micro Computed Tomography

Mathematical functions

erf	Error function
exp	Exponential function
rand	Random function

1 Introduction

Heterogeneous materials are of major importance in technological applications nowadays. Well-known examples of heterogeneous materials are composites, which typically exhibit high stiffness-to-weight ratios. Also, biological materials and living organisms consist of complex, hierarchical structures, which represent evolutionary advantages regarding their mechanical properties. In general, interfaces and interphases play a key role in various mechanical systems.

The instrumented indentation testing, at the smallest scale also called nanoindentation, has been proven a suitable tool for the micromechanical characterization of various materials. Typically, a series of tests are performed on a material, and a mean value and standard deviation of the property of interest are calculated. For heterogeneous materials, however, one mean value and standard deviation are not enough to describe the material with sufficient resolution. A statistical analysis of the distribution of the measured property can lead to a more accurate and realistic description of the material's mechanical properties. Probabilistic methods enable the calculation of the different phase proportions and a material's mechanical characterization.

The goal of this research is to evaluate the applicability of the statistical nanoindentation technique to the different classes of materials. Furthermore, a method for the characterization of the mechanical properties of heterogeneous materials at the micrometer scale using nanoindentation and probabilistics-based criteria has been developed and its applicability to a heterogeneous sample with simple two-phase microstructure has been investigated, based on the example of Cu-Cr composites of different weight

ratios. The method has been applied to understand the effect of the internal structure on the mechanical function of attachment pads of a climbing plant, to describe the aging of mortar, and to quantify the role of polymer additions in cement pastes. Finally, the capabilities of the method in particular in application to the different material classes will be discussed.

After a literature review part, which gives insight into heterogeneous materials, their mechanical testing via nanoindentation, and the Statistical Nanoindentation Technique, the applicability of the method to Cu-Cr composites is discussed.

Then, three application parts follow, each focusing on a different type of material. In the first part, attachment pads of the passionflower *Passiflora discophora* are studied, in order to understand the role of the microstructure on their attachment properties. The second part aims at determining the role of different microscopic phases of a commercially available mortar used in building anchors. The third part evaluates the role of the polymer for the mechanical properties of polymer-modified cement-based materials.

To conclude, the applicability of the statistical nanoindentation method to the different material classes is discussed and some open questions are raised.

For more details on the statistical nanoindentation technique, a study in the appendix compares different variations of the methods, such as the fitting procedures or the influence of fundamental parameters, to identify the critical parameters.

2 State of the art

2.1 Heterogeneous materials

Heterogeneous derives from Greek *heterogenes*, itself coming from *heteros*, the other of two, the other, the different, and *-genes*, which means "born, kind". The final *-ous*, means "full of". Thus heterogeneous materials are, literally, "full of, per nature different, components". Heterogeneity is often defined as the contrary of homogeneity. In physics, heterogeneity characterizes media having properties that vary with the investigated location, as the medium is being made of "dissimilar or diverse ingredients or constituents"[1]. Engineering composites are well-known examples of heterogeneous materials and typically possess a well-defined microstructure. Other heterogeneous materials used on a daily basis, such as concrete and mortars, however, do not possess a well-defined microstructure, i.e. the location of the different constituents within the material is random and varies with the sample and possibly also the age or the environmental conditions.

A heterogeneous microstructure complexifies the characterization of a material's mechanical behavior at the different length scales. Indeed, the complexity of mechanical testing depends on the testing length scale l with respect to the characteristic size of the heterogeneity D. When the heterogeneity is much smaller than the testing length scale, i.e. $l \gg D$, the material is then characterized in the same way as a homogeneous material and the role of the heterogeneities is neglected. However, some applications and simulations require the knowledge of the mechanical properties at a much

[1] See Merriam-Webster, *Heterogeneous*, `https://www.merriam-webster.com/dictionary/heterogeneous`, visited on 10th March 2018.

smaller scale, which may be similar or even smaller than the typical size of the heterogeneity, i.e. $l \approx D$, $l < D$ or even $l \ll D$ [1]. At these length scales, the mechanical properties determination is influenced by the local microstructure, and the local variations in the composition, microstructure or mechanical properties cannot be neglected.
In the following, the characteristics of the different classes of heterogeneous materials are presented, with focus on properties relevant for their mechanical behavior. Among them, attention is focused on heterogeneous metal-based materials and composites, then biological materials, and finally hydrated cement-based materials, also mixed with various polymers.

2.1.1 Metal-based materials and composites

Composites are a combination of two or more materials designed to fulfill certain requirements, which monolithic, bulk materials cannot fulfill. In case of metal-matrix composites (MMC), the second material is often a ceramic or a polymer. The material combination differs according to the purpose and the use case of the composite component. The mechanical reinforcing phase can be shaped as fibers, particles, or filaments, and is selected to improve a certain mechanical property, such as the yield strength, tensile strength, creep or fatigue resistance. The reinforcing phase should also enable the composite to maintain a minimum ductility or toughness. The aim of using composites may be to decrease the total weight of materials used in the engineered system [2]. Typical reinforcement materials, for example, for aluminum and magnesium-based matrices are Al_2O_3, SiC, C, B_4C and B, all of them having different crystal structures and shapes [2, 3]. Some applications include turbine blades, brake discs, piston and frames in the automotive, aeronautical and aerospace industries, as well as carbon brushes, electrical contacts and electrodes in the electrical industry [2].
Composites can also be used to take advantage of mechanical size effects. In particular, ceramics are known to be tougher when micrometer-sized than

as bulk component [3], or "the flow stress of a ceramic particle-reinforced metal-matrix composite is observed to increase with decreasing particle size for particles in the micron size range, all other factors such as particle volume fraction being held constant" [4]. Thus, new MMCs tend to contain sub-micrometer to nanosized particles instead of large, long fibers. However, the decrease in size of one or more material phases in the composites leads to some challenges. First, the mechanical properties of each individual phase must be known to design the composites according to the requirements. Thus, the sub-micrometer to nanosized materials must be tested. It may also be interesting to test each composite phase individually within the composite. Therefore, mechanical testing methods with an adequate resolution in stress and strain as well as positioning resolution are needed.

Besides composites, heterogeneous metal-based materials also include thin films, metallic multi-layers, and Functionally Graded Materials (FGM). Thin films are primarily used in electronics to shrink "the feature size in integrated circuit technology", and thus improve the overall capacity of electronics components [5]. Besides electrical properties, stress and deformation processes in thin films on substrates have to be investigated. Decreasing film thickness leads to changes in the mechanical properties of the film compared to the those of the bulk material, which is known as mechanical size effect. For example, the deformation mechanisms may change with the decreasing device size [6], which is accompanied by a growing influence of residual, thermal and surface stresses on the mechanical behavior.

Furthermore, the strength of a metal is known to increase with a decreasing grain size or layer thickness [7]. In general, the Hall-Petch model [8, 9] describes the strength increase with decreasing microstructural length scale. It is based on the principle that both grain or interface boundaries act as barriers for the dislocations, i.e. dislocations pile-up at the interfaces and at the grain boundaries. Dislocations move into adjacent grains, when the shear stress at the head of a pile-up reaches some threshold value. The applied stress is proportional to $h^{-1/2}$ with h as the layer thickness in case of a polycrystalline

thin film [7] and to $d^{-1/2}$ with d as the mean grain size diameter [10]. Thus, the measured hardness also increases with decreasing grain size diameter.
The small dimensions of thin films require high resolution mechanical testing methods to obtain an adequate understanding of a film's mechanical behavior. Two special cases of thin films are multi-layers, which are stacks of two different metals, and Functionally Graded Materials (FGM). Multi-layers are studied because of their high strength as well as their electrical, magnetic and optical properties [7]. FGM are similar to thin films, but exhibit a smooth transition of the film and substrate properties instead of the typically abrupt change at the interface between film and substrate [11]. A gradient in properties aims at reducing, e.g., the residual stresses of a film/substrate system, when the thermo-physical properties have a large mismatch, as in a W/Fe FGM. In this particular FGM, the hardness H varies with the testing position along the material gradient and is reduced for smaller W contents [11]. Indentation testing with high resolution to characterize the elastic and elasto-plastic properties of the graded material could help to understand the advantages of FGM, and to further improve their design [12].

2.1.2 Heterogeneity of biological materials and attachment systems

Heterogeneity plays a major role in biological materials. Indeed, only a few constituents are available as building blocks in biological systems. However, the diversity of combinations of these constituents at different length scales enables the natural diversity of biological materials and is a great source of inspiration for the design of new materials and structures [13]. Prominent examples of heterogeneous biological materials are teeth and bone [14–16], shells, nacre and carapaces [13, 15, 17], butterfly wings [15], as well as wood and plant tissues [16, 18].
Biological attachment systems are of great interest to researchers and engineers, as they have significant potential for biomimetics and bioinspiration.

For example, the adhesion principles of barnacles, which can adhere under water [19], or gecko toes with their hierarchical setae structure [20], were investigated with the goal of developing new adhesives and attachment devices. The attachment strategies found in nature can be divided based on their physical principles, their functionalities, and their contact timescales [21].

Climbing plants exhibit a variety of techniques facilitating permanent attachment. The development of specialized organs, as for example in English ivy (*Hedera helix*), enables the plant to grow and climb on flat, vertical surfaces [22]. Thus they are independent of the support diameter, which limits the growth of twining plants and lianas [23]. The attachment pad of the climbing passionflower *P. discophora* exhibits a heterogeneous microstructure with at least three different tissue types [24]. Also in Boston ivy (*Parthenocissus tricuspidata*), different tissues, some being lignified, others unlignified, were found [25].

First attempts to understand the structure-property relationship of Boston ivy attachment pads used tensile tests on the whole attachment organ [26]. It was found that dry, lignified pads of *P. tricuspidata* have an attachment strength more than four times as large as the one of young, fresh attachment pads. More recently, lignified attachment pads of *Passiflora discophora* were tested with a micro-tensile apparatus, which revealed the strong attachment of the pad to the substrate [27]. Characterizing the mechanical properties of attachment pads, and more generally, biological materials, at a microscopic length scale may enable a deeper understanding of the microstructure-function relationship.

2.1.3 Hardened cement paste

Hardened cement paste can be described as “a 3D disordered material composed of a number of different phases” [28]. Also, “the microstructure of hydrated Portland cement pastes varies considerably with such factors as the

chemistry and fineness of the cement used, the water-to-cement ratio, the use of chemical admixtures, variations in mixing procedures, differences in early curing temperatures, and variations in hydration conditions. Nevertheless, most cement pastes show common features" [29]. With the development of new investigative methods, such as Transmission Electron Microscopy (TEM), Scanning Electron Microscopy (SEM) or Focused Ion Beam (FIB) nanotomography, the possibilities of microstructure investigation of cement-based materials have improved during the late 20th century [30, 31]. In the beginning of the 21st century, Diamond [29] qualitatively analyzed the microstructure of hardened cement paste with SEM and energy-dispersive X-ray spectroscopy (EDX) analysis. Numerous phases were identified, the most significant ones being unhydrated cement paste particles, calcium silicate hydrates (C-S-H) gel, itself being composed of two phases of different densities, and calcium hydroxide (CH). Large pores ($>$200 nm) were also observed [29], which influence the strength of the cement-based material [32]. The smaller pores are of great importance for the material's properties, as they can be related to the paste's degree of hydration and creep properties [32]. In particular, the C-S-H phase exhibits a complex structure at the nanometer scale [31]. "C-S-H has porosity at length scales down to about 1 nm" [32]. However, there is no consensus on the cement paste microstructure and in particular the microstructure of the C-S-H gel [28, 29, 33–36], but on the presence of at least two different C-S-H phases, a low density (LD C-S-H) and a high density (HD C-S-H) phase [37].

Cement pastes harden through kinetically controlled hydration reactions. Thus the material and its mechanical properties not only change with the investigated location, but also change with time and the environmental condition: the material ages. Studying Young's modulus and strength of cement pastes during setting and hardening has shown that Young's modulus is more sensitive to "the connection between particles, whereas strength is more sensitive to the pore filling" [38].

2.1.4 Polymer-modified cement-based materials

Besides hydrated cement pastes, also cement-based materials with polymer additives show a heterogeneous microstructure. Among them, polymer-modified concrete and mortar were developed “as repair materials for deteriorated reinforced concrete structure” [39]. Their development aimed in particular at improving or modifying the duration of the hardening reaction, mechanical properties, chemical resistance, durability and waterproof performance [40]. An adhesion increase or a reduction of the drying shrinkage compared to that of the unmodified materials were sought [39, 41, 42]. Applications include repair and overlays [43]. But the field of applications seems to be still not fully explored [43–45]. Polymer-modified cement pastes (PMC) should be distinguished from polymer-cement composites, in which the polymer is used as fiber or mesh to reinforce the cementitious, inorganic matrix [46]. The PMCs rather consist of “two interpenetrating matrices” [46], as the polymerization of the dispersed monomer and the hydration reaction of the cement paste happen in parallel and potentially interact.
Various polymers can be used, which are classified by chemical composition, water-solubility properties and condition (powder or solution/emulsion) [41, 47]. Two different composite mechanisms are brought up by Sakai et al. [47] in the early stages of microstructural characterization of PMC, “the particle dispersion of polymer and the formation of polymer films”. Considering the microstructure of PMC, the delivery form of the polymer, the polymer additives and the polymer-to-cement ratio (P:C) seem to play a major role in the polymer adsorption by the inorganic matrix, in the polymer film formation around the cement particles, in the delay of the hydration reactions and for the resulting properties [42, 48]. Concerning the modification of the mechanical properties due to the polymer, a decrease in the compressive strength and Young’s modulus has been observed in PMCs, in particular for P:C ratio larger than 2 % [42, 49–51]. This is assumed to be due to the sample’s porosity being increased by the polymer modification. However, the

polymer modification improves the flexural and tensile strengths as well as the toughness due to an improved cohesion of the polymer-modified cementitious matrix [42, 50–52]. Creep is also increased [50].
Besides PMC and polymer-modified concrete, cement reinforced polymers were developed from fischerwerke GmbH[2] to serve as glue material for threaded steel rods anchoring in concrete structures [53]. The main difference to PMC is their larger polymer content (up to 75 %). While composite anchors seem to be of interest for researchers [54–56], to the best of our knowledge, no scientific literature is available for such materials. The possibility of using a polymer-cement composite as adhesive in bonded anchors was noted, as in passing, by Cook et al. [56]. However, on the European market, such composites are already sold by two companies, e.g. epoxy based mortars FIS EM[3] and HIT HY-10 PLUS[4]. One explanation may be that the material used as anchor is not the major parameter for reliability. Indeed, focus lies on the geometrical parameters, such as numbers and position of adhesive anchors or embedding depth and shape of the cylindrical bore holes, in particular in the most recent literature [57–60]. To investigate the reliability of polymer-cement composite anchor materials, the microstructure, mechanical properties, and aging of such new materials must be addressed.

2.2 Nanoindentation of heterogeneous materials

2.2.1 Principles of nanoindentation

The hardness testing technique at the microscale, namely microindentation, does not perform well at sub-micron length scales. The reason lies in the difficulty to optically measure the deformed area in the material after removal of the tip. Depth-sensing indentation instruments, which require both the load and the penetration into a sample during tests, were developed over time

[2] fischerwerke GmbH & Co. KG, Germany
[3] from fischerwerke GmbH
[4] from Hilti Corporation, Liechtenstein

[61, 62]. The analysis of the load-indenter displacement semistatic unloading curve gives information on the contact stiffness.

The Continuous Stiffness Measurement (CSM) method allows determining the contact stiffness during loading [63]. Thus, the CSM also enables to test materials with viscoelastic or viscoplastic behavior. Indeed, the load-indenter displacement semistatic unloading curve of materials with viscoelastic or viscoplastic behavior is strongly influenced by their viscosity and thus cannot be modeled as linear [64]. Moreover, the short time constant and the high measurement frequencies of the CSM make the testing of time-sensitive or thermal drift-sensitive materials more accurate [65]. The application range of nanoindentation, using in particular the CSM method, also includes elastic-plastic solids with power-law work-hardening, power-law creep solids, and linear viscoelastic materials [66–68].

The nanoindentation analysis is based on elastic contact theory, in particular on the analysis of the "contact of an isotropic elastic half-space by rigid indenters of various geometr[ies]" [69]. It was shown that the contact equation holds for any indenter with revolution symmetry, and the self-similar geometry of sharp pyramidal indenters, and that it even applies for elastic-plastic contact [69].

Li et al. [65] describe the relation between reduced modulus E_r, the unloading stiffness at maximal indentation depth S_u, the contact area A and a factor β depending on the indenter geometry:

$$S_u = 2\beta \sqrt{\frac{A}{\pi}} E_r \tag{2.1}$$

For a Berkovich indenter, a three-sided pyramid, the value of β depends slightly on Poisson's ratio ν and typically varies between 1 and 1.1 [69–71].

Also, the reduced modulus depends on the indenter modulus E_t and the indenter Poisson's ratio ν_t, as well as the sample's elastic modulus E and its Poisson's ratio ν with the relation [63]:

$$\frac{1}{E_r} = \frac{1-\nu^2}{E} + \frac{1-\nu_t^2}{E_t} \tag{2.2}$$

To determine the contact area A in equation 2.1, both the indenter geometry and the contact depth must be known. The indenter geometry, for a Berkovich indenter, is assumed to be of the functional form:

$$A = C_0 h_c^2 + C_1 h_c + C_2 h_c^{1/2} + C_3 h_c^{1/4} + ... \tag{2.3}$$

where $C_0, C_1, ...$ are constants, and h_c is the contact depth of the indenter [65], calculated as:

$$h_c = h_{max} - \varepsilon \frac{P_{max}}{S_u} \tag{2.4}$$

In equation 2.4, ε is a constant and 0.75 for a Berkovich tip [65] and 1 for a flat punch [71]; P_{max} is the maximal load during indentation, h_{max} the maximal indentation depth and S_u is calculated as [65]:

$$S_u = \frac{dP}{dh}\Big|_{h=h_{max}} \tag{2.5}$$

The equations 2.4 and 2.5 are used in the so-called Oliver-Pharr analysis as defined in [63] and refined in [71]. This method is applied in the time domain, which means that the load, depth and mechanical properties are functions of time only. In Continuous Stiffness Measurement, however, load, depth and mechanical properties are also function of frequency ω [68]. ω is one of an additional oscillating load with the function $P = P_{os} \exp(i\omega t)$, with P_{os} being the amplitude of the oscillation. The oscillating load is superimposed on the loading signal, resulting in an oscillating displacement response: $h(\omega) = h_0 \exp(i\omega t + \Phi)$ [65], with h_0 as its amplitude and Φ as the phase angle between the oscillating load signal and the displacement re-

sponse. In the frequency domain, the contact stiffness S is calculated continuously as a function of the indentation depth h, but it also depends on the mass of the indenter M_{in}, the stiffness of the indenter frame K_f and the stiffness of the springs that support the indenter $K_s p$ [65]:

$$S = \left[\frac{1}{\frac{P_{os}}{h(\omega)} \cos\Phi - (K_s p - M_{in}\,\omega^2)} - K_f^{-1} \right]^{-1} \tag{2.6}$$

Both experiments in the time and frequency domains present some challenges, constraints and limitations, in particular for low depth or low load indentation [68]. For example, the accurate detection of the surface, the consideration of the thermal drift or the limitation of the contribution of the measurement system to the basic outputs of the nanoindentation experiments still represent major challenges [68].

2.2.2 Nanoindentation of heterogeneous metals and composites

The CSM method enables the continuous measurement of the mechanical properties with depth to determine, for example, the mechanical properties of a thin film [72]. There, the indentation depth versus the film thickness is a key parameter for the measurement of the film properties, and minimize the substrate's influence [73]. During the measurement of the mechanical properties of a SiO_2 film on Si substrate, it was found that the substrate stiffness could be neglected for a maximal indentation depth lower than 10 % of the film thickness [73]. A Finite-Element (FE) analysis showed good agreement with nanoindentation results for both the film's Young's modulus and hardness. The friction coefficient between the indenter and the thin film does not seem to influence the load-displacement curve of the film, and thus the determination of the contact stiffness.

However, the critical indentation depth for characterization of the sole thin film properties, such as hardness and elastic modulus, is dependent on the

hardness and elasticity mismatches between thin film and the substrate. For example, in an FE analysis with both a soft ($E = 100\,\mathrm{GPa}$, yield strength $Y = 10\,\mathrm{GPa}$) and a hard material ($E = 200\,\mathrm{GPa}$, $Y = 20\,\mathrm{GPa}$), the hardness has been found to be less sensitive to the indentation depth than Young's modulus. Also, the hardness showed a significant deviation from the expected film properties for an indentation depth larger than 40 % of the film thickness only [74]. However, the indentation of the soft film on a hard substrate showed a higher elastic modulus than the corresponding bulk material with an increase of more than 5 % for indentation-depth-over-film-thickness ratio larger than 10 %. The elastic modulus of a hard film on a soft substrate already deviated by 8 % compared to that of the hard bulk material at indentation-depth-over-film-thickness ratio as small as 5 %. Moreover, a soft thin film on a hard substrate showed more pile-up than hard and soft bulk materials, whereas a hard thin film on a soft substrate showed more sink-in than the corresponding bulk materials.

The importance of careful surface preparation was highlighted, as thin films' mechanical testing requires low indent depths, thus small contact areas and better contact quality [75]. For example, a numerical simulation of a single crystal copper thin film showed that the signal-to-noise ratio due to the surface roughness increased with decreasing indentation depth [75]. Both the hardness and the elastic modulus were studied and it was suggested that a randomly patterned film roughness leads to a "big dispersion of nanoindentation results" [75]. Thus, even for very careful surface preparation, an indentation depth much greater than the characteristic size of the roughness must be chosen for thin films nanoindentation.

In the case of composites, the material under the tip may be considered as a film-substrate pair and a similar analysis and constraints as for thin films can be applied. However, composites are also laterally heterogeneous, which may lead to deviations from the film-substrate model due to the influence of a different phase nearby an indent. In particular, the determination of the zone influenced by the tip during the indentation, and thus the volume investigated

during nanoindentation of a composite, were investigated [76, 77]. Composite materials were modeled as two-phase materials, with a particle embedded in a matrix [76]. An FE study showed that both "the particle shape and the particle properties do influence the indentation response" [76]. The largest influence of the surrounding matrix on the mechanical properties determination of a particle hardness was found either for hard, thin particles, in a soft matrix or for soft, needle-shaped particles, in a hard matrix. Moreover, as an even more precise rule-of-thumb for the maximal indentation depth in a composite, when indented to characterize a single composite phase, the indenter contact radius should be smaller than 70 % of the particle radius. Furthermore, it was shown that the determination of the elastic properties of individual phases in a two-phase material, modeled as a 3D checkerboard, is only possible for a testing volume of less than 4 % of the volume of the homogeneous domains [77]. These characteristics may be difficult to achieve in a complex heterogeneous material with only small homogeneous domains.

2.2.3 Nanoindentation of biological materials

Some challenges of nanoindentation are specific to biological materials. The first one arises from their composition. Most biological materials are composed partly or fully of polymeric materials. Thus, they exhibit a viscoelastic or viscoplastic behavior with a strain-rate dependency [78]. Besides composition, they also have a complex microstructure, "in part because of their biological routes of formation" [78]. For both reasons, biological materials may present a "co-continuous composite nature" and a high heterogeneity in the local properties [78]. Moreover, their generally lower modulus compared to that of structural materials leads to difficulties in the surface detection, and thus in the determination of the contact depth of the tip into the material and the material's elastic modulus [68, 79]. The use of the CSM nanoindentation method "eliminates many of the problems sensing the surface" [79]. The surface roughness also plays a role, as in every other material. However, a

careful surface preparation, for example, using a microtome seems to provide sufficiently smooth surfaces for nanoindentation in bone [80] and tooth materials [81]. Moreover, most biological materials' mechanical properties are very sensitive to the relative humidity (and thus also the temperature) of their environment [82–84].
Nanoindentation of biological materials is extremely challenging and special issues are to be considered during testing for example bone and cartilage with the use of a quasi-static nanoindentation test method [82], or hydrogels and very compliant biological materials [78]. The CSM nanoindentation method has also been used to study biological materials [78]. Called nanoDMA [78], the CSM-based measurement technique enables testing of plant cell walls, and enabled for example the determination of differences in the cell wall's viscoelasticity of two ecotypes, and a mutant, of the same species [85].

2.2.4 Nanoindentation of hardened cement pastes

"Nanoindentation is still the most commonly-used technique to study the microstructural mechanical properties of cement-based materials" [86]. When investigating the elastic properties and the hardness of hydrated cement pastes, a first approach consists of testing the cement pastes' components individually. The clinker phase can be polished and tested by nanoindentation before hydration. Using the Oliver-Pharr analysis, the elastic modulus of C_3S, C_2S, C_3A and C_4AF was shown to vary between 125 GPa and 145 GPa, for a hardness between 8 GPa and 9.5 GPa [87]. Besides clinker phases, C-S-H is "the main product in Portland cement hydration", and "has a strong influence on the physical and mechanical properties of most cementitious materials" [88]. The mechanical properties, i.e. elastic modulus and hardness, of synthesized C-S-H were investigated by nanoindentation, to avoid potential interaction with other phases in hydrated Portland cement paste. However, synthesized or in hydrated cement paste, C-S-H remains a very complex phase. First, it has an amorphous, nanoporous heterogeneous struc-

ture, with a large surface area [88]. Second, "there are at least 30 crystalline materials that are similar in composition to C-S-H", but "differ in atomic arrangement, Ca/Si ratio, and the number of OH and H_20 groups" [88]. A Berkovich indenter was used for the nanoindentation measurements and the analysis was conducted based on the Oliver-Pharr method. It was found that the indentation modulus and hardness of C-S-H increases with decreasing Ca/Si ratio and varies between 20 GPa and 27 GPa. However, the results are significantly dependent of both the micro- and nanoporosity of the phase [88]. In another study of synthesized C-S-H with constant Ca/Si ratio, statistical analysis of the Young's modulus distribution yielded a varying number of phases having different densities and elastic properties [89]. The denser phases were compacted under higher pressure and had higher elastic modulus. It was found that the synthesized C-S-H under relatively high pressure possesses similar elastic modulus than the C-S-H found in hydrated cement paste. For the same high compaction pressure and measured with the same procedure as in the previous study, both the water content and the Ca/Si ratio influenced the microstructure, and thus the mechanical properties of C-S-H [90]. Higher water contents increased the sample density and Young's modulus. At low water content, the polymerization grade of the silicate might have increased, which also increased Young's modulus.

However, "the requirement for *in situ* synthesis and characterization of chemically complex phases obviates conventional mechanical testing of large specimens representative of these material components" [1].

Two different approaches are typically used to identify *in situ* the mechanical phases present in hardened cement pastes. The first approach combines nanoindentation and microscopy techniques to "select the indentation points such that they correspond to a certain phase" [91]. When coupling the indents location with Back-Scattered Electron (BSE) and Atomic Force Microscopy (AFM) pictures, 22 indents were conducted in a well identified High-Density (HD) C-S-H phase around unhydrated clinker. The modulus distribution from the experiment showed big scatter, which hints towards

non-negligible interactions or mixture of chemical phases within or near the HD C-S-H, instead of a single-phase around the unhydrated clinker particles [91].
The second approach consists in using a large number of indents regularly distributed over the sample surface and analyzing the nanoindentation results with statistical methods [91–93]. The number of indents is of the order of many hundreds [92, 93]. This method is called Statistical Nanoindentation (SNI) or Statistical Nanoindentation Technique (SNT). Some assumptions are made while using this method:

- the investigated surface is representative for the phase distribution of the whole sample [92].
- the depth of indentation is chosen such that only one phase is included within the Representative Volume Element (RVE) around each indent. Typical indentation depths for hardened cement pastes were around 100 nm to 500 nm [92, 93].
- the phase fraction can be calculated as the proportions of indents from the total number of indents showing mechanical properties associated to one phase.

The indentation procedure was a trapezoidal loading-holding-unloading testing function, and the load-displacement curve was analyzed based on the Oliver-Pharr method [92, 93]. Nemeček et al. [92] identified the phase properties and phase fractions in cement pastes. Only the stiffest phase, composed of unhydrated clinker, was not identified, due to the high stiffness differences with its surrounding phases. Hu et al. [93] observed the same discrepancy between the stiffness of unhydrated clinker in hydrated cement paste and as measured *ex situ* on synthetic cement clinkers, and explained it with a difference in the porosity. Also, the estimation of effective elastic properties based on nanoindentation results as input and using numerical procedures (homogenization schemes and Fast-Fourier Transform) showed a

good agreement with macroscopic experimental data [92]. Thus considering also the reduction of testing time, the SNT "can be used as an effective tool to measure and map mechanical properties of cement paste and can identify the phases" [93].

2.2.5 Statistical Nanoindentation Technique (SNT)

"Measuring the intrinsic properties of each phase separately in multiphase materials gives information that is valuable for the development of new materials and for modelling" [94]. For example, a map of the mechanical properties, i.e. Young's modulus and hardness, of $WC-Co$ measured by nanoindentation revealed the location of the WC and Co phases as well as the higher hardness of Co in this form of a binder phase compared to its bulk hardness [94].

Mapping of mechanical properties at small forces and shallow depth is a feature of nanoindentation as a mechanical testing technique for surfaces. The mechanical properties mapping gives profound information about the material phases, in particular when the phases of the investigated composite show a large discrepancy in their elastic properties or hardness. It can also give hints about the actual interaction between two (or more) phases of a material. In particular, the phases' location, their *in situ* properties and also potential "mesophases" at the interfaces between two phases of an alloy can be identified with maps from nanoindentation data [95].

The principle of the SNT is presented in Figure 2.1. SNT combines the acquirement of a large set of nanoindentation data from the surface of a material with statistics or probabilistic methods to identify regions in the material with low scatter in their mechanical properties. These regions are called constituent phases [96]. At indentation depths much smaller than the characteristic size of the heterogeneities, and for a statistically sufficient number of indents, the mechanical properties of each constituent phase, such as its elastic modulus, can be measured. At depth larger than the characteristic size

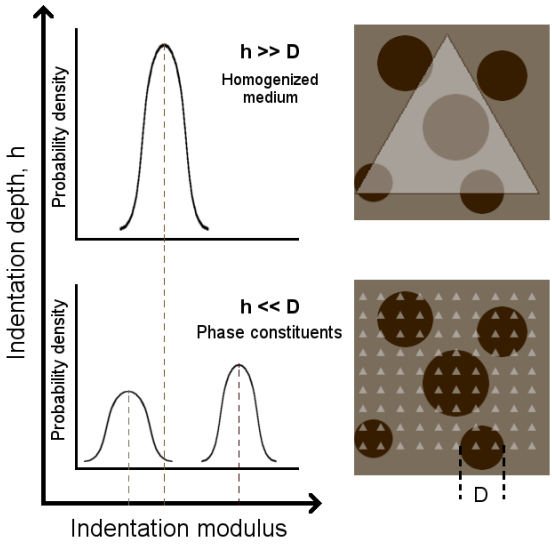

Figure 2.1: Schematic of the principle of the SNT for heterogeneous materials. Bottom: at low indentation depths ($h \ll D$) the individual constituents can be identified giving rise to multimode distributions. Top: at large indentation depths ($h \gg D$) the properties of a homogenized medium are obtained. Adapted from [1].

of the heterogeneities, only the mechanical properties of the homogenized medium are measured [1, 96].

If the goal of the SNT is to identify constituent phases in the material, then the indentation depth of the measurement must be "sufficiently smaller than the size of an average individual region of the material phase" [86]. A rule-of-thumb in nanoindentation states that $h < D/10$ is sufficient to resolve the individual phase properties [97]. This condition has many implications for the choice of h. First, D must be estimated, or at least assumed, before choosing h. This may require complementary microscopy, as e.g. from BSE image analysis [98], X-ray diffraction (XRD) method or from TEM images [91]. Depending on D, h can become very shallow. In this case, much attention must be put on the surface preparation, as it was shown that both

large scale surface waviness, with "wavelength" larger than the tip, and small scale nanometer-sized roughness can influence the nanoindentation measurement [80]. A Root-Mean-Square (RMS) roughness of five times lower than the indentation depth, measured on a surface of side length of 200 times h, leads to a unique distribution of the investigated material properties. For example, the RMS roughness leading to a stable hardness distribution in a hydrated cement paste was below 50 nm to 100 nm, for a maximal indentation depth between 100 nm and 400 nm, depending on the investigated phase [99].

The minimal number of indents must be chosen with respect to the characteristic phase sizes, the phase spatial distribution and the phase fractions. Indeed, a sufficient number of indents with no bias in the indents' locations relative to the phases' spatial distribution, enables the calculation of the surface fraction f_i of the i-th phase, as follows [1]: $f_i = N_i/N$, with $N_i \leq N$, N_i the number of indents landing in the i-th phase and N the total number of indents. Additionally, for a perfectly disordered material, after the Delesse principle [100], the surface fraction is equal to the volume fraction of the phase; thus, both terms can be used and simply be called phase fraction [101].

In the SNT, the distributions of both E and H are assumed to be weighted sums of Gaussian distributions (see eq. 2.7 and 2.9). The choice of a Gaussian to represent a mechanical phase in the fitting distribution is explained by Vandamme et al. [101] with this sentence: "for the sake of simplicity, the distribution [of the mechanical properties of a single phase] is chosen so that all standardized central moments of higher order are zero".

Thus, the mean value and standard deviation of the mechanical properties of each single phase, as well as the phase fraction for the currently investigated property (E or H) are obtained directly from the fit parameters of the whole distribution(s) with a weighted sum of Gaussians. In particular, the phase fraction f_i is calculated as the area under the Gaussian curve over the total

area of the fitting curve under the Cumulative Distribution Frequency (CDF), or Probability Density Function (PDF), plots [1].
The fitting parameters can be obtained by Maximum Likelihood Estimation (MLE), through the application of Expectation Maximization (EM) algorithm [98], or by Least Square Estimation (LSE). The experimental data can be fitted based on either the Probability Density Function (PDF) [102] or the CDF representation of their empirical distribution function (EDF) [103]. Comparing the LSE-based procedure to the EM-based procedure, the latter shows better results, as it does not require the choice of a supplementary parameter to construct the distribution representation [99]. The MLE seems to provide better results in the determination of the mechanical properties of hydrated cement phases compared to the LSE [103].

General equations of the SNT

First, the EDF $(X_j)_{j=1,\dots,N_X}$ with $X = E, H$ of the modulus E and/or the hardness H of a sample is measured by nanoindentation, with N_X the number of valid data points for the property X. The CDF of the empirical distribution is then calculated as $CDF_{X_j} = \frac{j-1/2}{N_X}$ [101], and the curves $(X_j, CDF_{X_j})_{j=1,\dots,N_X}$, with $X = E, H$ are fitted with the continuous function CDF_{fit}. CDF_{fit} is a weighted sum of $\tilde{N}_X$ Gaussian CDFs (Equation 2.7), with the Gaussian CDF as defined in Equation 2.8.

$$CDF_{fit}(x) = \sum_{i=1}^{\tilde{N}_X} f_i \, \mathcal{N}_{CDF}(m_i, s_i^2), \tag{2.7}$$

$$\text{where } \mathcal{N}_{CDF}(m_i, s_i^2) = \frac{1}{2}\left(1 + \text{erf}\left(\frac{x - m_i}{s_i\sqrt{2}}\right)\right) \tag{2.8}$$

Each of the $\tilde{N}_X$ weighted Gaussian CDFs $f_i \, \mathcal{N}_{CDF}(m_i, s_i^2)$ represents the distribution of a mechanical property in a homogenized material phase, where the functional parameters of the Gaussian, i.e. mean value m_i, standard de-

viation s_i and the associated weight or amplitude f_i are assigned to a phase's mean modulus, or hardness, with its standard deviation and the associated phase fraction within the heterogeneous material.

The PDF of the experimental distribution can also be analyzed and fitted with a sum of Gaussian PDFs. Then, first the empirical values $(X_j)_{j=1,...,\tilde{N}_X}$, with $X = E, H$, are separated in equally distributed bins $b_1, ..., b_q$, with q the total number of bins. The distance $b = \tilde{X}_{k+1} - \tilde{X}_k$, $k = 1, ..., q-1$ between the middle points $\tilde{X}_k$ and $\tilde{X}_{k+1}$ of two successive bins b_k and b_{k+1} is the bin width and thus a parameter of the PDF representation. The PDF of the experimental distribution is then $\{(\tilde{X}_k, Y_k)_{k=1,...,n}\}$ with Y_k the number of data points of (X_j) in b_k. The PDF representations of the experimental data can be fitted by the continuous function PDF_{fit}, which is also a weighted sum of P_X Gaussian PDFs (Equation 2.9). The Gaussian PDF is defined in Equation 2.10.

$$PDF_{fit}(x) = \sum_{i=1}^{P_X} f_i \, \mathcal{N}_{PDF}(m_i, s_i^2), \tag{2.9}$$

$$\text{where } \mathcal{N}_{PDF}(m_i, s_i^2) = \frac{1}{\sqrt{2\pi s_i^2}} \exp\left(-\frac{(x-m_i)^2}{2s_i^2}\right) \tag{2.10}$$

Considerations on additional constraints on the fitting function

During the fit, the total number of unknowns is equal to $3n$ for Young's modulus and $3\tilde{n}$ for the hardness, with n the total number of "elastic phases", and $\tilde{n}$ the total number of "hardness phases". For each phase i between 1 and n or $\tilde{n}$, the mean value m_i, the standard deviation s_i and the phase fraction f_i are unknown. Also n and $\tilde{n}$ are either unknown or assumed previously to the fit. Vandamme et al. [101] assumed a correlation between the distributions of Young's modulus and hardness, due to the "difference in material volume solicited respectively elastically and plastically" [101], which should add robustness to the analysis and "[avoid] the identification of spurious peaks as

mechanically activated material phases". It could be discussed here that the role of interfaces and interphases is much larger in the determination of the hardness than of Young's modulus, and thus the number of phases and the phase fractions might be different between the hardness and the modulus distributions. Also, this analysis assumes that the i^{th} hardness phase has the same composition as the i^{th} modulus phase, which might not be straightforward for certain materials. However, with this assumption, the number of "hardness phases" $\tilde{n}$ and "elastic phases" n are equal, which has the big advantage to reduce the number of unknowns in the fitting equation from $3n+3\tilde{n}$ to $3n+3n=6n$. With the additional assumption that the hardness and elastic phase fractions are also the same, the number of unknowns even decreases to $5n$.

Additional constraints can be added on the fitting parameters. For example, the sum of all phase fractions can be set to be equal to one [98], or each individual Gaussian is required to have a positive height or amplitude [104], or the minimal distance between two neighboring phases should be at least equal to the sum of both standard deviations [101]. To the author's best knowledge, the influence of these additional constraints on the deconvolution results has not been investigated yet.

2.2.6 Statistical considerations

Besides obtaining the phase properties, the SNT can also be used to estimate the number of phases in a heterogeneous material. Therefore, various statistical tools can be used to compare the best fits for a distribution having varying number of phases.

One criterion, used in the fitting procedures based on LSE, is the chi-square (χ^2) and is calculated as the residual sum of squares (RSS) between the experimental distribution and the fitting curve[5] — however, it depends on the

[5] `https://www.originlab.com/doc/Quick-Help/measure-fitresult`, visited on 1st May 2018

degrees of freedom (DOF). Thus, rather the reduced chi-square, calculated as RSS over DOF, should be used to compare fits with different numbers of phases.

Another criterion can be used in a LSE-based procedure and consists of comparing the coefficient of determination r^2 of the fits with each other [104]. The closer the r^2 approaches 1, the better is the fit. r^2 describes "the proportion of the total variation of y (about its mean $\bar{y}$) that is explained (accounted for) by the fitted model" [105]. However, the coefficient of determination monotonically increases with the number of parameters. Then, a more complex fitting function, i.e. with more parameters, would always lead to a better fit. The adjusted coefficient of determination r_a^2 addresses this point, as each sum of squares used in the calculation is divided by its DOF. It is calculated as $r_a^2 = 1 - a(1 - r^2)$, with a as an adjustment factor depending on the fitting model, in particular its DOF [105]. However, the adjusted coefficient of determination does not always provide sufficient information to enable the distinction between two models or two fits.

The Bayesian Information Criterion (BIC) was introduced to determine the optimal number of phase constituents of heterogeneous samples [93, 103]. For example, four phases were found to be optimal in hydrated Portland cement pastes [93]. An alternative could be the Akaike Information Criterion (AIC). Although AIC and BIC seem similar at first sight, the BIC is actually preferable in case of the determination of a number of phases. Indeed, the AIC favors more complex models as soon as the amount of experimental data increases [106]. The same holds for likelihood based criteria [107].

More generally, the Bayesian statistics aims at determining both the best fit for a given model, by use of the MLE [103] and the calculation of Bayes factors (or posterior values) to compare the adequacy of two models [106]. In the framework of Bayesian statistics, a posterior probability of an experimental point can be estimated and describes its probability to be part of each phase [107]. A model-based strategy for clustering is proposed by Fraley et al. [107]. First, the number of phases (n) to be considered and a starting set

of parameters for the fitting function is fixed. Then, the EM is calculated for each initial set of parameters and each number of phases, providing an optimal set of parameters. Then, the BIC of the fit with optimal parameters from EM is calculated. The BIC values of all models (i.e. a fixed number of phases and a set of optimal parameters) are compared with one another. The local maximum of the BIC indicates then a strong evidence for the associated model.

However, the choice in the numbers of phases, and thus, of parameters, is an important step of the model selection. Potentially, the true model might be infinite-dimensional. Thus, as Burnham and Anderson [108] explain: "the fit of any model can be improved by increasing the number of parameters [...]; however, a trade-off with the increasing variance must be considered in selecting a model for inference". This tradeoff is called the principle of parsimony [108]. *Parsimonious* models avoid both underfitting and overfitting; they can balance "the error of approximation and the error due to random fluctuations". The BIC is considered as a parsimonious model selection method, but with a tendency to underfitting [108].

3 Nanoindentation of Cu-Cr composites

3.1 Experimental methods

3.1.1 Samples description and preparation

Bi-metal composites, in particular Cu-Cr composites, are commonly used "as contact materials for energy distribution" [109]. As copper and chromium are not miscible [110], Cu-Cr composites are made of Cr particles spread out in a Cu matrix [111]. In the following and for simplicity reasons, the structural phases will be named after their main components, copper or chromium. A bi-metal composite system based on Cu and Cr phases and with various Cr content was chosen as model material and investigated via SNT. The elastic properties of Cu and Cr are presented in Table 3.1. The large differences in elastic properties between Cu and Cr are expected to lead to large difference in the properties of the composites phases. For comparison, Cu and Cr samples produced with the same technique were also investigated.

Table 3.1: Young's modulus and Poisson's ratio of pure Cu and Cr.

Material	Young's modulus (GPa)	Poisson's ratio	Reference
Cu	124	-	[112]
	129.8	0.343	[113]
Cr	285 to 290	-	[112]
	279	0.21	[113]

Table 3.2: Cr fraction (in weight and volume fractions) and relative density of the investigated Cu-Cr composites and the Cu and Cr compacted reference samples [111].

Sample	wt / vol-% Cu	wt / vol-% Cr	rel. density (%)
Compacted Cu	100	0	97.7
Cu25Cr	75 / 71	25 / 29	99.4
Cu60Cr	40 / 35	60 / 65	98.3
Compacted Cr	0	100	99.1

All samples were provided by von Klinski-Berger (IAM, KIT, Karlsruhe, Germany), who produced them and analyzed the influence of their microstructures on their use as contact materials [111]. The samples were compacted with Field Assisted Sintering Technique (FAST) from Cu powder with 99.9-at% purity and technically pure Cr powder (99.5-at%). The temperature of the process was 950 °C, except for the compacted Cr sample, which was compacted at 1450 °C. The weight and volume fractions of Cu and Cr in the investigated Cu-Cr samples are summarized in Table 3.2 [111]. The density of Cu is $8.93\,\mathrm{g\,cm^{-3}}$, and is $7.19\,\mathrm{g\,cm^{-3}}$ for Cr [111]. Some pores were observed in the copper-chromium composites produced by FAST. Relative densities below 100 % were measured in all investigated samples [111] and are also summarized in Table 3.2.

The samples were manually ground and polished. To simplify the sample preparation of the samples, they were glued with Crystalbond™ 509 adhesive (Ted Pella, Inc., Redding, California, USA) on aluminum cylinders at a temperature of around 80 °C. The preparation procedure included grinding with SiC paper from P600 to P4000 grid size under water flow. The first grinding step was stopped after the sample was flat and the further steps after about 3 minutes each. Then the samples were polished with various water-based diamond suspensions of 3 µm, 1 µm, 0.25 µm and 0.1 µm grain size. Between each step, the samples were cleaned with propanol in an ultrasonic bath and dried with air at around 50 °C. Finally, the samples were taken off

Table 3.3: Area fraction and Equivalent Circle Diameter (ECD) of Cr particles in Cu-Cr composites parallel to FAST pressure direction [111].

Sample	Cu25Cr		Cu60Cr	
Area fraction (%)	69	31	5	95
ECD (µm)	50	110	65	1068
St. Dev. ECD (µm)	25	40	40	15

the sample cylinder and re-glued with a thin layer of cyanoacrylate-based adhesives to reduce the influence of the thick layer of Crystalbond glue on the nanoindentation measurement.

Despite careful handling, this procedure induced a tilt of the sample surface in all samples but the compacted Cu sample, as estimated in Section 3.2.1. A second set of Cu25Cr, Cu60Cr and compacted Cr samples was also prepared, glued with 2k UHU Plus Endfest 300 (UHU GmbH & Co. KG, Bühl, Germany), and ground similarly as described above. In order to avoid step creations between the Cu and the Cr phases, the two last grinding steps were replaced by a polishing step with 9 µm diamond paste (on MD largo, Struers A/S, Ballerup, Denmark). After this step, the samples were polished with various water-based diamond suspensions of 3 µm, 1 µm, 0.25 µm grain size. Long polishing durations (5-30 min) were necessary at the 3 µm polishing step to eliminate the scratches of the 9 µm-step, particularly present in the Cr phase. The polishing time at this step increased with the Cr content of the sample.

The microstructure of Cu-Cr composites was intensively investigated with the goal to better understand the link between the composites microstructure and their behavior as contact materials [109, 111]. The chromium-rich phase of the compacted samples exhibit an isometric microstructure in the plane perpendicular to the pressing direction during FAST and are elongated in the direction parallel to the pressure direction [109]. This is a consequence of the FAST production technique, as the pressure applied during sintering is

Table 3.4: Area fraction and aspect ratio of Cr particles in Cu-Cr composites parallel to pressure direction [111].

Sample	Cu25Cr		Cu60Cr
Area fraction (%)	81	19	100
Aspect ratio	1.9	3.8	1.3
St. dev. of aspect ratio	0.7	1	0.01

not hydrostatic but directed along one axis. Tables 3.3 and 3.4 summarize the microstructure characteristics (ECD and aspect ratio) of the Cr particles parallel to the pressure direction during production [111]. A bi-modal distribution of the particles is observed in both composite samples, but with a stronger aspect ratio in Cu25Cr than in Cu60Cr. In the experiments presented in the following, the samples were prepared such that the investigated surface was parallel to the pressing direction.

3.1.2 Micromechanical testing with nanoindentation

A load-controlled Nanoindenter G200 XP (Agilent/Keysight Technologies Keysight Technologies, Inc., Santa Rosa, CA, USA) equipped with CSM and Express Test (ET) options were used to investigate the mechanical properties of Cu-Cr composites and compacted reference samples at a microscopic scale. The ET option is a grid nanoindentation technique with high indentation frequency, thus enabling indenting around 1000 locations per hour, compared to around 10 locations per hour for the standard CSM method [114, 115].

The bi-metal composites were tested using a diamond Berkovich tip, assuming tip Young's modulus and Poisson's ratio of 1141 GPa and 0.07, respectively. Two kind of measurements were realized, first with the standard CSM method and then with ET.

Standard CSM experiments

In the first measurement batch, the CSM additional sinusoidal signal was applied only during the approach and the loading segment at frequency of 45 Hz and nominal RMS depth amplitude of 2 nm, until the maximum depth was reached. Then, the static load was held for ten seconds and then removed at a rate of $20\,\mathrm{mN\,s^{-1}}$ until 90 % of the load on sample. The thermal drift was measured during 75 s at this load and then the load was removed at the same previous unloading rate. The target strain rate $\frac{\dot{P}}{P}$ was $0.05\,\mathrm{s^{-1}}$ until a maximal depth of 2000 nm to 2100 nm.

The tip area function and the load frame stiffness were calibrated on a quartz reference sample over a depth range between 200 nm and 2000 nm. The load frame stiffness was corrected on every sample as described in [116] to yield an elastic modulus approaching the literature value (3.1), while in the composite samples, only the curves which were obviously in a homogeneous phase were used. For all samples, ε was set to 0.75 and β to 1.034. The Poisson's ratio was assumed as 0.343 for the compacted Cu and 0.21 for the compacted Cr samples (3.1). For the Cu-Cr composites, it was set to 0.25. 25 tests were done in each sample to a maximum depth of 2100 nm with a minimal distance between indents of 45 µm. The modulus and the hardness were evaluated at 200 nm, 500 nm, 1000 nm and 1500 nm, as well as at the largest available depth in the range of 1900 nm to 2000 nm.

In both composite samples, indents being in a single phase were selected and their modulus and hardness values were investigated as function of the Cr content of the sample. The selection appears in two steps. First, indents for which the load-displacement curve showed irregularities, for example a pop-in or an "[unstable] contact between the tip and the material surface at the initial loading process" [86], were sorted out. The irregularities are assumed to be mostly related to the indent location at an interface between phases and to the interaction between neighboring Cu and Cr phases. Then, the remaining curves are assigned to either the Cu phase for the curves with

the lowest mean modulus or the Cr phase otherwise. The indent location is confirmed by light microscopy (see Figure 3.1). From all 25 indents in each sample, 5 to 10 indents were located either in the Cu, or in the Cr phases. For these indents, the load, the hardness and the modulus were averaged over the depth range of the measurement.
To verify that the load-displacement or modulus over indentation depth curves can be correlated to the sample microstructure under the indent, Cu25Cr was also indented at a shallower depth of 500 nm and the test location was investigated with FIB and SEM to exhibit the three-dimensional microstructure underneath the indent.

ET experiments

High-speed nanoindentation experiments (ET) enable testing a large number of locations in a short period of time. With this kind of experiments, the quality of the analysis of the surface heterogeneity is increased by the capacity of testing around 100 times more locations on the surface than with the standard CSM method and in the same time. ET experiments were conducted in the Cu-Cr composites and compacted samples at an indentation depth set to 1000 nm for a distance between indents of 20 µm. For Poisson's ratios, ε and β, the same values as in the standard CSM measurements were assumed. Only the indents with indentation depth within 600 nm to 2000 nm were kept for the analysis, in order to get a consistent depth range for the mechanical properties analysis. Table 3.5 summarizes the total tested surface, the total number of indents made in each sample, the number of actually analyzed indents, as well as the averaged depth of the analyzed indents for all samples.

3.1.3 Statistical analysis

The Cu-Cr composites as well as the compacted Cu and Cr samples were analyzed with the deconvolution procedures described in Appendix A. Fitting functions with between one and five phases were chosen for statistical

Table 3.5: Total tested surface area, total number of indents, number and mean depth of analyzed indents in Cu-Cr composites and in compacted Cu and Cr samples.

Sample	Compacted Cu	Cu25Cr	Cu60Cr	Compacted Cr
Total indents number	72	$26 \times 26 = 676$	$3 \times 16 \times 16 = 768$	36
Total tested surface area	$2 \times 100 \times 100\,\mu m^2$	$500 \times 500\,\mu m^2$	$3 \times 120 \times 120\,\mu m^2$	$100 \times 100\,\mu m^2$
Number of analyzed indents	66	554	606	35
Depth of analyzed indents	1036 ± 109 nm	976 ± 113 nm	976 ± 175 nm	957 ± 27 nm

analysis, depending on the sample Cr content and the indentation depth (see App. B).

First, the Expectation Maximization (EM, see Section A.1.4) fitting procedure was used to investigate the modulus evolution with depth (standard CSM experiments). Then, the Levenberg-Marquardt (LM, see Section A.1.1) and the EM fitting procedures were used to investigate the influence of the high-rate and large number of experiments at constant depth (ET experiments) on both the hardness and the modulus distributions. Finally, the results from both nanoindentation testing methods are compared, as well as the deconvolution results from both fitting procedures.

3.1.4 Microstructural investigations

For the two-dimensional microstructure investigations, an optical microscope (Nikon Eclipse LV150N) equipped with objectives of 4, 10, 20, 50 and 100 of magnification was used for visual control of surface quality previous to mechanical testing and imaging the microstructure.

Additionally, the three-dimensional microstructure of the Cu25Cr sample was investigated by Focused Ion Beam (FIB, Scios, FEI Inc.) cross sectioning. The material was cut perpendicular to an indent from standard CSM experiment at low depth.

A graphical user interface (GUI)-based line-cut procedure (GUI_linecut V2.0 by M. Funk, S. Meister, IAM, KIT, Germany, 2012) implemented in Matlab (Release 2015b, The MathWorks, Inc., Natick, MA, USA) was used to determine the grain size of a material from the measurement of the grains chord lengths in a cross section. The procedure was extended to consider the case of a 2-phase material and measure the size of the individual phases. First, the chord lengths of both material phases are manually selected from a picture. Then, a material is assigned to each chord. The segment lengths of both phases are recorded and treated separately as in the one-phase case.

This modified procedure was used to measure the phase area fractions of both phases, as well as a characteristic size for each phase. In the calculation, the length over diameter ratio is set to $\pi/4 \approx 0.79$. This ratio estimates the difference between the mean linear intercept of a phase (particle) and the averaged particle diameter. The ratio is exact for circular particles [117].
The area fraction of the j^{th}-phase A_j is calculated as $A_j = \frac{\sum_p l_{j,p}}{\sum_q l_{k,q} + \sum_p l_{j,p}}(\%)$, with $j,k = 1,2$; $j \neq k$; $p = 1...n$; $q = 1...m$, and where $l_{j,p}$ is the p^{th}-chord length l of phase j measured during the line-cut procedure. The mean diameter D_j of the particles in a given phase is then calculated as $D_j = \frac{1}{0.79\,n}\sum_{p=1}^{n} l_{j,p}$.
A confocal laser microscope (VK 9710K, KEYENCE Corporation, Itasca, IL, USA) is used to capture three-dimensional reconstructions of various surfaces topology. If necessary, the image tilt was corrected based on the mean surface tilt. From the surface topology, a root mean square areal roughness parameter $R_q = \sqrt{\frac{1}{n}\sum_{i=1}^{n} y_i^2}$ was calculated. The areal roughness depends on the scan size [99], thus the scan size was estimated for each measurement and was typically 3000 to 8000 μm^2 for the smaller scans and $530 \times 2200\,\mu m^2$ for the larger scans.

3.2 Results

3.2.1 Microstructure, surface roughness and surface tilt estimation

Microstructure

The microstructure of the Cu-Cr composites Cu25Cr and Cu60Cr is presented in Figure 3.1. The agglomeration of the Cr particles observed and measured by von Klinski [111] is confirmed optically (Figure 3.1b) for the sample with high Cr content, Cu60Cr.
In the zone investigated via nanoindentation, the Cr phase fraction and the Cr particle size were measured using the line-cut procedure in two perpendicu-

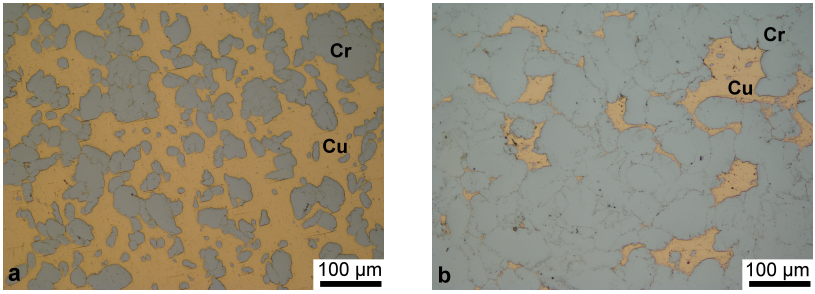

Figure 3.1: Polished Cu-Cr composites samples with (a) 25-wt% Cr and (b) 60-wt% Cr investigated with light microscopy. The copper and chromium phases are marked on the pictures by Cu and Cr, respectively.

Table 3.6: Cr particles size distribution in $200 \times 200\,\mu m^2$ fields in Cu-Cr composite samples.

Sample	Cu25Cr		Cu60Cr	
Particle diameter (µm)	30 ± 15	90 ± 12	25 ± 17	86 ± 33

lar directions, and on a cross section perpendicular to the sample compression direction. Table 3.6 summarizes the Cr particles size distribution and Table 3.7 the Cr phase fraction in the $200 \times 200\,\mu m^2$ fields. There, after the Delesse principle and assuming perfect disorder of the microstructure in the composites, the area fractions of the material, either theoretical or measured, are assumed to be equal to the material volume fraction (see Section 2.2.5). The Cr particles show a bi-modal size distribution in both samples, probably related to the production method of the samples by FAST. Compared to the theoretical area fraction of Cr in the samples (s. Table 3.2), the measured area fraction of Cr is overestimated in Cu25Cr and underestimated in Cu60Cr.

Surface roughness

The compacted Cu and Cr samples exhibit a roughness below 0.1 µm over $4 \times 10^4\,\mu m^2$ to $5 \times 10^4\,\mu m^2$. The sample roughness of Cu25Cr and Cu60Cr is

Table 3.7: Cr area fraction in $200 \times 200\,\mu m^2$ fields on two Cu-Cr composite samples of various Cr content.

Sample	Cu25Cr		Cu60Cr	
Direction	1	2	1	2
Area fraction (%)	38.4	32.5	60.8	63.3
Mean area fraction (%)	35.4		62.1	
Theoretical area fraction (%)	29.3		65.1	

higher, below 0.3 µm for the standard CSM samples, prepared with the first polishing method. At the scale of a single phase, however, the roughness decreases until 0.05 µm to 0.14 µm.

In the samples prepared for ET measurements, the roughness is larger than in the standard CSM samples, and reaches 0.5 µm to 1.1 µm over an area of $6 \times 10^4\,\mu m^2$ to $9 \times 10^4\,\mu m^2$, and only less than 0.3 µm on a homogeneous phase (over an area $<3 \times 10^3\,\mu m^2$). The roughness of these last samples and the difference between both samples might have consequences for the nanoindentation experiments.

Surface tilt and estimation of error on hardness

Due to the sample preparation (see Section 3.1.1), the sample surface of the Cu-Cr samples prepared for standard CSM measurements was tilted. This misalignment of the samples towards the horizontal plane was determined with the confocal laser microscope as 0.67° for Cu25Cr and 1.29° for Cu60Cr.

The error in the contact area due to the misalignment was estimated as:

$$\frac{\Delta H}{H} = \frac{H_{actual} - H_{ideal}}{H_{ideal}} = \frac{A_{p,ideal} - A_{p,actual}}{A_{p,actual}} \tag{3.1}$$

In general, the hardness H is calculated as the ratio of the maximal load on the sample P_{max} and the projected area of the indent A_p, so that $H = \frac{P_{max}}{A_p}$. To estimate H_{actual} and H_{ideal}, A_p is measured with two different procedures, on the same 15 indents of the tilted Cu60Cr sample. This enables the simplification of the equation for P_{max} and the hardness error due to tilt only depends on the projected areas $A_{p,actual}$ and $A_{p,ideal}$.

First, $A_{p,actual}$ is the projected area of the actual indent on the sample surface. The red triangles on Figure 3.2a highlight the contour of the actual projected area for some indents.

Then, $A_{p,ideal}$ is defined as the area of the same indent on an ideally non-tilted surface, and is measured as the largest equilateral triangle that fits into the real projected indent surface. The red triangles on Figure 3.2b represent the contour of such a triangle for the same three indents as on Figure 3.2a.

As Cu60Cr had the highest surface tilt, this sample also exhibits the largest error of all investigated samples due to the underestimated contact surface in the hardness measurement. Following the equation 3.1, ΔH was estimated as $-18.5 \pm 7.4\,\%$ in Cu60Cr, and the tilt leads to underestimate the sample's hardness. The relatively consistent hardness error over all investigated indents indicates a very tilted, but rather smooth surface.

3.2.2 Microstructure and mechanical properties of a shallow indent in Cu25Cr

Shallow indents in Cu25Cr in the proximity of a Cr particle were conducted to a depth of 500 nm and with a distance of 10 µm between indents (Figure 3.3a). SEM pictures reveal the position of each indent (Figure 3.3b) and the material phase at the indent location (Figure 3.3c). Indents 3, 4 and 7 seem to be fully or partially located on a Cr particle (Figure 3.3a), the other indents are located on the Cu matrix. In particular, indent 7 (highlighted by a red circle in Figure 3.3a) appears to be fully located on a Cr particle.

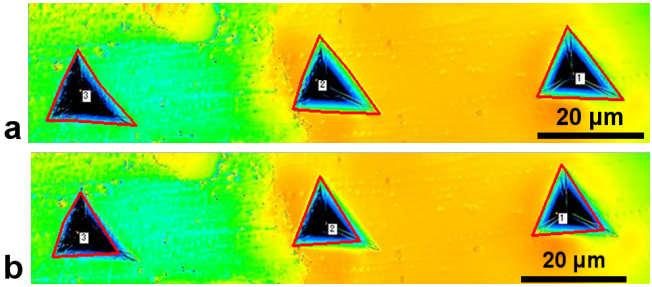

Figure 3.2: Height representation of a Cu60Cr surface with three indents (black triangular areas). The indents projected areas are measured in two different ways (red lines) to analyze the effect of the misalignment on the indent projected area: (a) the real, misaligned indent projected area $A_{p,actual}$ and (b) the equivalent projected area $A_{p,ideal}$ on an ideally, non-tilted surface.

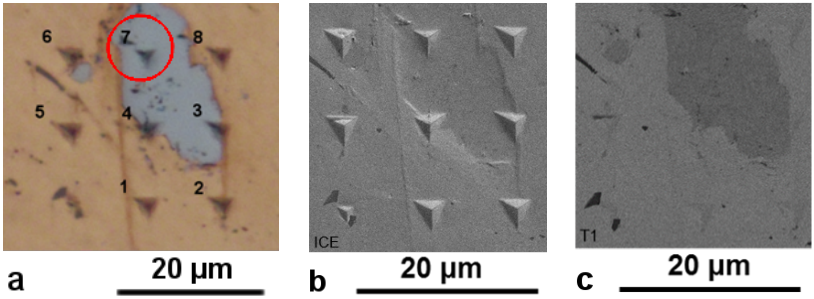

Figure 3.3: Indent field in Cu25Cr composite sample around a Cr particle, from (a) optical microscopy, (b) SEM showing secondary electron contrast, and (c) SEM showing Back-Scattered Electron (BSE) contrast. Indent 7 lies on the surface of a Cr particle.

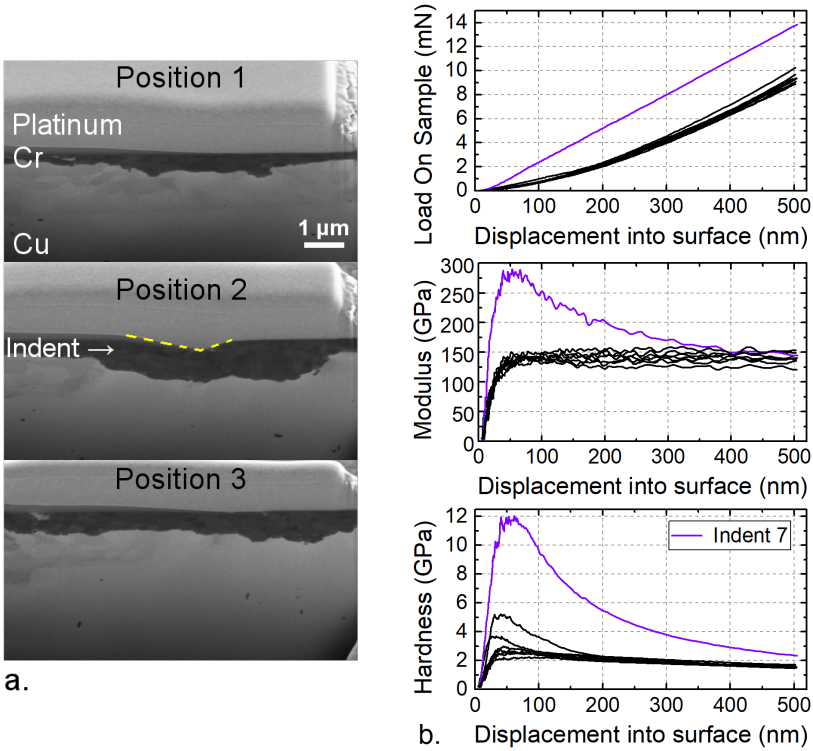

Figure 3.4: (a) FIB cross sections of indent 7 at three positions of the indented region in Cu25Cr, imaged at a tilt angle of 52° to the vertical. The scale bar is the same for all FIB cross sections. (b) Load on sample, modulus and hardness curves over depths for all 8 shallow indents in Cu25Cr. The Cr particle influences the mechanical behavior of the material mostly at lower depths.

To investigate the microstructure-properties relationship in composite samples, the microstructure underneath the indent number 7 was investigated by FIB cross sections perpendicular to the surface (Figure 3.4a), at two positions in the immediate proximity of the indent (positions 1 and 3) and also through the indent (position 2). The SEM pictures from FIB cross sections confirmed that the indent is located on a Cr particle with large surface area compared to its thickness. The mean thickness of the Cr particle was estimated as around 2 µm, measured at 10 locations in the cross section on the one side (position 1, 1.80 ± 0.16 µm) and 8 locations on the other side (position 3, 2.30 ± 0.32 µm) of the indent.

The load-indentation depth curves, as well as the modulus and hardness variation over indentation depths for all indents are shown in Figure 3.4b. Despite the tip not being calibrated below 200 nm depth, trends in the modulus and hardness of the indents can be qualitatively compared to each other at lower depths, as the calibration error is consistent for all indents of a single measurement batch. The curves highlight the special behavior of indent 7 compared to that of the 7 other indents. The 7th indent exhibits higher loads on sample, higher modulus and hardness values than all other 7 indents over the whole indentation depth. The modulus and hardness of indent 7 reach a plateau for both the modulus and hardness at depths around 40 nm to 70 nm and then decrease. Modulus and hardness deviate from more than 10 % of their plateau value for depths around 100 nm and tend towards the mean values of the 7 other indents for the largest depths.

The 7 other indents have a mean modulus of 140 ± 10 GPa and a mean hardness of 1.6 ± 0.1 GPa at 490 nm depth. Their modulus is constant over the whole indentation depth range, whereas their hardness exhibit a small peak at very low depth (less than 100 nm) for both indents 3 and 4. Note that this hardness peak has a much smaller amplitude than for indent 7.

From this low-depth experiment, it is obvious that the microstructure underneath an indent influences both the modulus and hardness measurements. For example, indent 7 seems to be fully located on the Cr particle: the measured

modulus of 275 GPa for depths between 40 nm and 100 nm could correspond to the mechanical properties of Cr (see Table 3.1). The depth of the modulus plateau in indent 7 corresponds to significantly less than 10 % of the measured layer thickness.

Also, looking at indents 3 and 4 that are partly located on the Cr particle, it seems that the hardness is more sensitive than the modulus in detecting the presence of a harder and stiffer phase in the neighborhood of the indents. This corroborates the affirmation that "the material volume solicited elastically below the indenter is much larger than the volume solicited plastically" [101].

3.2.3 Modulus and hardness of single phase indents

In the standard CSM measurements of Cu-Cr samples, some indents could be clearly associated with a single phase over the whole indentation depth, based on both their location as seen from optical microscopy pictures and on the load-displacement curves [76]. Out of the 25 indents per sample, five to ten indents were assigned to the single phases in each sample, and their modulus-displacement and hardness-displacement curves were averaged (Figure 3.5). The mechanical phases as defined from these experiments are called Cu-rich and Cr-rich phase to highlight both their main component and the fact that their exact composition is unknown.

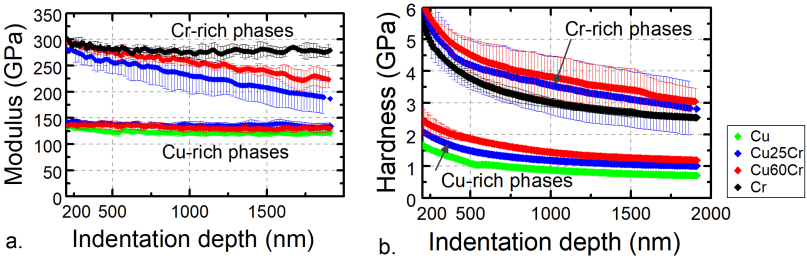

Figure 3.5: (a) Modulus and (b) hardness over indentation depth in single phase indents of Cu-Cr composites and in compacted Cu and Cr samples.

Indents into the Cu-rich phase exhibit a constant modulus over indentation depth in all samples (Figure 3.5a). The highest modulus in the Cu-rich phase is found in the Cu25Cr composite and the lowest in the compacted Cu sample. In the Cr-rich phase, the modulus is constant over depth in the compacted Cr sample, but decreases with increasing depth in both Cu-Cr composites (Figure 3.5a). The modulus decrease is more pronounced for higher depths in the sample with lower Cr content.
In the Cu-rich phase of all samples, the hardness decreases with indentation depth and increases with Cr content of the sample (Figure 3.5b). The hardness also decreases with indentation depth in the Cr-rich phase (Figure 3.5b). Comparing the Cr-rich phases only with the compacted Cr sample, the lowest hardness is found in the compacted Cr sample and the highest in the Cu60Cr sample.
The standard deviations of the averaged curves are larger in the Cr-rich phase than in the Cu-rich phase for all samples and for both the modulus and the hardness. This indicates that the modulus and the hardness estimations in the Cr-rich phase are more influenced by the neighboring Cu-rich phase and the microstructure under the indent than the Cu-rich phase is influenced by the neighboring Cr-rich phase.
The composite mechanical phases behave differently than the compacted pure samples. This corroborates the assumption that the mechanical phases as determined here cannot be considered as chemically pure, and that the composites microstructure plays a role in the determination of the single phase properties, even for indents that show similar behavior as the reference samples.

3.2.4 Influence of indentation depth

The role of the indentation depth on the determination of the individual phase properties is investigated for the Cu25Cr and Cu60Cr composites. The modulus and hardness distributions of 24 indents in Cu25Cr and 25 indents in

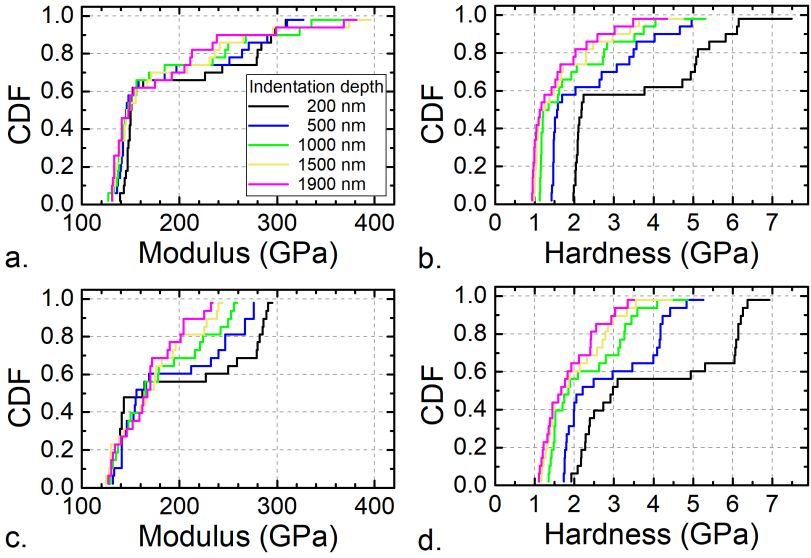

Figure 3.6: CDF of modulus and hardness at various depths in Cu-Cr composites. a) Modulus CDF in Cu25Cr, b) Hardness CDF in Cu25Cr, c) Modulus CDF in Cu60Cr, d) Hardness CDF in Cu60Cr

Cu60Cr, measured by standard CSM nanoindentation, are plotted in Figure 3.6. In each sample, the modulus and hardness distributions were analyzed at depths of 200 nm, 500 nm, 1000 nm, 1500 nm and 1900 nm with the statistical indentation technique and the EM fitting procedure.

The rough curves are due to the small number of indents. The more data points in a CDF representation, the smoother the curve. In Figure 3.6b, for example, the distributions at low hardness values are smoother than at high hardness values, due to the large number of indents (40 % to 60 %) in a narrow hardness range.

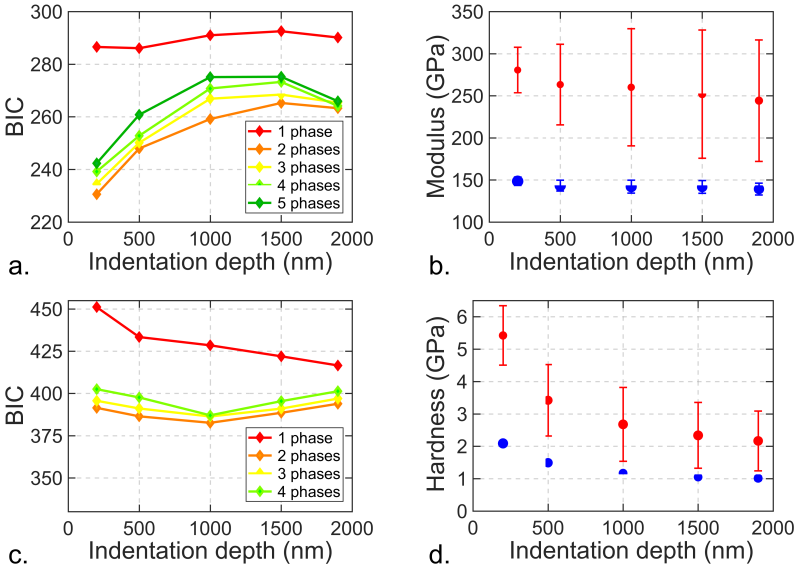

Figure 3.7: BIC of optimum fits of (a) modulus and (c) hardness as a function of the indentation depth and for various numbers of phases in Cu25Cr composite, and representation of optimum fits of the (b) modulus and (d) hardness distributions as a function of the indentation depth.

At low chromium content

In Cu25Cr, a Gaussian mixture with two phases possesses the lowest BIC for both modulus and hardness empirical distributions (Figures 3.7a and 3.7c), thus a deconvolution with two phases is optimum at each investigated depth for both modulus and hardness. Figures 3.7b and 3.7d represent the optimum phases for the modulus and the hardness, respectively, of Cu25Cr at various depths. Each phase is represented by a circle (Fig. 3.7c,d), whose area is proportional to the phase fraction as determined from the fitting procedure. The circle represents the phase mean value and the circle error bar the standard deviation of the phase's property. The phase fraction of the phase 1, with the lowest stiffness and hardness, is summarized in Table 3.8.

Table 3.8: Phase fraction of the phase with the lowest stiffness or hardness (phase 1) in Cu25Cr, as calculated from SNT on the modulus and hardness distributions at various depths.

	Property	
Analysis depth	Young's modulus	Hardness
200 nm	64.0 %	56.0 %
500 nm	63.2 %	51.0 %
1000 nm	62.2 %	47.0 %
1500 nm	57.6 %	46.2 %
1900 nm	57.1 %	47.7 %

The mechanical properties (modulus and hardness) of the phase with the lowest properties (phase 1) are constant with depth (modulus around 145 GPa and hardness around 1 GPa). In contrast, both modulus and hardness of the phase with the highest properties (phase 2) decrease with depth.
In case of the modulus, the standard deviation of the phase 2 increases until 1500 nm, which indicates that the second phase shows greater variation at large depths than at shallow depths, e.g. 200 nm. Also, the BIC of the modulus optimum fit with two phases is near the BIC of the best modulus fit with three and four phases, in particular at a depth of 1900 nm. This indicates that the second phase could probably be split into two or three phases to better describe the experimental distribution.
The phase fraction of phase 1 varies with the investigated depth (Table 3.8). It decreases continuously with increasing depth for both the modulus and the hardness distributions and is up to 15 % lower when calculated from the hardness distribution than from the modulus distribution. The volume fraction of the Cu phase measured on the investigated sample of Cu25Cr lies at around 64.6 % (Table 3.7). The fractions of phase 1 calculated from the modulus distribution until a depth of 1000 nm lie within 10 % of this optically measured value.

Table 3.9: Cumulative phase fraction of the phase(s) with mean stiffness below 200 GPa or with the lowest hardness in Cu60Cr, as calculated from SNT on the modulus and hardness distributions at various depths.

	Property	
Analysis depth	Young's modulus	Hardness
200 nm	54.1 %	54.2 %
500 nm	58.3 %	47.8 %
1000 nm	66.1 %	51.8 %
1500 nm	79.5 %	42.4 %
1900 nm	100 %	38.4 %

At high chromium content

According to the BIC of the fits with various phases, one phase or a sum of two to four phases are optimal to describe the empirical modulus distribution in Cu60Cr, depending on the indentation depth (Figure 3.8a). The optimal distributions are plotted on Figure 3.8b. At 1900 nm, a single normal distribution fits best the empirical modulus distribution. Its mean value is 171 GPa. Both the most compliant and stiffest modulus phases of the sample Cu60Cr converge to this mean value with increasing indentation depth.

Three phases (up to 500 nm) or two phases (from 1000 nm on) are optimal to fit the empirical hardness distribution in Cu60Cr (Figure 3.8c). Both the softer and harder phases exhibit a decreasing hardness with increasing indentation depth. This effect diminishes after 1000 nm and both phases have rather constant properties at depths higher than 1500 nm (Figure 3.8d).

From the EDF of the modulus, the cumulative phase fractions of the phase(s) with mean modulus below 200 GPa are summarized in Table 3.9. They increase with depth and all lie well above the experimentally measured phase fraction of Cu in Cu60Cr, which is around 37.9 % (see Table 3.7). The fractions of the first phase calculated from the hardness EDF seem to converge towards this value with increasing depth.

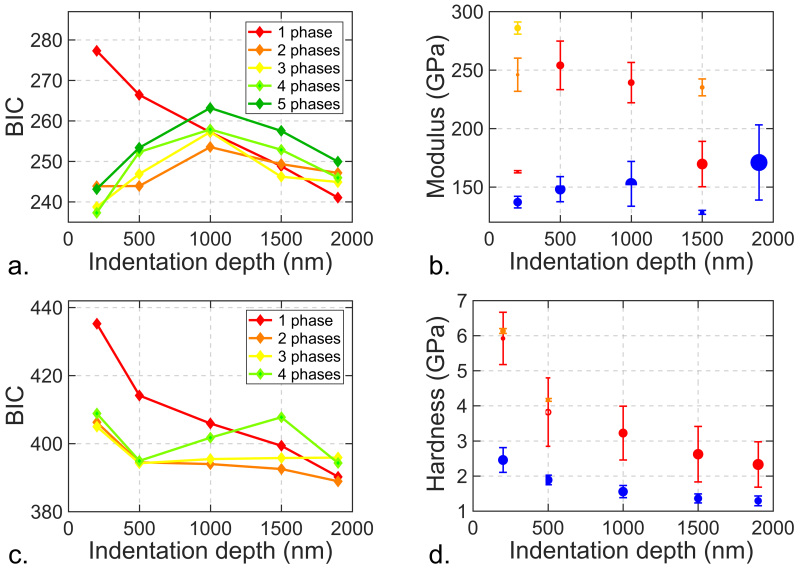

Figure 3.8: BIC of optimum fits of (a) modulus and (c) hardness as a function of the indentation depth and for various numbers of phases in Cu60Cr composite, and representation of optimum fits of the (b) modulus and (d) hardness distributions as a function of the indentation depth.

3.2.5 Influence of Cr content

The modulus and hardness EDF of the ET measurements in the compacted Cu and Cr samples and in Cu25Cr and Cu60Cr are analyzed.

The modulus EDF of both composite samples lies between the EDF of the compacted Cu sample for the lower modulus values and the compacted Cr sample for the higher ones (Figure 3.9a), with the Cu25Cr having lower modulus values than in Cu60Cr. Young's modulus of the compacted Cu and Cr samples measured by high speed nanoindentation is 125 ± 11 GPa and 386 ± 12 GPa, respectively. The modulus of the compacted Cu sample measured with ET experiments corresponds to Young's modulus found in literature [111]. For the Cr sample however, the measured modulus is about

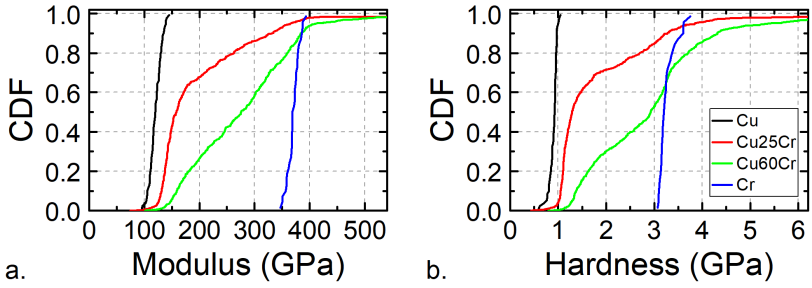

Figure 3.9: (a) Modulus and (b) hardness distributions from high speed nanoindentation in Cu-Cr composites at 1 µm depth.

100 GPa higher than values from literature [111]. This will be discussed in more detail in section 3.2.7.

The hardness EDF of the compacted Cu sample, Cu25Cr and Cu60Cr samples look similar to their modulus EDF (Figure 3.9b). However, around 20 % of the values in the Cu60Cr hardness distribution show a higher hardness than in the compacted Cr sample. As references, the mean hardness is 3.19 ± 0.08 GPa in the compacted Cr sample and 0.92 ± 0.07 GPa in the compacted Cu sample.

Both modulus and hardness EDFs were fitted with two to three phases using the LM fitting procedure. The fitting results in both cases are compared in the following and are summarized in Appendix B, Tables B.5 to B.8. Interestingly, the standard deviations of the phases in the compacted samples are much smaller than the standard deviations of most phases in the composites samples (Figures 3.10 and 3.11).

First, two phases are used to fit the modulus distribution of both Cu-Cr composites (Figure 3.10a). Both phases in both samples have Young's modulus between the compacted samples, when measured and analyzed with the same procedure. The mean modulus of both phases increases with the Cr content of the sample. The standard deviation of the most compliant phase increases with increasing Cr content.

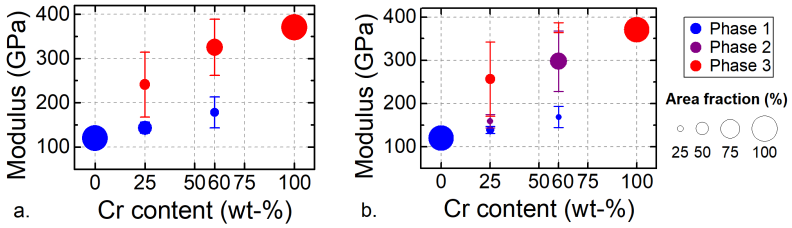

Figure 3.10: Deconvolution of modulus distribution from high speed nanoindentation in Cu-Cr composites with (a) two or (b) three phases as function of the sample Cr content.

In the three-phase fit in Cu25Cr (Figure 3.10b), the third phase decomposes a part of the empirical distribution into two phases with small differences in mean values. At the same time, its area fraction is either small, less than 10 %, or around the half of one phase fraction from a two-phase fit. For example of the latter case, the most compliant phase of the two-phase fit (Figure 3.10a) is decomposed in two phases with mean values varying by 13 % in the three-phase fit. Also, the area fraction of both first and second phases together is very similar to the volume fraction of the most compliant phase in a two-phase fit: 58 % versus 54 %. As an example of the first case, the third phase in Cu60Cr has a mean modulus varying from the Cr mean modulus by only 1 %, and an area fraction of only 6 %.

The hardness EDFs were fit with one to three phases, depending of the sample Cr content. There, also the compacted samples were sometimes fit with two phases. The hardness of the compacted Cr sample, for example, is deconvoluted with a softer phase at 3.17 ± 0.06 GPa, representing 70 % of the locations, and a harder phase at 3.45 ± 0.19 GPa, which represents the remaining locations. However, one phase at 0.92 ± 0.07 GPa was sufficient to describe the whole hardness EDF of the compacted Cu sample.

In the composite samples, the mean hardness of both phases in a two-phase fit increases with increasing Cr content (Figure 3.11a). Similarly, the area fraction of the hardest phase increases with increasing Cr content, and the contrary for the softest phase. Interestingly, a higher area fraction of a phase

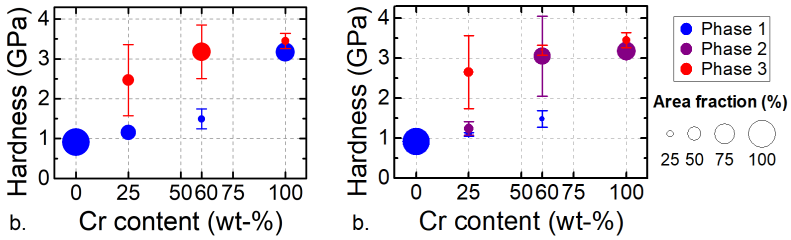

Figure 3.11: Deconvolution of hardness distribution from high speed nanoindentation in Cu-Cr composites with (a) two or (b) three phases as function of the sample Cr content.

is always associated to a lower standard deviation of the same phase, independent of its mean value. But as for the modulus, the standard deviation of the softer phase also increases with increasing Cr content.

While analyzing the hardness EDF in the Cu-Cr composites with three phases instead of two (Figure 3.11b), the third phase mostly refines the deconvolution around the phase with the largest area fraction. For example, the difference of the mean hardness between the intermediary phase and the next phase is below 0.16 GPa ($= 13\,\%$) for both Cu-Cr composites. Also, the area fraction of the hardest phase in Cu25Cr is only 5 % lower than the hardest phase in the two-phase fit area fraction, and the hardness variation between the two phases is 7 %. This means that in Cu25Cr, the first phase is *divided* into two phases, without impacting the upper half of the hardness distribution. In Cu60Cr, the difference in area fraction of the softest phase between the two-phase and the three-phase fits is only 8 % for a mean hardness variation of only 1 %. The addition of the third phase does not substantially influence the softest phase.

Such variations in the number of phases used to fit experimental distributions help identifying the weakest part of the deconvolution, where the deviations from a two-phase distribution of the mechanical properties are the largest.

3.2.6 Comparison of fitting procedures

The distributions from the ET nanoindentation experiments in the Cu-Cr composites were previously analyzed with LM fitting procedure. In this section, the distributions are also analyzed with the EM fitting procedures and both results are compared. The fitting results of the EM fitting procedure are summarized in Appendix, Tables B.5 to B.8.

In the fits from the EM procedure, the BIC is calculated and its minimum over the investigated number of phases indicates an optimal number of phases. It was found to be four for both the modulus and the hardness EDF in Cu60Cr, as well as for the modulus EDF in Cu25Cr, and five phases for the hardness EDF in Cu25Cr. For a better comparison with the results from the LM fitting procedure, also the results of a three-phase distribution are analyzed for all investigated EDFs.

First of all, looking at the deconvolution results from the EM procedure in Tables B.5 to B.8, exactly one phase in each deconvolution (modulus or hardness, three-phase, four-phase or five-phase fitting function) fulfills the following conditions: it is the stiffest or hardest phase in the deconvolution, its area fraction is less or equal to 9 %, its standard deviation higher than a third of the phase mean value, and its mean modulus and hardness are largely above the mean modulus and hardness measured in the compacted Cr sample with ET experiments (below 400 GPa and 4.5 GPa for the modulus and the hardness, respectively).

An example of such a phase is the 3rd phase of the Cu25Cr modulus distribution analyzed by the EM procedure with 3 phases (see Table B.5). Its modulus is 731 ± 302 GPa for a phase fraction of 1.9 %. These very stiff or hard phases were not present in the analysis with the LM procedure or in the deconvolution of the CSM experiments, and thus are unlikely to describe a material mechanical phase, but are rather an artifact of the EM fitting procedure. In the following, the phases meeting the criteria listed above will

not be analyzed and the fitting results will be only displayed up to 350 GPa–400 GPa for the modulus and 3.5 GPa–4.5 GPa for the hardness.

The fitting results from various fitting procedures and with various phase number are plotted next to each other in Figure 3.12.

In Cu25Cr, the modulus phases between 100 GPa and 350 GPa are similar for both fitting algorithms and all numbers of phases (Figure 3.12a). The most compliant phase has a modulus of 145 ± 15 GPa and the stiffest phase of 260 ± 80 GPa. The introduction of a third phase in the fitting with the EM procedure leads to a phase with middle-stiff properties and with the smallest phase fraction of all three phases. The introduction of this phase refines the definition of the phase with the largest area fraction: its standard deviation and phase fraction are reduced, while the mean value is shifted in the opposite direction of the newest phase. The other previous phase also encounters these changes, but with less amplitude. The same phenomenon was also observed with the LM procedure (see Section 3.2.5).

For the modulus of Cu60Cr (Figure 3.12c), similar conclusions can be drawn as in Cu25Cr. The most compliant phase in Cu60Cr has 175 ± 25 GPa, and the next stiffest phase 310 ± 80 GPa. As with the LM fitting procedure, the introduction of a third phase in the fitting with the EM procedure introduces a stiffer phase around 375 ± 14 GPa with an area fraction smaller than 10 %.

In Cu25Cr, the hardness phases between 1 GPa and 4 GPa are similar for both fitting algorithms (Figure 3.12b); for a two-phase fit, the softest phase lies at 1.2 ± 0.2 GPa and the hardest phase at 2.6 ± 0.9 GPa. The introduction of a third or even a fourth phase in the deconvolution with the EM procedure divides the phases with the largest area fraction into two or three phases: the mean values of the phases are shifted away one from each other, while their standard deviations and phase fractions are reduced. Similar observations were made in the deconvolution with the LM procedure.

In Cu60Cr (Figure 3.12d), both fitting algorithms also provide similar phases. In the two-phase fit, the hardness of the softest phase lies at 1.50 ± 0.25 GPa

and at 3.2 ± 0.8 GPa for the hardest phase. When a third phase is introduced in the deconvolution, the hardest phase is divided into two smaller phases.
In general, the deconvolution phases are more similar for fits with the same number of phases and different fitting algorithms than with the same fitting algorithm and varying number of phases. For example in Cu25Cr, the hardness distribution *EM 3 Phases* on Figure 3.12b is more similar to *LM 2 Phases* than to *EM Opt. fit* in the investigated hardness range. The largest differences between the two fitting algorithms are, first, the presence (or absence) of a very stiff, or very hard, phase in each deconvolution, and second, the provision of the BIC to compare fit results with each other, either with a given number of phases or between the best fits with different number of phases.

3.2.7 Comparison of nanoindentation testing procedures

The optimum deconvolution results for the hardness and modulus distributions in both Cu-Cr composites, measured with the standard CSM (see Section 3.2.4) and ET nanoindentation experiments (see Section 3.2.5) were compared in Figure 3.13. Both distributions were measured at 1 µm depth and fitted with the EM procedure. The phase parameters for all fits are listed in Appendix in the Tables B.1 to B.4 for the standard CSM results and in Tables B.5 to B.8 for the ET results.
Based on the BIC, the optimal number of phases is two for the modulus and the hardness distributions in both Cu25Cr and Cu60Cr measured with standard CSM. The optimal number of phases in the ET experiments was either three or four, depending on the investigated distribution. Thus, the fits with either three or four phases from the ET experiments were compared to those with two or three phases from the standard CSM experiments.
Under the same criteria as in Section 3.2.6, the results of the ET nanoindentation deconvolutions in both Cu-Cr composites were only investigated up to a modulus of 400 GPa and a hardness of 4.5 GPa.

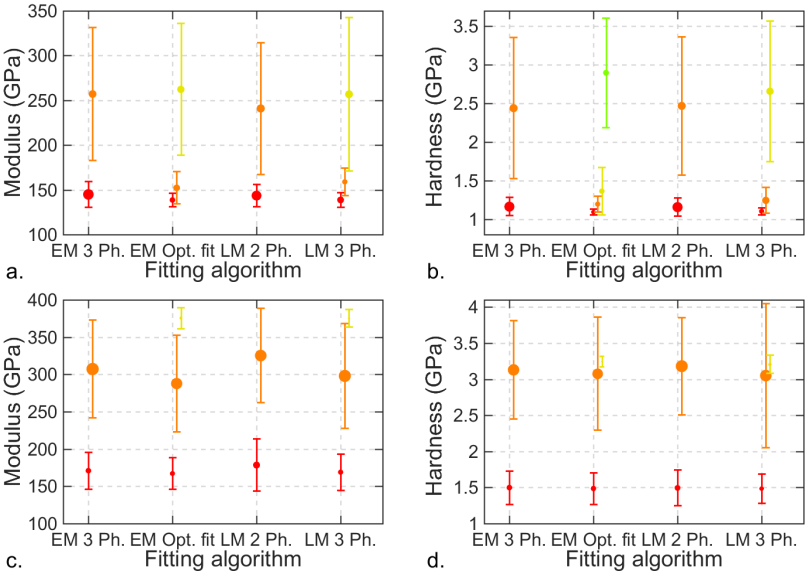

Figure 3.12: Comparison of (a, c) the modulus and (b, d) hardness deconvolution results from two different fitting algorithms (LM and EM) and two to four phases for (a, b) Cu25Cr and (c, d) Cu60Cr. For a better visibility, the phases that fulfilled the following conditions are not displayed: phase mean value larger than in the previously investigated Cr sample, standard deviation above a third of its mean value and area fraction below 9 %.

The presence of a very stiff or very hard phase in the modulus and the hardness distributions in the deconvolution results from the ET measurements in Cu25Cr represents the main difference with the results from the standard CSM distribution. Once this phase is removed from the analysis, the deconvolutions are very similar.

The main remaining differences are the larger standard deviations of the phases from ET measurements than from standard CSM. Comparing for example the deconvolutions from *CSM 2 Phases* and *ET 3 Phases* in Cu25Cr (Figure 3.13a), the mean modulus values of each phase are equal: around 145 GPa for the most compliant phase and around 260 GPa for the stiffest

phase. But the phases have higher standard deviations when derived from the ET than from standard CSM measurements: 14.2 GPa vs. 8 GPa for the most compliant phase and 74.2 GPa vs. 70 GPa for the stiffest phase.
Also the area fractions depend on the measurement technique. The most compliant and the stiffest analyzed phases in each deconvolution have a phase fraction of 62 % and 38 % when measured from the standard CSM modulus distribution and 58 % and 40 % from the ET distribution with three phases, respectively.
In Cu60Cr, the modulus deconvolutions show greater difference between the standard CSM and ET deconvolutions than for Cu25Cr (Figure 3.13c). The mean values of all phases are higher in the ET distribution than in the standard CSM distribution for the same number of analyzed phases.
A modulus variation greater than 100 GPa is also observed in the compacted Cr sample when measured with standard CSM (see Figure 3.5) and with ET experiments (see Figure 3.10). In comparison, the modulus of the Cu compacted sample does not show such a large difference with the nanoindentation method, and only varies between 125 GPa with standard CSM versus 120 GPa with ET experiments.
The reason for this observed behavior of the modulus in the compacted Cr sample and the samples with large Cr content might be that chromium has strain-rate dependent elastic properties, and that the standard CSM and ET indentation measurements represent very different strain rates. Indeed, the indentation rates were estimated as around 300 $\mathrm{nm\,s^{-1}}$ to 1000 $\mathrm{nm\,s^{-1}}$ in the ET experiments, and below 50 $\mathrm{nm\,s^{-1}}$ in the standard CSM experiments, thus with at least a factor 6 in the indentation rates of both measurement methods. This would also lead to large differences in the strain rates of the indented materials. Assuming that the stiffest phases of the Cu-Cr composites contain more Cr than the most compliant ones, the increase of their mean modulus with both the indentation rate and the Cr content of the sample could be explained by the higher influence of the indentation rate of the measurement on

Cr than on Cu. This must be considered in the choice of the nanoindentation method.
The hardness of the softest phase in the deconvolutions from both measurements has similar mean values in all Cu25Cr analyzes, as well as in Cu60Cr (Figures 3.13b and 3.13d). The standard deviations of these phases are however somewhat larger when measured from ET than from the standard CSM: compare for example *CSM 2 Phases* and *ET 3 Phases* in Figure 3.13d.
Also, the addition of a third phase in the deconvolution of distributions from ET measurements improves the resolution of the individual phase properties. For example, comparing *ET 3 Phases* and *ET 4 Phases* to *CSM 2 Phases* from the hardness distribution in Cu25Cr on Figure 3.13b, the mean value of the softest and hardest investigated phases in the *ET 4 Phases* deconvolution are closer to the mean values in *CSM 2 Phases* than the mean values in *ET 3 Phases* are. Also, in this example, the standard deviations of the softest and hardest investigated phases are reduced in the *ET 4 Phases* deconvolution compared to those of *ET 3 Phases*.

3.3 Discussion

3.3.1 Relation between microstructure and mechanical properties

Shallow indents were made around a Cr particle in the Cu25Cr sample (see Section 3.2.2). The influence of the Cr phase is clearly visible in the load-displacement curves, as well as in the modulus and hardness evolution over indentation depth (see indent 7 in Figure 3.4b). The hardness can even detect indents located only partially on a hard phase: indents 3 and 4 in Figure 3.3 show a small peak of hardness at very low depths in Figure 3.4b.
Analyzing the mechanical properties measured at indent 7, the plateau modulus at shallow depths, typ. below 500 nm is in the same range as the modulus of Cr (see Table 3.1). However, the hardness of the Cr particle in the com-

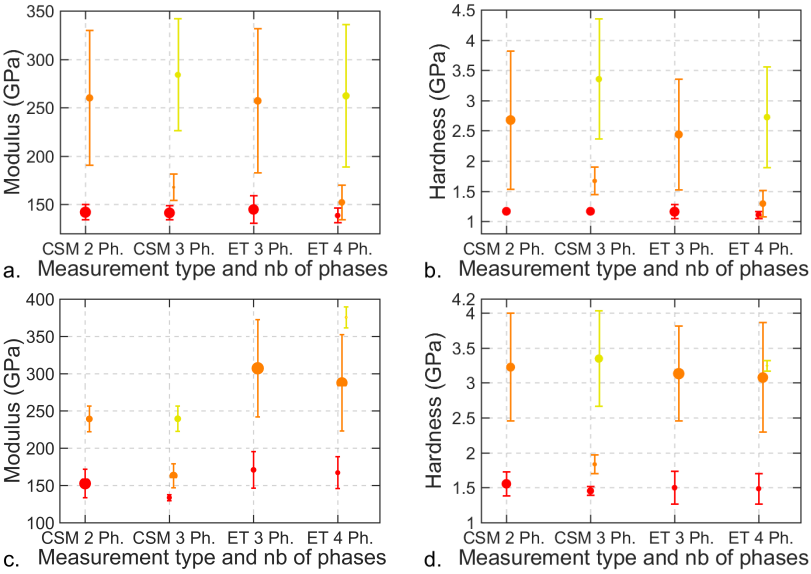

Figure 3.13: (a, c) Modulus and (b, d) hardness deconvolutions from standard CSM and ET nanoindentation measurements at 1 µm indentation depth in (a, b) Cu25Cr and (c, d) Cu60Cr. The EM fitting procedure with two to four phases was used. For a better visibility, the phases that fulfilled the following conditions are not displayed: phase mean value larger than in the previously investigated Cr sample, standard deviation above a third of its mean value and area fraction below 8 %.

posite at shallow depths is much lower than the hardness of the compacted Cr sample: at 500 nm, the hardness in the compacted Cr is around 3.7 GPa, and 2.2 GPa in the Cr particle of Cu25Cr. This could be explained by the influence of the Cu neighboring phase on the measured hardness, acting like a soft substrate for the hard Cr film in Cu25Cr.

Despite a Cr particle thickness of around 2 µm, the modulus and hardness of indent 7 deviates largely from the Cr properties at a depth of 200 nm. This depth corresponds to a depth over thickness ratio of 10 %. This means that neither the Buckle's rule of thumb of 10 % [118], nor the criterion for a ratio of the indentation depth over the particle thickness proposed by Durst

et al. [76] can be applied here for determining the hardness of this Cr film on the softer Cu substrate.

One difference between this experiment and the simulation from Durst et al. [76] is the larger height to diameter aspect ratio of the Cr particle near the analyzed indent, compared to 0.05 for the particles simulated in [76]. Indeed, the particle ECD at the surface is 14.8 µm (see Figure 3.3a) and its aspect ratio is estimated as 0.14. However, following the simulations in [76], an increased aspect ratio should actually increase the depth-over-thickness ratio for which the particle's properties can be estimated accurately.

Another possible reason for the discrepancy between the simulation and the experiment is the difference in material properties. A hard particle or thin film on a soft substrate were simulated, with both materials having the same elastic modulus and a factor of two in yield strength, thus, also in hardness; though in this experiment, the Cr particle is twice as stiff as, and three times harder than the Cu substrate (see Figure 3.5).

3.3.2 Single phase measurements

In both Cu25Cr and Cu60Cr, some indents from standard CSM experiments were assigned to either a Cu or a Cr phase, depending on their location from optical microscopy and their indentation curves (see Section 3.2.3). The others had ambiguous location and/or indentation curves and were not considered in this analysis.

However, the Cu-rich and Cr-rich phases of the composites as defined in this analysis behave differently than the Cu and Cr compacted samples (see Figure 3.5). Possible reasons for the different behaviours are that the phases were not determined from perfect measurements at infinitely shallow depths and that the materials were probably not perfectly biphasic (see e.g. Fig.1 in [101]). Therefore, the phases seem to mechanically interact with each other, and the mechanical properties of the individual phases of the composites cannot be directly measured from such experiments.

Young's modulus

The smallest modulus for the Cu phase was found in the compacted Cu sample (Fig 3.5), followed by Cu60Cr and finally Cu25Cr. The highest modulus of the Cr phase was found in the compacted Cr sample, followed by the Cu60Cr and the Cu25Cr samples. The reasons for the modulus differences depending on the Cr content could be the diffusion of one phase into another, the presence of foreign particles or pores, or the influence of the surrounding material.

The amount of chromium diffusing into copper as solid solution is estimated as 0.4 % [111]. Considering the small differences in lattice parameters (2.88 Å and 3.61 Å for Cr and Cu, respectively) and an estimated amount of Cr in the Cu lattice of 0.4 at-% to 3 at-% [110], the effect of the Cr solid solution on the Cu lattice is small and can be very roughly estimated to be limited to a reduction of 0.1 % to 0.6 % of the Cu lattice parameter, according to Vegard's law [119]. Following [120], a smaller lattice constant would lead to a higher Young's modulus. Thus, the Cr solid solution does surely contribute to the modulus difference of 12.5 % between the Cu phase in the Cu60Cr and the Cu composites.

Another factor is the presence of Cr particles in the Cu phase [111]. They are estimated to represent 1 % to 3 % of the volume and have a diameter of 100 nm to 200 nm [111]. Applying the lower and upper rules of mixture on a composite made from a Cu matrix and Cr particles, the modulus increase of the Cu phase due to the presence of Cr particles would be between 1 % and 3 %.

Finally, the influence of porosity on the modulus of the Cu phase in Cu-Cr composites needs to be considered. Indeed, the relative density of the Cu sample is only 97.7 % (see Table 3.2), while the relative density of the Cu-Cr composites is as high as 99.4 % in Cu25Cr and 98.3 % in Cu60Cr. Thus, the porosity in the Cu-Cr composites is lower than in the compacted Cu sample. Moreover, it is concentrated in the Cr phase or at the interfaces [111]. After

Lebedev et al. [121], "a reduction of the modulus due to the porosity can be well approximated by a simple formula":

$$E = E_{bulk} \exp(-\alpha \Delta p/p) \tag{3.2}$$

where E_{bulk} is the modulus of the bulk, poreless material, and α an experimental constant. Assuming α equal to -4.0, as calculated from the experiments on Cu from Lebedev et al. [121], the actual porosity of the compacted Cu sample would decrease its modulus by up to 9 % compared to that of bulk copper. Thus, the difference in porosity of the Cu phase in the compacted Cu sample and in the Cu-Cr composites could explain most of the modulus differences observed.

Furthermore, the modulus in the Cu phase varies by up to 18 % comparing Cu25Cr and Cu60Cr in the depth range between 250 nm and 1900 nm (see Figure 3.5a). Thus, the neighboring Cr phase does not seem to influence the modulus estimation in the Cu phase of the composites, even in the composite with highest Cr content, or at the highest investigated depths. This indicates that despite the lower number of investigated curves in Cu60Cr (only 5 indents could be assigned to the Cu phase of the Cu60Cr sample, and 10 for Cu25Cr), and the lower Cu phase fraction in the composite, the modulus of the Cu-rich phase can be determined accurately with nanoindentation in selected locations.

The Cr-rich phase however, shows large differences in the evolution of the modulus over depth between the investigated samples (see Figure 3.5a). First, it should be noted that, as the nanoindentation tip has been calibrated in the range of 200 nm to 2000 nm only, the deviations of the calibrated tip geometry for depths below 200 nm would impact the measured hardness and modulus values, but with a consistent error for all indents. The modulus of the compacted Cr sample is constant with the indentation depth, which is expected, considering the sample homogeneity. The modulus also corresponds to the literature value for Cr, as summarized in Table 3.1. The modulus of

the Cr phase (around 300 GPa) is not reached at depths higher than 200 nm, but approaching modulus values are reached in all three samples (Cu25Cr, Cu60Cr and the compacted Cr) at a depth around 100 nm. For larger indentation depths, the modulus of the Cr phase decreases in the Cu-Cr composites, whereas it remains rather constant in the compacted Cr sample. The modulus decrease with depth is larger in the samples with higher Cr content in the composite.

As the diffusion of Cu into Cr is negligible [110], and no Cu particles were found in the Cr phase [111], one can exclude that this behavior comes from Cu impurities in the composites Cr phase. However, the influence of the neighboring softer Cu phase should influence the determination of the mechanical properties of the harder Cr phase in the composites, in particular at larger depths h compared to the particles' characteristic size D. Indeed, the mechanical properties of a single phase can only be accurately determined for a phase size over indentation depth ratio $\frac{D}{h}$ higher than 10 [97].

The characteristic size of the Cr particles in Cu25Cr and Cu60Cr is estimated by their mean diameter. Both particles have bimodal diameter distributions (Table 3.6), with the smallest particles having a mean diameter of 25 µm in both samples. According to the phase separation criterion from [97], indentation depths below 1.7 µm to 2.5 µm should resolve the mechanical properties of the Cr particles only. However, a deviation of more than 10 % from the elastic properties of the compacted Cr sample is observed for depths larger than 600 nm in Cu25Cr, and 1200 nm in Cu60Cr. The discrepancy here might come from the actual shape of the Cr particles, which are not spherical but rather in a coin-shape [111]. Assuming that the criterion of $\frac{D}{h} > 10$ holds, the mean thickness of the Cr particles can be estimated as 6 µm in Cu25Cr and 12 µm in Cu60Cr, and the particles have an aspect ratio of 2 to 4, depending on the sample.

An additional interesting question would then be if the indentation depth was large enough in these experiments to measure the homogenized modulus of the Cu-Cr composites, i.e. if both phases are so small compared to the mea-

surement depth that the microstructure does not influence the modulus measurement (see e.g. [1, 122]). The homogenized modulus can be estimated based on the Voigt and Reuss rules-of-mixture and is in the range of 151 GPa to 170 GPa for Cu25Cr and 195 GPa to 220 GPa for Cu60Cr. The averaged modulus values just below 2 µm depth were 187 GPa in Cu25Cr and 224 GPa in Cu60Cr (Fig. 3.5). Thus, the depth for which the homogenized modulus can be measured is probably larger than 2 µm and has not been reached in these measurements.

Hardness

Composites versus compacted samples In the single-phase measurements, the hardness is higher in the composites than in the compacted samples (see Figure 3.5b).

First, as shown in Section 3.2.1, the surface tilt influences the comparison of the hardness distributions between the samples, as it leads to an underestimation of the hardness for some samples. The variation of hardness between the single phases of all samples is underestimated, as the measured hardness is underestimated by 19 % in both phases from Cu60Cr, somewhat less underestimated in both phases of the less tilted Cu25Cr sample, and quite accurate for both, even less tilted, compacted Cu and Cr samples.

For the Cu-rich phase, the hardness variation can be correlated to the fraction of the harder Cr-phase in the sample: the hardness of the Cu-phase in Cu60Cr is higher than in Cu25Cr, and the hardness of both samples are higher than in the compacted Cu sample. Material size effects might also explain the hardness differences measured in the samples: when the Cr content increases, the characteristic size of the Cu-rich phase decreases. Interestingly, this does not hold for the Cr-rich phase, where the composite samples show harder Cr-rich phase than the compacted Cr sample, and the Cr-rich phase is harder in Cu60Cr than in Cu25Cr.

Furthermore, when the Cr volume fraction increases, the distribution of the Cr particles diameter varies by less than 20 % (see Table 3.6). In Figure 3.1b, one can clearly see the Cr particles boundaries, where the porosity concentrates, probably as a consequence of the FAST material production. The particles boundaries are not so clearly visible in the Cu matrix, neither in Cu60Cr nor in Cu25Cr.
Finally, the phase interface density increases with the sample Cr content [111], which leads to a harder material. Thus, the microstructure of the composites, and in particular of Cu60Cr, might explain the differences in the measured hardness.

Variation of the hardness with indentation depth As shown in Figure 3.5b, the hardness of all samples decreases with increasing indentation depth, in particular in the Cr-rich phase. Some microstructure-related effects and the indentation size effect play a role for the measured hardness, and are detailed below.

Microstructure-related size effects The grain size is known to play a role on the hardness measured in metals. In general, the hardness increases with decreasing grain size (See Section 2.1.1). In the Cu25Cr sample, the FIB cross sections showed that the grains possess a different size on the surface compared to that of the unprepared material at higher depths (see Figure 3.4a). The Cu grains were estimated to have a mean size of 400 ± 100 nm within the first micrometer from the surface and of 5 µm at higher depths, as measured on a cross section next to the location shown in Figure 3.4a. The difference in grain size between the sample surface and the deeper material is probably related to the deformation layer induced by the mechanical polishing of the samples, which is known to "work-harden the material in the near-surface region" [96]. Yet, the size of the deformation layer at the surface, as well as the effects of polishing on each single phase, may vary with

the sample composition and morphology and thus have an influence on the measured hardness.

According to the Hall-Petch model (Section 2.1.1), a reduction of the grain size of Cu from 5 µm to 400 nm would lead to a hardness increase of 0.35 GPa. For a grain size decrease by 200 nm from 500 nm, the hardness would increase by 0.13 GPa. Thus, a different mean grain size in the near-surface region, compared to that deeper in the sample, could contribute to the variations in the hardness observed in the individual samples' phases over the indentation depth, as well as between the samples.

Besides the presence of a deformation layer near the surface, the measured hardness can be influenced by the phases actually being heterogeneous at the rather small investigated scale of 0.2 µm to 2 µm, for example through solid solution or precipitation. If Cu does not diffuse into Cr [110], Cr can diffuse into the Cu phase during the sample preparation per FAST and precipitate during the sample cooling, as suggested by v. Klinski [111].

Considering a size of 100 nm to 200 nm, and atomic fraction of 0.4 at-% (or 0.41 vol-%) for such precipitates [111], the hardness increase due to Cr precipitation in the Cu phase is limited to around 2 MPa to 83 MPa, using the Orowan [123] and the Ashby-Orowan theories [124], with a Cu shear modulus of 48.3 GPa[1], and Burger's vector of 2.55 Å[2]. As the exact size distribution of these particles is unknown, also smaller particles (around 50 nm diameter) with the same atomic fraction might be encountered. Then, the hardness increase is in the range of 6 MPa to 200 MPa. Thus, this hardening mechanism surely contributes to the difference of 500 MPa in the single-phases hardness between the Cu phase of Cu25Cr and the compacted Cu sample.

[1] Calculated using $E(1+\nu)/2$ with E and ν from Table 3.1

[2] `https://www.copper.org/resources/properties/atomic_properties.html`, visited on 23rd March 2018

Indentation Size Effect The Indentation Size Effect (ISE) is described as an increase of the hardness with decreasing indentation depth in single crystals, and is particularly relevant for depths below 1 µm [125]. According to Pharr et al. [125], the ISE "can be observed only when the specimen dimensions approach the average dislocation spacing and when plastic deformation is controlled by a limited number of defects".
In this work, a decrease in hardness from 2.5 GPa at 2 µm to 6 GPa at 250 nm was observed for the Cr compacted sample (Fig. 3.5). But also the Cu compacted sample shows a size effect, as its hardness increases from 0.7 GPa at 2 µm to 1.5 GPa at 250 nm (Fig. 3.5).
As suggested by Nix and Gao [126], the hardness increases with decreasing indentation depth, as: $(\frac{H}{H_0})^2 = 1 + \frac{h^*}{h}$, with the hardness H, the indentation hardness at infinite depth H_0, the indentation depth h and h^* a characteristic length scale. This relationship implies that a plot of H^2 as a function of $\frac{1}{h}$ should be linear. H_0 is the square root of the intercept and h^* the slope divided by the intercept, respectively.
The Nix-Gao model appears to describe the behaviour of the compacted Cu and Cr samples (Figure 3.14): a straight line fits the whole indentation depth range. For the Cu compacted sample, the Nix-Gao fit parameter H_0 is near to the values found in the literature (Table 3.10). As a consequence, the depth of investigation does have an influence on the measured hardness, and for the investigation of the composite influence on the hardness properties of a single phase, the investigated depth should be limited to depths above 500 nm to 1000 nm, where the ISE is weaker.

3.3.3 Determining phase properties in Cu-Cr composites

Comparison of nanoindentation techniques

First, independent of the nanoindentation testing procedure, the impact of the surface quality on nanoindentation measurements should not be underestimated. In particular, a higher surface roughness leads to an increase in the

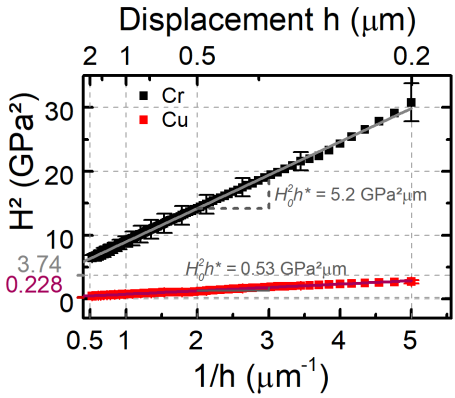

Figure 3.14: Nix-Gao plot for investigation of the ISE in single phase indents of compacted Cu and Cr samples.

Table 3.10: Indentation Size Effect parameters from fits over whole indentation range in the compacted Cu and Cr samples and from literature, when available.

Fitted phase	H_0 (GPa)	h^* (μm)
Compacted Cu sample	0.48	2.3
Compacted Cr sample	1.93	1.4
Cu [127–132]	0.5 to 0.675	0.2 to 0.7

standard deviation of the phase properties, as in the modulus deconvolutions from CSM and ET in Cu25Cr (Figure 3.13a).

The sample tilt also leads to underestimating the hardness by up to 20 %. As the Cu60Cr sample is more tilted than Cu25Cr, the hardness differences of similar phases are underestimated, when the composites are compared. Besides the sample tilt, these differences could also come from an increased influence of the phase with the largest phase fraction, i.e. Cu in Cu25Cr *softens* both phases, and Cr in Cu60Cr *hardens* them.

Both nanoindentation testing procedures have advantages and drawbacks. For the CSM, the main advantage is the possibility to decide, a posteriori, the

indentation depth at which the distribution is analyzed. However, the rather long testing time does not easily enable testing a large number of locations, which is required to accurately determine the phase properties, in particular the phase fractions. Also, the phases from the deconvolution of the CSM modulus measurements correlate well with the properties of both compacted samples. For instance, the Cu-rich phase of the Cu-Cr composites has a modulus around 140 GPa to 160 GPa in the composite samples. The phase with the second largest fraction has a mean value around 240 GPa to 260 GPa and is, thus, assumed to be a Cr-rich phase.

Conversely, the ET testing procedure does only measure the mechanical properties at a given depth. It has the advantage of measuring a larger number of locations in the same amount of time compared to the standard CSM technique and, thus, to facilitate the determination of the phase properties. However, the ET procedure applies high strain-rates, and may not be suitable for materials showing strain-rate dependent material properties, such as Cr or viscoelastic materials. For example, the modulus of the compacted Cr sample is much higher when measured with ET than with CSM. The high strain rates probably also explain the large differences in the mean modulus of the Cr-rich phase from the deconvolution of Cu60Cr, i.e. around 300 GPa with ET and around 250 GPa when measured with CSM.

Comparison of methods for analyzing indents

SNT provides a quick and reproducible deconvolution of the mechanical properties of Cu-Cr composites. Two phases are expected to be found, with mean modulus and hardness between the modulus and hardness of the compacted samples of Cu as lower bound and Cr as higher bound.

From the modulus and hardness values presented in Section 3.2.4, the phase (or phases) with lowest mean modulus or hardness are assumed to present a higher content of Cu, and are thus assigned to the Cu-rich material phase. Similarly, the stiffest or hardest phases present a higher Cr content and are

Table 3.11: Cu-rich and Cr-rich phase properties from SNT of the CSM experiments, compared to the Cu-rich and Cr-rich phases mean properties from single phase experiments (selected indents) in the same Cu-Cr composites samples. All measurements were done at 1 µm depth.

		Property	
		Modulus (GPa)	Hardness (GPa)
Cu-rich phase			
Cu25Cr	From SNT	142 ± 8	1.20 ± 0.03
	Selected indents	136 ± 7	1.18 ± 0.07
Cu60Cr	From SNT	153 ± 19	1.60 ± 0.20
	Selected indents	131 ± 8	1.40 ± 0.07
Cr-rich phase			
Cu25Cr	From SNT	260 ± 70	2.7 ± 1.1
	Selected indents	231 ± 34	3.6 ± 0.9
Cu60Cr	From SNT	239 ± 17	3.2 ± 0.8
	Selected indents	257 ± 7	3.8 ± 0.7

assigned to the Cr-rich phase. The modulus and hardness values measured in single material phases of each sample (see Section 3.2.3) are then compared to those of the Cu-rich and Cr-rich phase properties determined from deconvolution of the CSM experiments in Table 3.11.

The deconvoluted phases show an increased influence of the neighboring second phase compared to the results from selected indents. This can be seen in particular in the modulus of both phases, and in the hardness of the Cr-rich phase.

In the Cu-rich phase, the modulus of all phases determined from SNT and the standard deviation are higher than those from the single phase experiments. This holds in particular in Cu60Cr, the composite with higher Cr content. Thus, the SNT does not only resolve the Cu-rich phase properties, but also measures the stronger Cr-rich phase.

In the Cr-rich phase, the modulus shows a higher standard deviation when determined from SNT. Interestingly, in Cu25Cr, this phase modulus is higher when determined from SNT as when determined from selected indents, whereas the contrary happens for Cu60Cr. Yet, if the number of indents are comparable between both measurement methods (5 to 10 in the single phase measurements, and 25 for both phases in the SNT), the exact microstructure below the indents is different. Also, the neighboring Cu-rich phase influences the Cr-rich phase properties determination in both analysis methods, as the modulus measured in the Cr compacted sample was 276 ± 10 GPa, i.e. higher than all averaged moduli in the Cr-rich phases of Cu25Cr and Cu60Cr.

Considering the hardness, the averaged values from SNT are less scattered compared to those from the single phase measurements, i.e. the Cu-rich phase hardness is higher and the Cr-rich phase is lower in the SNT. This clearly highlights that the neighboring phase influences the determined properties in the SNT, even after deconvolution. This effect is less important at smaller indentation depths. Table 3.12 presents the same experiments results as Table 3.11, but at a depth of 500 nm.

At 500 nm indentation depth, i.e. below the phase separation criterion as determined in the Section 3.3.2, the accuracy of the SNT is improved compared to the phases as determined from selected indents. The phases have lower standard deviations of their measured modulus and hardness, in particular the Cu-rich phases, and the mean values from both analysis methods are nearer to each other than at 1 µm.

Comparison of fitting procedures in the SNT

Regarding the statistical analysis, both fitting procedures present some interesting features and some issues. The major interest of the EM fitting procedure is the calculation of the BIC. The BIC enables to select the optimal fit out of fit replicas with different sets of random parameters and a given num-

Table 3.12: Cu-rich and Cr-rich phase properties from SNT of the CSM experiments, compared to the mean properties from single phase experiments (selected indents) in the same Cu-Cr composites samples. All measurements were done at 500 nm depth.

		Property	
		Modulus (GPa)	Hardness (GPa)
Cu-rich phase			
Cu25Cr	From SNT	143 ± 6	1.50 ± 0.04
	Selected indents	139 ± 2	1.49 ± 0.04
Cu60Cr	From SNT	148 ± 11	1.9 ± 0.1
	Selected indents	137 ± 8	1.9 ± 0.1
Cr-rich phase			
Cu25Cr	From SNT	263 ± 48	3.4 ± 1.1
	Selected indents	256 ± 21	4.2 ± 0.8
Cu60Cr	From SNT	254 ± 21	3.8 ± 1.0 4.20 ± 0.04
	Selected indents	278 ± 5	4.5 ± 0.5

ber of phases, and to also select the best number of phases (as in e.g. [103]). A more detailed comparison of both fitting procedures can be found in Appendix A.

In the following, the surface fraction estimations from statistical analysis from both CSM and ET nanoindentation experiments and from optical microscopy are compared (Table 3.13).

Using the Cr-rich phase fractions measured by optical microscopy as a reference, the statistical analysis of the modulus from ET measurements seems to provide more reliable phase fractions (see Table 3.13) than the CSM experiments. The lower number of indents in the CSM experiments might be the reason for the large variations between the phase fractions from the SNT analysis based on CSM measurement and from optical microscopy. Also

Table 3.13: Cr-rich phase fractions estimated in Cu25Cr and Cu60Cr from both optical microscopy and SNT of the modulus and hardness distributions, measured via ET and CSM methods. When more than two phases describe the composite mechanical properties distribution, the sum of the phase fractions of the two stiffest phases were added to estimate the Cr-rich phase fraction.

Phase fraction (%)	SNT				Optical
Distribution	Modulus		Hardness		
NI method	CSM	ET	CSM	ET	
Cu25Cr	38	37 to 43	53	38 to 43	35
Cu60Cr	34	63 to 70	48	64 to 82	65

small variations in the microstructure between the two locations investigated by nanoindentation and optical microscopy might contribute to the differences.

Independent of the measurement method, the analysis of the hardness data provides higher values of the Cr-rich phase fraction than the analysis of the modulus data. As both distributions come from the exact same measurements, in particular the same locations, the hardness seems to more accurately detect the presence of a harder phase under an indent than the modulus the presence of a stiffer phase.

3.4 Summary

3.4.1 Applicability of the SNT on bi-metal composites

The applicability of the SNT to characterize the microstructure of bi-metal composites has been successfully investigated.

Both investigated Cu-Cr composites present a bi-phased microstructure composed of a (softer) Cu-rich and a (stiffer and harder) Cr-rich phase, which was confirmed by the SNT in most cases. However, in some analyses, a third

phase was found in the deconvolution results from SNT, which then refined the properties determined for one of the two phases.
In general, the SNT can measure the modulus of the Cu-rich phase quite accurately, but with a large standard deviation, whereas it provides less accurate results for the Cr-rich phase. Also, the SNT is well indicated to measure the hardness of the softer Cu-rich phase, but underestimates that of the Cr-rich phase. This corroborates the results from the FE study performed by Durst et al. [76] on the hardness measurement of a film on a substrate.
Finally, at the relatively large indentation depth compared to the characteristic sizes of the mechanical phases, the modulus and hardness measured in both phases are better resolved when the investigated phase has a larger relative fraction in the investigated composite than the contrary.

3.4.2 Conclusions on the SNT analysis

Some more general conclusions about the SNT can be drawn from this study. In the SNT analysis, the execution of the nanoindentation experiments as well as the experiment analysis play a more important role than the choice of the statistical fitting procedure in achieving a reproducible and accurate determination of the mechanical phases' properties. The nanoindentation testing procedure and its analysis must be adapted to the sample microstructure to meet the requirements of the statistical analysis.
Indeed, if, a priori, both CSM and ET nanoindentation techniques can be suitable to test heterogeneous materials, ET experiments have the big advantage of providing more data in a short time. They should be avoided, however, for materials with strain-rate dependent mechanical properties. Moreover, besides the NI technique, the choice of the indentation depth is the most important parameter of the experimental part of the SNT. Finding the best compromise between the contradictory constraints coming from the sample microstructure and the surface quality is not straightforward.

However, whenever the microstructure of the material is not well-known or can't be investigated thoroughly previous to the experiments, an estimate on the characteristic size of the smallest phase can be determined e.g. by comparing with SNT the phase deconvolutions of successive ET experiments series at different indentation depths. Then, the characteristic size of a phase can be derived from the largest indentation depth providing consistent deconvolution results.

Also, regarding the statistical analysis, it was shown that the use of the BIC to compare fit results does improve the estimation of the number of phases. But, independent of the information provided by the BIC parameter, the number of phases must be carefully considered. Indeed, in a statistical analysis, the presence of a statistical phase at the edges of the distribution, with a large ratio of standard deviation to mean value and a small phase fraction, might actually capture some experimental noise. On the other hand, it might also help improve the determination accuracy of the properties of the remaining phases.

Finally, it has been shown from the comparison of the phase fractions of the Cu-Cr composites that the hardness seems to more accurately detect the presence of a harder phase under an indent than the modulus the presence of a stiffer phase. Thus, whenever possible, both the hardness and the modulus distributions should be investigated via SNT to determine the number of phases in the material.

4 Nanoindentation of *Passiflora discophora* attachment pads

Various attachment strategies are used by climbing plants [133]. Unlike most Passifloraceae, which climb using coiling tendrils [133], the passionflower *Passiflora discophora* uses dedicated organs for climbing, called attachment pads [24]. The pad morphology has been investigated by Bohn et al. [24], and revealed a heterogeneous structure made of two main tissues: "a lignified and thus stiff central tissue surrounded by less stiff parenchyma and pad tissue". This study aims to better understand the structure-function relationship of the attachment pads, by investigating Young's modulus of both tissues with nanoindentation. The challenge of the nanoindentation measurement lies in testing the small, soft, cellular, and heterogeneous structure of the attachment pads with a statistically sufficient number of data. From the nanoindentation results, a pad model is proposed and analyzed using Finite-Element (FE) modeling study to gain insight into the relationship between microstructure and stress distribution in the pad when the pad branchlet is pulled in the direction of the plant stem.

4.1 Experimental details

4.1.1 Material description and sample preparation

Passiflora discophora attachment pads (see Figure 4.1) in the dried state were collected from plants growing on wood substrate in the Botanic Garden of the Freiburg University in Germany [24]. The mean diameter of the pads was 1.63 ± 0.50 mm [24]. Large specimens were chosen for the microscopy anal-

ysis and mechanical testing, as a larger size indicates a fully developed pad, and also offer a larger area for testing. The pads were embedded in paraffin wax (Surgipath® Paraplast® tissue embedding medium, Leica Biosystems Nussloch GmbH, Germany) and glued with the same wax to an aluminum cylinder. The wood substrate was glued parallel to the sample holder surface. The sample was cut parallel to the sample holder surface with a sledge microtome (Leitz™ 1400, Germany) to obtain smooth cross sections for microscopy and nanoindentation experiments. After a cross section in one sample was tested, the sample was cut again removing the already tested layer, revealing a new cross section of the pad, parallel to the previous one and closer to the substrate.

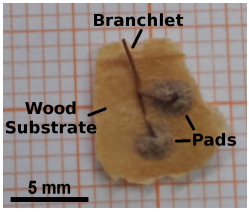

Figure 4.1: Two *Passiflora discophora* attachment pads, as received. They are attached to a wood substrate.

4.1.2 Microstructure investigations

An optical microscope (Nikon Eclipse LV150N) was used for visual control of surface quality prior to mechanical testing and imaging the microstructure. Additionally, micro computed tomography (µ-CT, scan and reconstruction by RJL Micro & Analytic GmbH, Karlsdorf-Neuthard, Germany) was used to investigate the three-dimensional microstructure of a pad. A major advantage of this method is that it is non-destructive and not restricted to conductive materials. As the scan magnification is directly related to the distance between the sample and the source, the sample must be placed as close

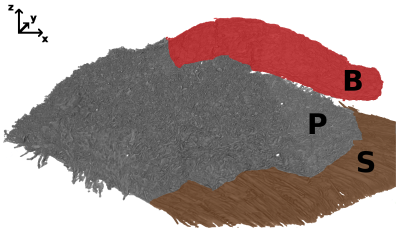

Figure 4.2: 3D reconstruction of a *P. discophora* attachment pad (P) from a µ-CT scan with a resolution of 0.65 µm/voxel. The x-axis indicates the branchlet (B) main orientation and the z-axis the orientation perpendicular to the (wooden) substrate (S).

as possible to the X-ray source to increase the magnification[1]. Considering also the fixed opening angle of the source, the smaller the sample size, the closer the sample can be placed to the source and the higher the resolutions that can be achieved. However, smaller pads may not be fully developed or may possess smaller cells. Thus, a scan of a *Passiflora discophora* attachment pad with a diameter around 1.8 mm was done, which enabled to achieve a high resolution of 0.65 µm/voxel (see Figure 4.2). After 3D reconstruction, the microstructure of the sample was investigated using the software package Avizo Standard V. 8.1 (FEI®, Hillsboro, Oregon, USA).

Additionally, the area and the position of every closed cell were determined in two perpendicular cross sections scanned with µ-CT. Therefore, the binarization and watershed algorithms from image editing software ImageJ (Rasband, W.S., U. S. National Institutes of Health, Bethesda, Maryland, USA) were used to separate adjacent cells. Then, the center of mass, the area, the minor and the major length of the cells are measured with ImageJ, as well as the orientation of the major axis of the cells. Using the area, also the cells Equivalent Circle Diameter (ECD) was calculated.

[1] See Texas Geosciences, *Resolution and Size Limitations [of CT]*, `http://www.ctlab.geo.utexas.edu/about-ct/resolution-and-size-limitations` accessed on 18th April 2018

4.1.3 Nanoindentation procedure and statistical analysis

To investigate the properties of the pads of the climbing *P. discophora*, the tissue of one pad was investigated with nanoindentation. A diamond conical tip with a flat end of 15 µm diameter and an angle of 60° was used. The tip Young's modulus and Poisson's ratio were 1141 GPa and 0.07, respectively. Nanoindentation analysis parameters ε and β (see Section 2.2.1) were set to 1.

During the approach and the loading segments, the standard CSM nanoindentation method was used at frequency of 45 Hz and with a harmonic displacement amplitude of 2 nm. The sample was loaded at a rate of $1\,\mathrm{mN\,s^{-1}}$ until a load on sample of 10 mN was reached. Then, the indentation modulus was averaged over an applied load range between 5 mN and 9 mN. This accounts for the large depth range reached by the indenter for various indent locations. The surface detection was manually corrected for each indent with the criterion that the load on sample versus displacement slope is $200\,\mathrm{N\,m^{-1}}$. The thermal drift was not corrected for these samples, as the contact area was nearly constant with the contact depth and the visco-elasto-plasticity of the material could influence the thermal drift measurement [82].

Six successive cross sections of the pad were investigated, cut at distances of 20 to 100 µm between them (Figures 4.3a to 4.3f). An average of 150 ± 33 indents were performed per cross section, as the total surface available varied with the cross section position in the pad. It was ensured that the distance between two indents was at least 30 µm (twice the smallest punch diameter) in every planar direction, to prevent testing of an already plastically deformed area.

In addition, the cross section of a branchlet was prepared and tested with the same nanoindentation procedure, but perpendicularly to the branchlet longitudinal axis, in the direction going from the plant stem into the pad (Figure 4.3g). Due to its smaller cross section, only 60 indents were performed on the branchlet. The indentation modulus of the pad cellular struc-

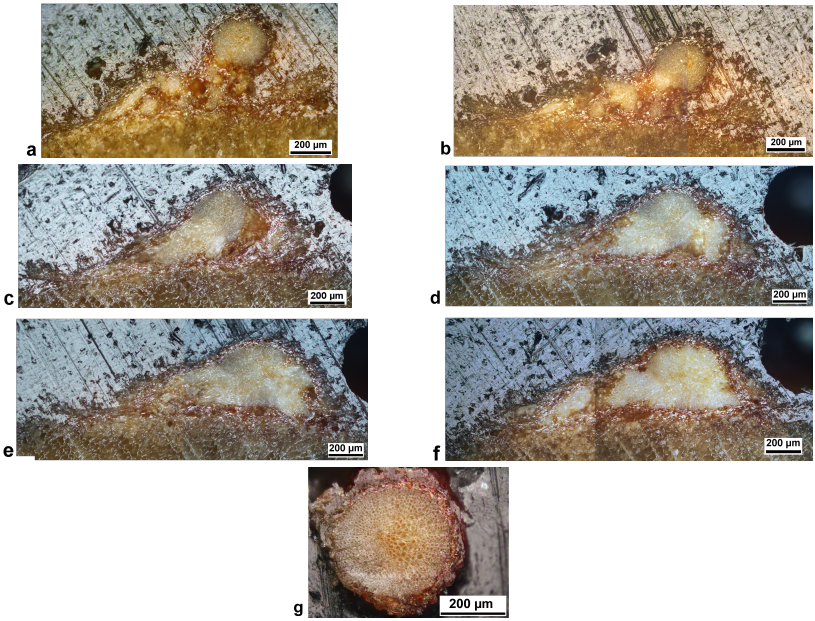

Figure 4.3: *Passiflora discophora* attachment pad cross sections (a) 1 to (f) 6 and (g) branchlet cross section from embedded samples, light microscopy.

ture was evaluated assuming Poisson's ratio ν of 0. To calculate the Young's modulus with a different Poisson's ratio, the following relation can be used: $E_\nu = (1-\nu^2)E_{\nu=0}$

The modulus values were analyzed by the statistical nanoindentation technique. The Levenberg-Marquardt fitting algorithm (see Section A.1.1) was used to fit the empirical modulus distribution in each cross section with a sum of two to four Gaussian distributions, depending on the investigated pad (or branchlet) cross section.

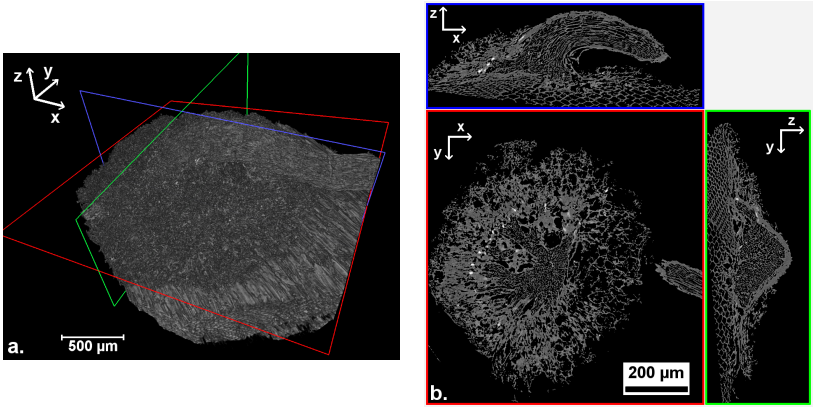

Figure 4.4: (a) 3D rendering of a *P. discophora* pad from the µ-CT scan. The branchlet lies along the x-axis and the the z-axis is perpendicular to the substrate. (b) Three cross sections of the same pad µ-CT scan, along the planes shown in (a): x-z on the top, x-y on the bottom left and y-z planes on the bottom right.

4.2 Results

4.2.1 Microstructure of the pads

The *Passiflora discophora* attachment pads are composed of different tissues [24]. A 3D reconstruction of the pad investigated with µ-CT (Figure 4.4a) and cross sections in different planes (Figure 4.4b) give a first overview of the pad complex microstructure. The branchlet lies along the x-axis and the the z-axis is perpendicular to the substrate.

Cross sections of interest with two different pad orientations are presented in Figure 4.5. In Figure 4.5a, the pad (**P**) cross section is aligned with the branchlet (**B**) and perpendicular to the substrate (**S**). In Figure 4.5b, the cross section is parallel to both the substrate plane and the branchlet axis.

In the pad main body, two different tissues might be identified *a priori* based on the light microscope pictures and the µ-CT scan results. First, the tissue layer at the periphery, which appears foamy and does not exhibit a particular arrangement of the cells at first sight, in particular in the x-y cross section

(Figure 4.4b). Cross sections of the 3D scan in different orientations relative to the substrate reveal a large number of damaged cells in this peripheral layer (Figure 4.5), as also observed by Bohn et al [24]. Examples of such locations are marked by stars (∗) in Figure 4.5.
In both pictures, the inner tissue (**L**) is located at the center of both pad main body and branchlet. This tissue exhibits an ordered cell structure with elongated, compactly stacked cells, with a low concentration of macroscopic defects (Figure 4.5). As it correlates well with the central compact lignified tissue described in [24], this tissue is assumed to be lignified.
A segmentation of this central lignified tissue in the pad µ-CT scan is shown in two different orientations in Figure 4.6. The substrate is not visible but is located as usual in the negative z positions and the branchlet is oriented along the x-axis. This central tissue resembles an arm and an "open hand with fingers" [134]. To stay with this image, the arm is located inside the branchlet; the palm is at the junction between the branchlet and the pad main body, while a dozen of "fingers" are spread out in the pad main body. The fingers are oriented radially around the pad center.

4.2.2 Modulus distribution in the pad

The modulus distributions in the pad cross sections and in the branchlet are compared in Figure 4.7. The modulus values within one cross section vary between 0.2 GPa and 4 GPa, whereas roughly 80 % of the modulus values over all cross sections are distributed between 0.7 GPa and 2.7 GPa. A larger fraction of compliant tissue is found in cross section 3 (CS 3) and of stiffer tissue in CS 6 than in the total of all cross sections.
Figure 4.8 summarizes the deconvolution results of the modulus in the six successive cross sections. In each cross section, two to four normal distributions are necessary to fit the modulus distribution. The mean value of each normal distribution is represented by a circle. The standard deviation of the normal distribution is plotted as an error bar. The weight associated

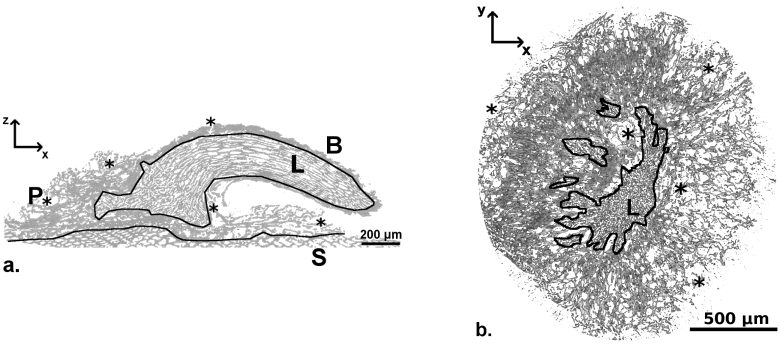

Figure 4.5: Cross sections of one *Passiflora discophora* attachment pad **P** as reconstructed from a µ-CT scan (a) in the plane parallel to the branchlet **B** and perpendicular to the substrate **S** and (b) in the plane parallel to the substrate. The stars (∗) mark locations with bigger cells, which can be understood as defects in pad structure. The lignified central tissue is marked in the pad and the branchlet with a **L**.

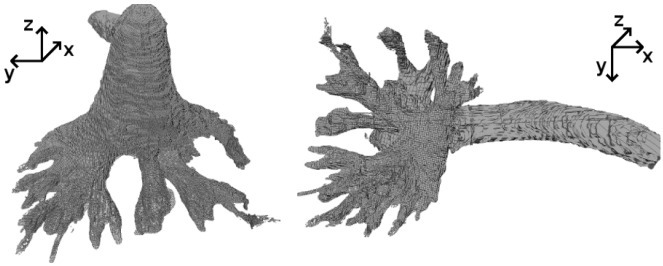

Figure 4.6: Segmentation of a pad central lignified tissue based on a µ-CT scan in two different orientations. The x-axis indicates the branchlet main orientation and the z-axis is normal to the substrate.

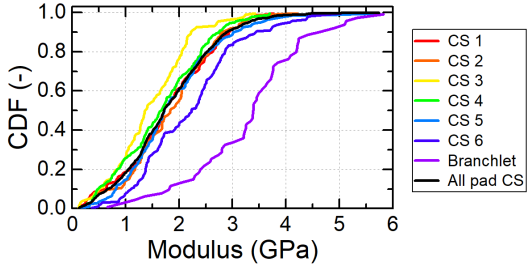

Figure 4.7: Empirical modulus distribution in each cross section of the pad, in the branchlet cross section and in all pad cross sections (branchlet excluded).

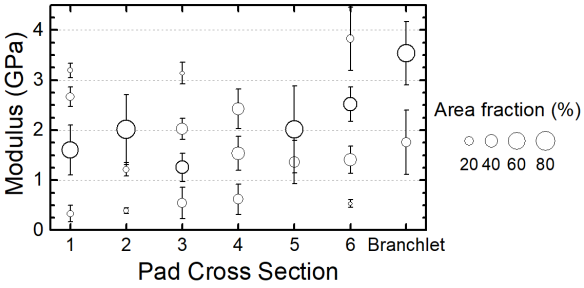

Figure 4.8: Modulus phase in six pad cross sections and the branchlet. The point center of each phase is located at the phase mean modulus value, the error bars indicate the modulus standard deviation in the phase and the point area is proportional to the phase area fraction in the cross section, as indicated in the legend.

to this distribution in the whole fitting function is proportional to the circle diameter. Each normal distribution is assumed to describe a cross-sectional phase, which mean modulus m_i is the mean value, its standard deviation s_i the normal standard deviation, and the area fraction f_i is associated to the weight of the normal distribution. Most modulus values are found in a range of between 1 GPa and 3 GPa, see the largest circles on Figure 4.8.

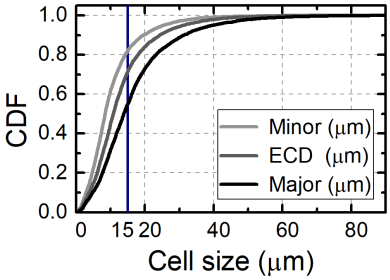

Figure 4.9: Cell ECD, minor and major cell lengths in the pad x-y cross section of Figure 4.10a as explained in section 4.1.2. The punch tip diameter is indicated by the vertical line (15 µm). A few cell major lengths were larger than 90 µm, but were not plotted here for better readability.

4.2.3 Modulus distribution in the branchlet

The branchlet modulus distribution clearly lies at higher modulus values (around 1.5 GPa) compared to those of the pad cross sections (Figure 4.7). The deconvolution of the modulus distribution in the branchlet is presented in Figure 4.8.

Only two phases are sufficient to describe the modulus distribution in the branchlet. The phase with the lowest area fraction in the branchlet also possesses the lowest mean modulus (around 1.8 GPa). This modulus is similar to the modulus of the phase with the highest area fraction in CS 1, for example. The phase with the highest area fraction in the branchlet has the highest mean modulus, around 3.5 GPa. This phase is also present in CS 1, 3 and 6, but with smaller phase fractions.

4.3 Discussion

4.3.1 Role of cell size on nanoindentation experiments

As for all heterogeneous materials, the elastic properties measured via nanoindentation are sensitive to the composition and the distribution of the ma-

terial(s) underneath the indenter. In the case of biological materials, the cell size, as well as the wall thickness and stiffness are important microstructural parameters. The focus of this study, however, is on the properties of the pad tissues rather than of single cells. Thus, an important experimental parameter was the tip diameter that had to be large enough to capture multiple cell walls for each indent, and small enough to capture the tissue's properties.

Figure 4.9 represents the minor (smallest cell dimension), major (longest cell dimension) and the ECD of the cells measured in the x-y cross section of Figure 4.10b. The tip diameter of the conical flat punch used in nanoindentation is marked with a vertical line at 15 µm. The ECD distribution ranges from 0 to over 80 µm, and some cells have a larger diameter than the tip used in the measurements.

However, since the median cell diameter lies around 10 µm, i.e. well below the punch diameter, the tip is appropriate to test a large majority of the cells. Also, considering the minor cell size on Figure 4.9, over 80 % of the cells have their smallest diameter being smaller than the tip diameter. This means that a tip indenting at a random location has an 80 % chance to hit at least one cell wall.

Moreover, comparing Figure 4.10b and Figure 4.5b, the largest cells are mostly located at defect-rich areas, like the ones marked by stars on Figure 4.5. Although the indents locations were randomly positioned over the pad cross sections, defect-rich areas, and with them the largest cells, have been avoided. A negative consequence of this restriction in the indents location might be the underestimation of the fraction of the most compliant pad tissue(s).

Finally, with an indent diameter of 15 µm and an indentation depth smaller than 10 µm, the indentation volume per indent is of the order of magnitude of 1×10^4 µm^3. This corresponds to an actual size of roughly 27 µm being solicited for the measurement of the elastic properties below the indent. The characteristic sizes of the central and peripheral pad tissues are many times larger, on the order of 100 µm (Figure 5D in [24]).

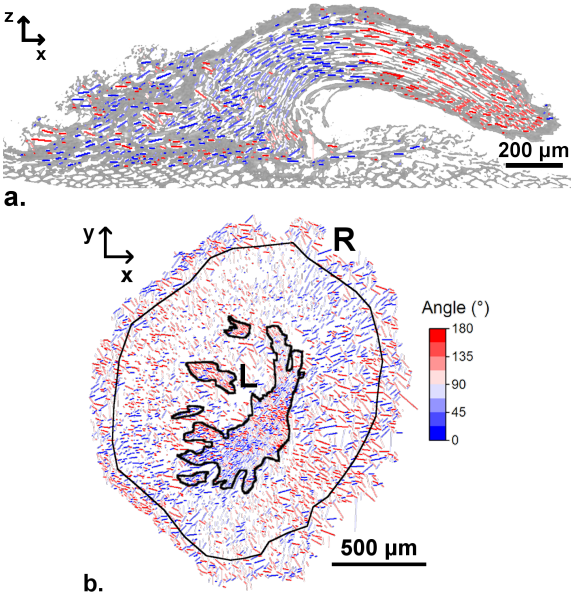

Figure 4.10: Cell location, cell area and cell angle in two pad cross sections with different orientations: (a) parallel to the branchlet and perpendicular to the substrate and (b) parallel to the substrate. The cross sections are the same as those presented in Figure 4.5. The cell center of mass is at the circle center, the circle area is proportional to the cell area and the circle color is the angle of the cell main axis towards the x-axis, in degrees, scaled as in the color scale on the side. The outer black line in (b) indicates the limit between the outer cell layers (R), which present a more scattered organization, and the inner cells. The inner lignified tissue is marked with L.

Thus, the chosen tip diameter, combined with the large indentation depths, enables the measurement of the mechanical properties of the cellular structure(s) in the investigated attachment pad. Hence, the phases determined from the statistical analysis can be associated with regions in the pad having homogeneous modulus.

4.3.2 The pad heterogeneous microstructure

The cells in the *P. discophora* pads have various size and orientations depending on their locations in the pad or in the branchlet.

Figure 4.10 presents the cell location, area and angle in the cross sections of Figure 4.5 measured as explained in section 4.1.2. In both cross sections, the middle of each line is located at the cell center of mass, its length is proportional to the ECD and the line color highlights its orientation between 0° and 180° of the cell longest axis towards the x-axis, following the angle scale. This assumes that the cells have no direction in their longitudinal axis, i.e. that the 0° and 180° orientations are equal.

The cell orientation in the branchlet lignified tissue follows the branchlet geometry at the cell location (Figure 4.10a). For example, at the point with highest z-coordinates in the branchlet, the cells are directed along the x-axis, which is also the branchlet orientation at this location. Similarly, at the junction region of the lignified tissue of the branchlet with the pad lignified tissue ("palm"), the lignified tissue has an angle of around 45° with the x-axis; at this location, the cells also have an angle around 45°, as indicated by their light blue color.

The organization of the cells in a cross section parallel to the substrate is highlighted on Figure 4.10b. The black contours indicate the limit between the outer cell layers (R), which present a more scattered organization, and the inner cells on the inner side of the contours. At the center of the pad main body, the lignified tissue (L) consists of small, densely packed cells with no uniform orientation. The unlignified inner tissue around this lignified central tissue is made of cells with more variable area and a radial orientation. For example, at position of higher x coordinates, i.e. under the branchlet, the cells are mostly painted in dark blue or dark red; they are nearly aligned with the x-axis. Similarly, the cells at the highest and lowest y coordinates are mostly painted in light blue or light red; they are nearly aligned with the y-axis.

Regarding the pad microstructure, two tissues with large area fractions are visible on light microscopy pictures (Figure 4.3), on µ-CT scans (Figure 4.5), and on Figure 5D in [24]. The inner one is made of lignified cells, which have rather small cross sections in the pad and which are continuously present from the pad up into the branchlet (Figure 4.6). The outer tissue is radially organized, and possesses a higher distribution of cell cross sections diameter and of damaged cells. A small layer of more damaged, compliant cells at the pad surface seems to protect the pad core (Figure 4.10b).
Bohn et al. [24] also concluded that the pads consist of a "lignified and thus stiff central tissue", surrounded by two tissues, the "parenchyma and pad tissue[s]". Both last tissues were described as "less stiff" than the central tissue. In this study, these two tissues could not be distinguished.

4.3.3 Heterogeneous distribution of elastic properties

The phases from Figure 4.8 were grouped into four mechanically different structural areas (Figure 4.11). These areas were defined such that, in priority order:

- each phase in one cross section must fit into a single structural area,
- a structural area cannot contain two phases of the same cross section,
- within the previous constraints, the width of the structural area must also contain each phase's standard deviation.

As discussed above, one structural area represents a pad zone with homogeneous elastic modulus. The number of four areas is the smallest possible number of regions that can be defined in this way, as e.g., the sixth cross section possesses four phases. Like the phases, also the structural areas can overlap. Table B.9 in Appendix B summarizes the modulus range and the mean value of each structural area.
The structural area 1 is found only in small proportions in the cross sections and not at all in the branchlet. The embedding material could influence

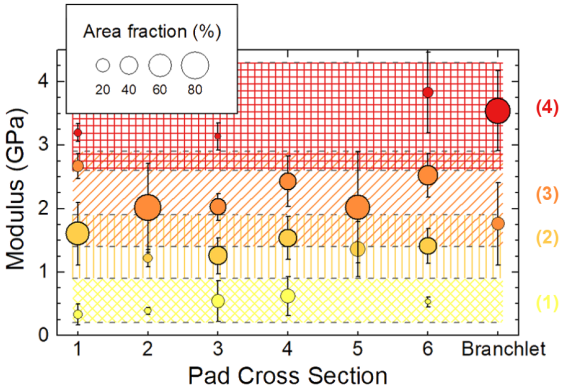

Figure 4.11: Four structural areas as determined from the modulus phases in six pad cross sections and the branchlet.

the measured mechanical properties, in particular at the most peripheral locations in the cross sections. Indeed, Young's modulus of the embedding material, i.e. paraffin wax, is in the range of 0.23 GPa [135]. Furthermore, the elastic modulus of parenchyma tissues is typically between 0.3 MPa and 14 MPa [136]. Since the branchlet is also embedded in wax, and contains no phase in the first structural area, it is unlikely that only the wax properties were measured in this structural area. Elongated unlignified cells were observed in the peripheral regions of pad cross sections [24], which are expected to have a lower stiffness. Also, this peripheral tissue shows degradation through senescence or tissue shrinking during drying (marked by $*$ in Figures 4.5a and 4.5b), which would result in reduced stiffness. Thus, the first structural area could be influenced most by the unlignified peripheral cells.

The structural area 4 is mainly present in the branchlet, where it represents the largest phase fraction. The structural areas 2 and 3 are the most important one in proportion and are present in almost constant fractions in all cross

sections. The overlap of the areas 2 and 3 as well as 3 and 4 might be related to a mechanical interaction of neighboring structural zones.

The structural areas 2 to 4 are much stiffer than the first structural area, and are thus related to the presence of the stiffer lignified tissue in the pad core [24]. The presence of three phases for a full description of this tissue's mechanical properties is explained by the stronger tissue anisotropy than in the peripheral tissue. Indeed, first the cell structure mechanical properties are probably anisotropic, due to both the cell morphology and the material anisotropy, like in a certain number of plant cells [136]. Wood for example is known to show orthotropic mechanical properties [18, 136] and to possess lignified, honeycomb-like, load-bearing cells [136]. The walls of lignified wood cell also exhibit orthotropic mechanical properties, due to the anisotropy of the cell wall layers: " the mechanical properties of the cell wall in the longitudinal direction largely depend on those of the S2 layer", whereas "the S1 layer contributes significantly [to the transverse modulus]" [136]. Thus, comparing the lignified cells of the attachment pad with the lignified wood cells, which have similar morphology (large aspect ratio) and function (load-bearing), one could expect the pad cells to show orthotropic mechanical properties.

In the nanoindentation measurements, the pad structure was tested only perpendicular to the branchlet (Fig. 4.3). However, the orientation of the cells in the inner tissue varies continuously from 0° (aligned with the branchlet) to 90° (perpendicular to the substrate), see Figure 4.5. The branchlet lignified cells were tested along their longest axis, while the lignified cells in the pad center where tested fully along their transverse orientation, across the grains. Considering the continuous variation of orientation of the lignified cells, the lignified inner tissue was tested in all orientations.

Thus, the structural area 4 can be understood as the elastic response of the lignified tissue tested parallel to the cell main axis, i.e. the stiffest direction of the tissue. This is corroborated by the fact that the inner branchlet cells in the investigated cross section are aligned parallel to the indentation direction

(see Figure 4.3g). The structural areas 2 and 3 also represent the elastic response of the same tissue but were tested with a middle angle related to the branchlet (area 3, angle around $\pm 45°$) or high angle towards the branchlet orientation (area 2, near $\pm 90°$).

4.3.4 Role of the heterogeneity on the attachment

Based on the microscopic investigations and the definition of the pad structural areas from nanoindentation, a two-dimensional pad model was proposed (Figure 4.12) [134] to investigate the linear-elastic stress distribution within the pad and at the pad-substrate interface. Five zones were distinguished, and associated with isotropic, linear-elastic properties. The zone properties (Table 4.1) were defined as the mean value of the elastic modulus of each structural area (Section 4.3.3) and the substrate.

The zone A (Fig. 4.12) simulates the compliant, unlignified tissue found at the pad periphery. Thus, the mean modulus of the most compliant structural area was attributed to this zone. The zone D simulates the lignified tissue in the branchlet. The cells are elongated and aligned along the tissue path, as in the branchlet cross section that has been tested during nanoindentation experiments. Thus, the mean modulus of the stiffest structural area was attributed to the zone D. The geometry of zone B simplifies the path of two "fingers" of the central lignified tissue (Figure 4.6), and zone C is the intermediary zone between the zones B and D. For the substrate, a modulus of 10 GPa, typical of wood [18], was assumed. A Poisson's ratio of 0.3 was chosen for all phases, which is typical value for polymers [137] and wood [18].

In the FE analysis (conducted by Dr. R. Kappel, IAM-WBM, KIT, Karlsruhe, Germany [134]), a force F of 10 N is applied horizontally on the branchlet cross section (Fig. 4.12), simulating the tensile force of the plant stem on the pad. The substrate is fixed in all directions at its side opposite

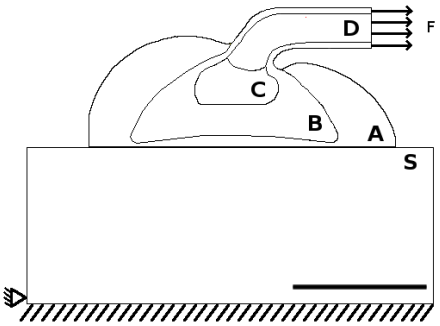

Figure 4.12: Attachment pad model for the simulation of linear-elastic stress distribution at the pad-substrate interface. Four regions are marked from A to D, the substrate is marked with S and the force applied on the branchlet with F. The scale bar is 1 mm.

Table 4.1: Elastic properties associated to the zones in the pad model.

Pad model zone	Young's modulus (GPa)	Poisson's ratio
A	0.5	0.3
B	1.4	0.3
C	2.1	0.3
D	3.4	0.3
S	10	0.3

to the pad and also laterally at the farthest substrate edge opposite to the branchlet.

The von Mises equivalent stress is influenced by the geometry of the zones. As can be seen in Figure 4.13a, the highest von Mises stress in the pad is reached where the branchlet bends into the pad. The stress extrema near the pad surface (dashed lines) are local extrema resulting from singularities caused by the sharp edges of the pad model. They are not considered in the following. Opposite the branchlet (negative positions along the interface, see Figure 4.13b), tensile normal stresses occur, which may cause the pad to peel off. Underneath the branchlet (positive positions along the interface),

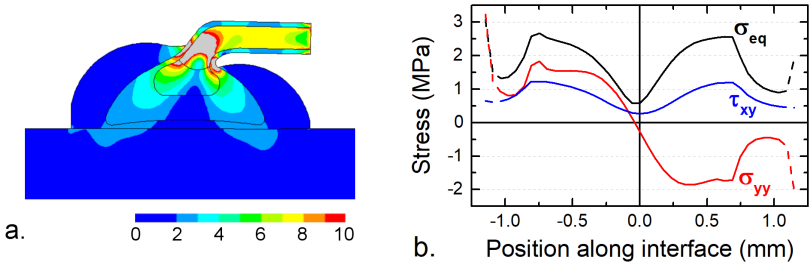

Figure 4.13: a) Von Mises stress distribution in the 2D model of the attachment pad under horizontal loading, using a Finite-Element Analysis. The stress is limited to a range between 0 MPa and 10 MPa. The grey zones are stressed over 10 MPa. b) Stress distribution at the pad-substrate interface: shear stresses τ_{xy} parallel to the substrate, normal stresses σ_{xx} perpendicular to the substrate and von Mises stresses σ_{eq} are shown. The stress extrema (dashed lines) at the interface borders result from singularities caused by the sharp edges of the pad model. The pad is stressed in tension on the side opposite to the branchlet (negative positions) and in compression underneath the branchlet (positive positions). Both normal and shear stresses present high variations over the interface.

the normal stresses are compressive, which helps to stabilize the pad. The maximum of all stresses is at the same location, more than 0.2 mm away from the edge, and thus clearly inside the pad. The location of the tensile stress maximum at the pad-substrate interface seems to be related to the model inner geometry (zone B in Figure 4.12).

A FE parameter study varying the mechanical properties of the different zones reveals the role of the central stiff pad interior part (zones B to D), which concentrate the higher stress in the pad and at the interface [134]. The parameter study also corroborates the importance of the peripheral tissue (zone A) for the attachment; it protects the pad and acts as the counterpart to the stiff central tissue preventing failure due to peeling off at the pad edges.

4.4 Summary

The microstructure investigations with light microscopy and micro computed tomography, as well as the SNT analysis of many cross sections, confirmed

the heterogeneous structure of the *P. discophora* attachment pads. Four elastic phases were defined as results of a statistical analysis of the pad's elastic properties. Young's modulus of these areas varied between 0.5 GPa and 3.4 GPa. The softest areas are found in the outer cell layers of the pad, while the stiffest areas are located in the center of the pad. The branchlet is almost exclusively made of stiff, lignified tissue. The elastic phases were used as input for an elastic model of the pad. In a parameter study based on an FE analysis, it was shown that the pad internal structure improves its attachment on a substrate. This is achieved by moving away the maximum of the internal stresses from the pad edge inside the pad.

5 Nanoindentation of mortar

Cement-reinforced polymeric materials are sometimes called mortar. They are used as glue between a steel rod and concrete, for example. Their heterogeneous microstructure is due to the cementitious phases in the material. The addition of a polymeric phase to cement increases the mortar tensile stiffness and its long-term properties.
In the following, the mechanical properties of individual material phases are investigated by nanoindentation and a statistical analysis, and in particular the phases' evolution over the sample age under various static loads. The properties of the phases can be used as material parameters for modeling of the material aging.

5.1 Experimental details

5.1.1 Material description and sample preparation

The mortar FIS EM 390S from fischer (fischerwerke GmbH, Waldachtal, Germany) was investigated. The mortar is an epoxy-based polymer filled with Portland cement paste in a proportion of 25 % to 50 %. The two monomer reactants and the cement powder are mixed using a fischer static mixer FIS UMR and a fischer dispenser FIS AM.
One sample was poured on a microscope glass slide, which was itself glued on an aluminum sample holder. The top surface was covered with a smooth plastic foil and a glass slide, placed on two cylinders of 2 mm diameter on opposite sides of the sample. This aimed to reduce the roughness of the upper sample's surface for nanoindentation and improve its parallelism with

the lower surface. The final sample dimensions are $20 \times 15 \times 2\,\mathrm{mm}^3$. After the first initial curing period of 24 hours, the upper slides were removed and the sample was stored in an air-conditioned room until the end of the curing reaction to prevent large temperature changes to influence the reaction.
Three samples were poured into self-made molds of silicone (Silcolan NV, Creartec trend-design GmbH, Lindenberg, Germany). To avoid damaging the mortar surface used in nanoindentation through the sample preparation, which would influence the measurement of the mechanical properties, the sample preparation had to ensure a smooth surface of the samples. Therefore, a PVC dummy of the right dimensions was cut and one side of its surface was either polished or prepared in contact with a clean glass surface, so that it had a face with a low roughness.The silicone mold was then poured around the dummy, and the dummy removed after full curing of the mold. The dummy smooth surface was thus copied in negative in the silicone mold. Then, the mortar is poured into the silicone mold, which is put within the first 20 minutes into a vacuum bell for five minutes to remove large air bubbles from the sample core. For the rest of the curing, all samples were kept in an air-conditioned environment until the last nanoindentation experiments were done.
The optical microscope was used for visual control of surface quality prior to mechanical testing and imaging the microstructure, and the confocal laser microscope was used to capture three-dimensional reconstructions of the surfaces, which enabled the calculation of the R_q roughness. Additionally, a µ -CT scan on a piece of mortar FIS EM of $1 \times 1 \times 1\,\mathrm{mm}^3$ with a resolution of 0.7 µm/pixel (Figure 5.1) was done to further investigate the mortar microstructure (scan and reconstruction by RJL Micro & Analytic GmbH, Karlsdorf-Neuthard, Germany). After 3D reconstruction from the slices, the microstructure of the sample was investigated in a subvolume of 490 µm side length of the investigated sample. The subvolume did not contain any surfaces of the sample to limit the influence of potential preparation artifacts on the microstructure investigation. Two material phases (particles and matrix)

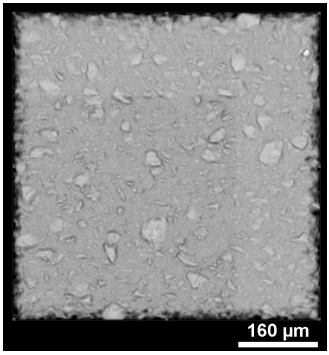

Figure 5.1: Cross section of a reconstructed mortar subvolume from a µ-CT scan with a resolution of 0.7 µm/voxel. The whiter the voxels, the denser the material or the higher the atomic number.

and a porous phase were segmented based on the grey values of the pixels: pores possess the darkest pixels, the particles the brightest pixels, and the pixels in-between are associated with the matrix. The phases were segmented based on the two minima of the grey values distribution. Then, the center of mass and the ECD of each segmented particle or pore within the subvolume, but also the mean ECD, the total surface and the volume ratios of both the porous and the particle phases were calculated.

5.1.2 Nanoindentation methods

Influence of aging on mechanical properties

The mortar FIS EM sample was tested 14 times over a period of 35 weeks, in order to observe the evolution of its mechanical properties with time, i.e. the chemical and physical aging of the material. The first test was done as soon as mechanically possible, i.e. after around 44 hours, and the last one after 247 days, i.e. 35 weeks. In agreement to the method proposed by Sebastiani et al [138], the high-speed option of the nanoindenter was used to capture the material heterogeneity with a statistically sufficient number

of indents in a relatively short time. 7 to 8 fields of 26×26 indents were programmed for a total test duration of around 8 h. The distance between two neighboring indents was set to 20 µm. The nominal indentation depth was 1 µm and indents with an indentation depth smaller than 600 nm or larger than 2 µm were filtered out before the analysis. This filter of the indents over the maximum depth aimed to improve the consistency of the distribution of the investigated properties at the nominal depth, while considering as much experimental data points as possible in the further analysis.
The final number of valid indents per run was between 3533 and 5387, with an average of 4682 indents. The total surface covered by the indent fields is $7 \times 500 \times 500\,\mu m^2$ to $8 \times 500 \times 500\,\mu m^2$ per run, or $1.75\,mm^2$ to $2\,mm^2$, including the invalid indents.
A Berkovich tip was used, and calibrated using a reference quartz sample. The frame stiffness was calibrated on the same sample. Both the hardness and the elastic modulus distributions were investigated. The analysis constants ε and β were set to 0.75 and 1.05, respectively (see Section 2.2.1). The Poisson's ratio ν of all phases is unknown and was thus assumed to be 0 for the calculation of the elastic modulus in the nanoindentation analysis. The Young's modulus assuming a Poisson's ratio ν_{as} can be obtained dividing the modulus presented in this study by $1 - \nu_{as}$.

Influence of aging under external loading on mechanical properties

To investigate the material under realistic aging conditions, three samples were kept under a static load over a few months and their microstructure was investigated with nanoindentation. One of the samples was loaded under compression, the second one under tension and the third one under shear. Specialized set-ups (Figure 5.2) were developed to apply the load on the sample, and also during the nanoindentation testing. A load sensor (Metron PT4000, Metron Messtechnik und Maschinenbau GmbH, Essen, Germany) was also integrated in all set-ups. The signal of the load sensors was read

with a digital microprocessor controlled display unit with integrated signal amplifier (Metron MMV22), as pictured on the left side of Figure 5.2b.
Table 5.1 summarizes the sample dimensions, applied load, applied stress on each sample for all long-term loading experiments. In the compression and tension experiments, the applied stress was between 38 % and 68 % of the corresponding short-term failure stress of the materials and registered regularly to account for relaxation of the sample and the load frame. The high load applied in the shear experiment compare to the other experiments aimed to generate high deformations in the sample. The actually applied shear stress and the reference shear strength of the material could not be estimated.
A high relaxation effect was observed after the load application. For example, a mean load drop of -270 N, i.e. -5.6 %, was observed during the first two hours for the sample under compression. Thus the load applied was adjusted twice a day during the first week and once a day in the second week in order to keep the stress on sample as constant as possible. After the third week, the relaxation slowed down and the load on sample was adjusted every two to four days.
As for the mortar without load, 6 fields of 26×26 indents were programmed for each run, i.e. a maximum of 4056 indents per day. All other parameters of the indentation were kept similar to the aging experiments without axial loading. 3836 ± 128, 4045 ± 5 and 4029 ± 39 indents were successfully done per run on the compression, tension and shear samples, respectively.
In order to investigate the macroscopic deformation of the sample under the constant axial loading, 10 to 12 markers were put on the top free surface close to the sample edges.
The markers' coordinates (X_m, Y_m) at every measurement day T are measured with optical microscopy and used to calculate the uniaxial strain $e_{x,m}$ in the compression and tension samples and the shear strain $\gamma_{xy,m}$ in the shear sample.

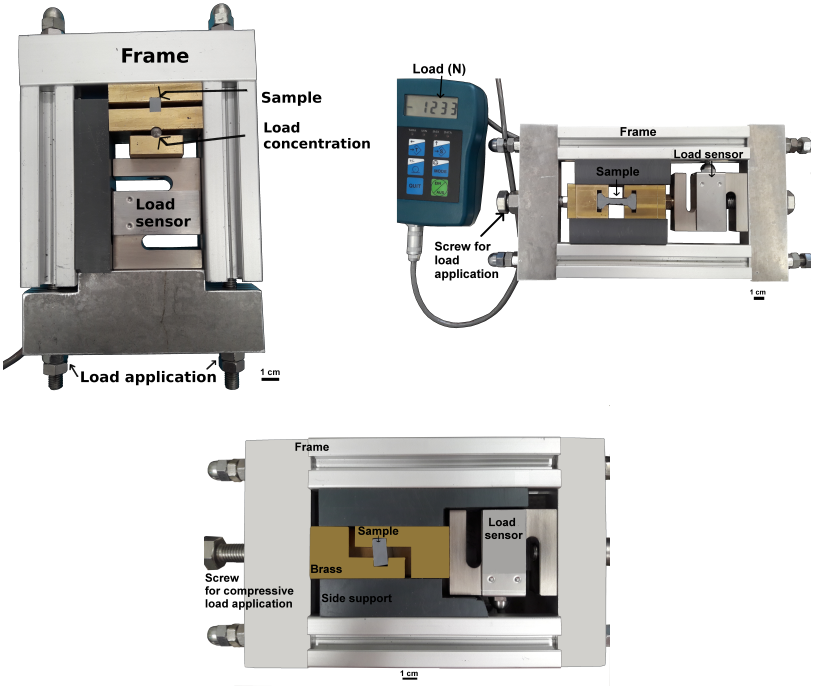

Figure 5.2: Investigation set-ups for static loading of nanoindentation samples in (a) compression, (b) tension and (c) shear. The applied load can be corrected on each set-up after measurement of the current load with the load sensors and the digital microprocessor.

5.1.3 Statistical analysis

The LM procedure (see Section A.1.1) was used to investigate the aging of the mortar with and without static load. Both modulus and hardness were analyzed. Fitting functions with three to four phases were used for all loading conditions and at each age to fit the modulus distribution. For the hardness distribution, one phase was assumed, as only replicable number of phases over all samples. Additionally, the EM procedure (see Section A.1.4) was also used to investigate the aging of the mortar without load, to further inves-

Table 5.1: Experimental parameters for mortar long-term loading experiments: dimensions of the sample (free surface and heigth), applied load on the sample, corresponding stress applied on the sample and reference short-term failure stress, as well as maximal load enabled by the sensor. Reference failure stress and actual applied stress could not be estimated for the shear experiments.

Sample		Compression	Tension		Shear
Sample age range		1 - 28 d	1 - 51 d	51 - 66 d	1 - 42 d
Test parameter	unit				
Dimensions of free surface	(mm^3)	$6 \times 4 \times 30$	$4 \times 12 \times 30$		$6 \times 8 \times 30$
Applied load	(N)	4905	818	1600	2000
Applied stress	(MPa)	27.25	6.81	13.3	-
Ref. short-term fail. stress	(MPa)	72	18		-
Applied stress	(% of reference)	38	38	63	-
Sensor maximal load	(N)	5000	2000		2000

tigate the number of phases in the modulus distribution. One to five phases were used to fit the modulus distribution at each age with this second fitting procedure.

5.2 Results

5.2.1 Microstructure and surface roughness

Surface roughness

The surface of the mortar samples exhibited good quality for nanoindentation (Figures 5.3a and 5.3b), as only a few particles, thin scratches and small bubbles are visible on the surface with the optical microscope. The sample roughness R_q was around 0.47 µm and 0.33 µm over an area of $530 \times 700\,\mu m^2$ and $200 \times 400\,\mu m^2$, respectively. For all samples, the indentation depth of 1 µm is at least twice as high as the mean sample roughness R_q over a large area. But the sample's roughness decreases with decreasing area and is 0.05 µm to 0.2 µm over an area of a few micrometer. At this size, the indentation depth is larger than five times the surface roughness, which might be sufficient to estimate accurately the material mechanical properties [99].

Microstructure

13159 particles were segmented from the 3D reconstruction of a mortar cube; they have an ECD of 6.4 ± 4.9 µm (see Figure 5.3c). The volume fraction of the particles was 1.4 %. The ECD of the 125259 segmented pores was 2.6 ± 1.9 µm for a volume fraction of 0.84 % (see Figure 5.3d).
The phase separation condition in the statistical nanoindentation technique (SNT) requires that the indentation depth is much larger than the characteristic size of the phase to be characterized, i.e. $h > 10D$ (see Section 2.2.5). With an indentation depth of 1 µm, the particles may be characterized as a single mechanical phase as their ECD is six times larger than the indentation depth. However, due to the small volume fraction, a large number

of indents would be required to enable the mechanical characterization of these particles. As the pores only have an ECD two times larger than the indentation depth and an even smaller volume fraction within the material, they cannot be characterized as a single phase. Thus, the chosen indentation depth represents a good compromise between the surface roughness and the deconvolution of the mechanical properties of the particles as a single phase.

5.2.2 Load relaxation

The absolute values of the load relaxation of the samples and the nanoindentation setups decreased over time (Figures 5.4a, 5.5a and 5.6a). In all samples, the maximal load relaxation is measured on the two days following the load application (days 2 and 3), and reaches 3.1 %, 4.8 % and 1.2 % per hour in average in the compression, tension and shear setups, respectively.
But from the days 17, 20 and 22 on, the absolute value of the load relaxation is less than 0.01 %, 0.12 % and 0.03 % per hour in the compression, tension and shear setups, respectively, indicating a rather constant external load application on the sample.
This indicates that the largest part of the samples and setups relaxation happens within the first 20 days of the experiments. Afterwards, a small, but constant relaxation is observed.

5.2.3 Strain estimations

The applied external load aimed at inducing an exclusive compression, tensile or shear deformation of the investigated samples. Estimating the strains in the sample provides a check on the actual samples deformation.
The uniaxial engineering strain in the compression sample increases with the sample age (Figure 5.4b). However, the sample sheared or rotated over the experiment duration: for example at day 20, -1.2 % maximal compression strain were measured on the one side of the sample top surface (Marker 1), compared to -0.5 % on the other side (Marker 2). Over all markers located

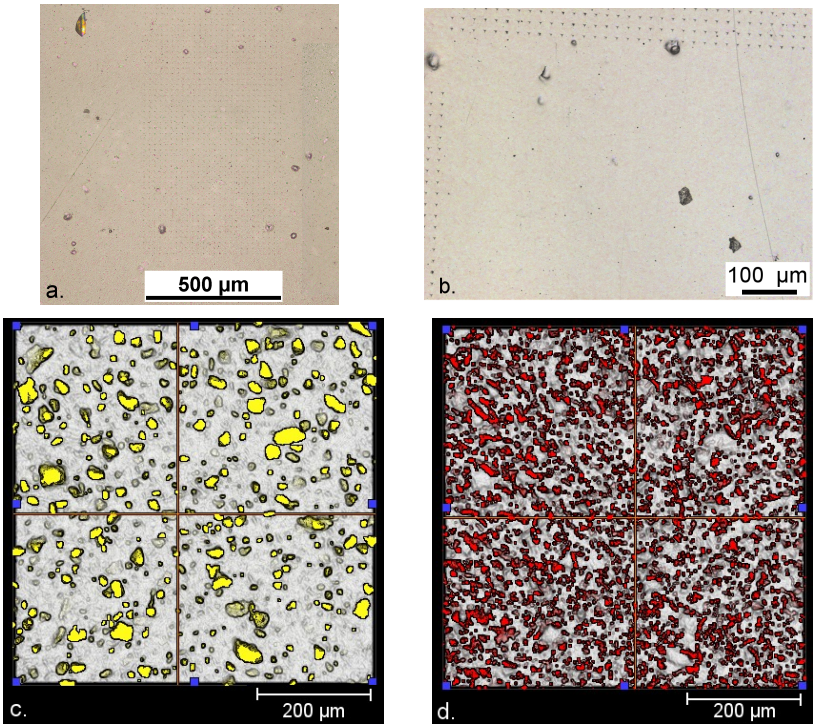

Figure 5.3: Surface of two mortar samples used for aging investigations and 3D segmentation of particles and pores within a mortar sample investigated with µ-CT. (a) Surface of mortar aging sample without load after nanoindentation investigations, optical microscope. Some indent fields are visible on the surface. (b) Surface of mortar aging sample under tensile load after nanoindentation investigations, confocal laser microscope. Some indent fields are visible on the top and the left of the picture. (c) Segmentation of 13159 particles in a 3D reconstruction of mortar from a µ-CT scan. (d) Segmentation of 125259 pores in a 3D reconstruction of mortar from a µ-CT scan.

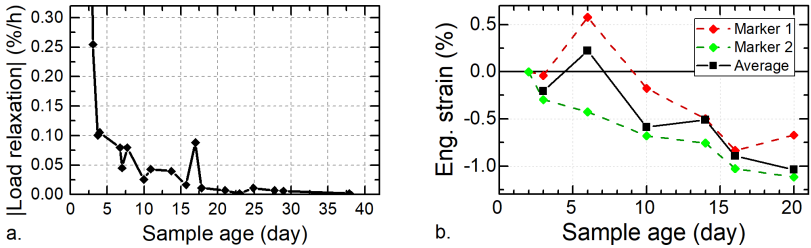

Figure 5.4: (a) Absolute value of the load relaxation in set-up and sample under compression, where the highest values are not shown for better visibility, and (b) uniaxial engineering strain over sample age at two markers location opposite to the fixed side of the sample (Markers 1 and 2) and averaged over all markers.

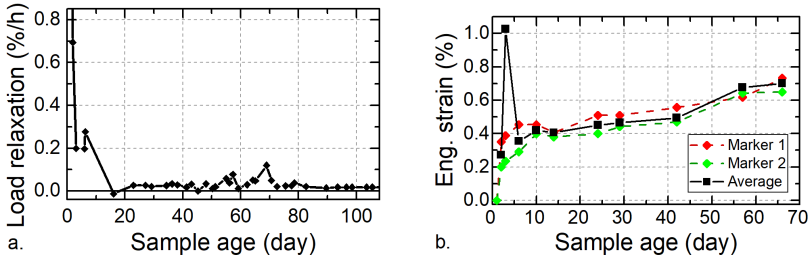

Figure 5.5: (a) Load relaxation in set-up and sample under tension and (b) uniaxial engineering strain over sample age at two markers location opposite to the fixed side of the sample (Markers 1 and 2) and averaged over all markers.

at the farthest from the fixed part of the sample, a mean compression strain slightly higher than 1.0 % was found at day 20.

The uniaxial engineering strain in the tension sample increases with the sample age (Figure 5.5b), in particular in the first ten days after the load application. A second increase of the strain happens shortly after day 51, when the external load is doubled. The deformation is homogeneous on both sides of the samples (compare Marker 1 and Marker 2) and nearly linear after day 6. The mean tensile strain at the farthest marker from the fixed side of the sample is less high than in the compression sample, in particular after day 14.

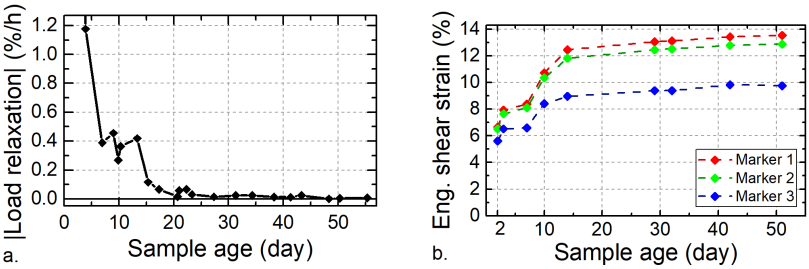

Figure 5.6: (a) Absolute value of the load relaxation in set-up and sample under shear, where the highest values are not shown for better visibility, and (b) macroscopic shear strain over sample age for three markers. Marker 1 is located the nearest to the moving sample side whereas Marker 3 is located near the clamped sample side and Marker 2 in-between.

The engineering strain in the sheared sample increases with the sample age (Figure 5.6b). The shear deformation is larger on the 'free' side of the sample (Marker 1) than near the clamped side (Marker 3). Marker 2 is located between both other markers. For example, the deformation for Marker 1 is higher by 4 % than for Marker 3 after the 14th day. The highest shear deformation increase happens between the 2nd and the 14th days, >85 % (for the investigated markers) of the shear deformation takes place within the first 14 days of the sample. This might give a hint on the speed of the chemical reaction in the sample.

5.2.4 Mortar aging without load

The cumulative distributions of the indentation modulus in FIS EM measured at 1 µm at different ages and without static load are shown in Figure 5.7a. Between the first and the last run, the median elastic modulus has increased by 15.5 % and the whole curve shifted towards higher modulus values. The fastest increase of modulus happened during the first month; the median modulus increased by 13.6 %, which is 88 % of the total increase.

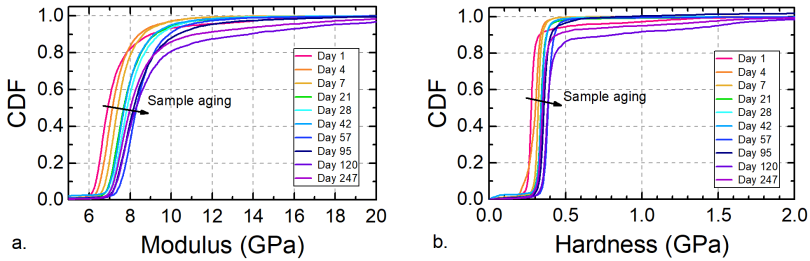

Figure 5.7: (a) Indentation modulus and (b) hardness distribution of mortar at 1 µm depth at ages between 1 day and 9 months (247 days)

The hardness evolution enables characterizing the plastic properties evolution of the sample. Figure 5.7b presents the hardness CDFs over time. As for the modulus, the curves are shifted to higher hardness values over time, in particular during the first month. For example, the median hardness in FIS EM has increased by 24.4 % during the first month, which represents 92 % of the total hardness increase.

5.2.5 Mortar aging under external load

The modulus distributions over age of the different samples are plotted in Figures 5.8a, 5.9a and 5.10a for the compression, tension and shear samples, respectively. For the compression sample, the distribution is shifted towards higher modulus values after the load application, in particular at the very early ages: the distribution median increases from 7.9 GPa on day 1 to 8.14 GPa on day 2. Then, the modulus decreases until day 7, with a median slightly above 8.0 GPa and increases again from day 7 on, and the median reaches 8.27 GPa on day 29.

For the sample under tensile load, the distribution is shifted towards lower modulus values just after the load application, and the distribution median decreases from 8.3 GPa on day 1 to 8 GPa on day 2. Then, the modulus increases until day 28, with a median around 8.3 GPa. After 28 days, the distribution scatters.

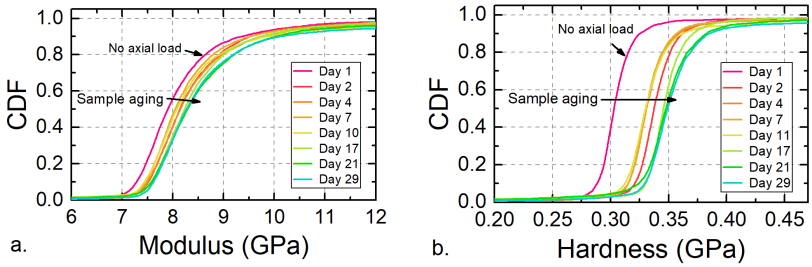

Figure 5.8: (a) Indentation modulus and (b) hardness distributions in mortar under compression over sample age.

For the shear sample, the distribution is shifted towards higher modulus values after the load application, with a median increase from 8.5 GPa on day 1 to 8.7 GPa on day 4. After day 4, the modulus decreases until day 42, for a median decrease from 9.4 GPa to 8.5 GPa. After day 28, a larger proportion of very high modulus indents (>12 GPa) was measured, as well as a larger proportion of low modulus indents (<7.8 GPa).

The hardness distribution over the sample age is plotted in Figure 5.8b. The distribution is shifted towards higher hardness values after the load application, with an increase of the median from 0.305 GPa to 0.335 GPa on days 1 and 2. Then, the hardness decreases until day 11, with a median around 0.330 GPa and increases again from day 11 on, when the median reaches 0.345 GPa.

The hardness distribution over the sample age is plotted in Figure 5.9b. Again, the load application shifts the distribution towards lower hardness values, with the distribution median decreasing from 0.315 GPa on day 1 to 0.31 GPa on day 2. After the second day, the hardness decreases until day 28, with a median around 0.345 GPa, and then scatters around this value.

In the hardness distribution (see Figure 5.10b), the hardness also increases after the load application, with a median increase from 0.32 GPa on day 1 to 0.35 GPa on day 2. Then, the hardness increases further until day 28, with a median around 0.36 GPa, and finally scatters around 0.35 GPa at the

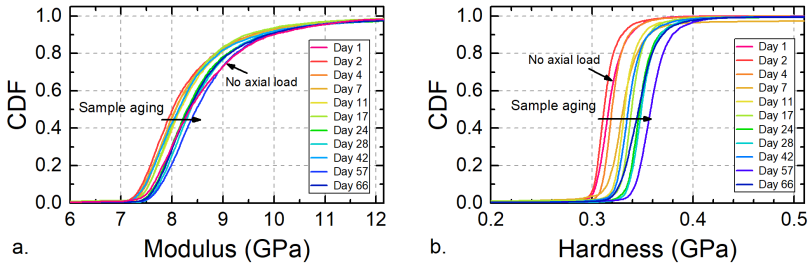

Figure 5.9: (a) Indentation modulus and (b) hardness distributions in mortar under tension over sample age.

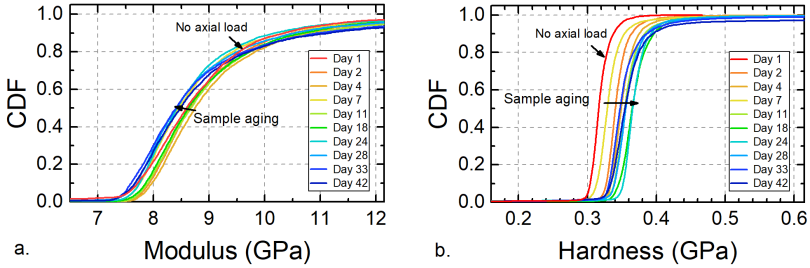

Figure 5.10: (a) Indentation modulus and (b) hardness distributions in mortar under shear over sample age.

other days. As for the modulus, a larger proportion of very hard (>0.4 GPa) indents was found at higher ages, in particular after day 33.

5.3 Discussion

The distribution of a mechanical property at various ages in a material provides some insight about its physical-chemical aging. But, for a heterogeneous material, besides the overall distribution, also the aging of the individual mechanical phases in the material provides interesting insights. To determine the aging of individual phases in the mortar, first the most probable number of phases in the material is determined from the analysis of the

elastic modulus distribution. Then, the phase properties (modulus and hardness) under different external loading conditions and their evolution with the sample age are investigated and discussed.

5.3.1 Number of elastic phases in the mortar

In the sample without load on day 1, the lowest BIC (1.09×10^4) is found for a five-phase fit (5.11a). However, the differences between the BIC of the distributions between three and five phases are small: their variation is smaller than 2.4 %. Also, when starting the fitting with a new set of random parameters, 94 % of the fits were successful for a four-phase fit, but only 78 % for a five-phase fit. Thus, to avoid overfitting of the distributions, keep the fitting model as simple as possible (see Section 2.2.6), and take into consideration the decreasing proportion of successful fit replicas with increasing number of phases, a number of phases under five is considered in the following.

Comparing the BICs of the fitting function with between 3 and 5 phases on all measurement days for the sample without load (Figure 5.11b), the BIC was minimal for a four-phase function at age of 4 d, 21 d, 28 d, 95 d and 120 d, and for a five-phase function at the other ages. Also, the largest difference in the BIC of the investigated fits at a given age is smaller than 2.4 %, and is found on day 1. This indicates that all three fitting models have similar goodness-of-fit for this sample, in particular after day 1, and further analysis of the actual phases is necessary to distinguish the best fit among the three-phase, four-phase and five-phase fits.

In the five-phase fits, the phase fraction of the stiffest phase (phase 5) is the smallest of all phases at all measured ages (Table 5.2), with less than 6.2 %. Exceptions are on days 4 and 120, where the smallest phase fraction is associated with the second stiffest phase (phase 4). The mean fraction of phase 5 at all measured ages is 3.44 % and only 2.22 % when days 4 and 120 are not considered, corresponding to a low number of investigated locations, around 100 to 200.

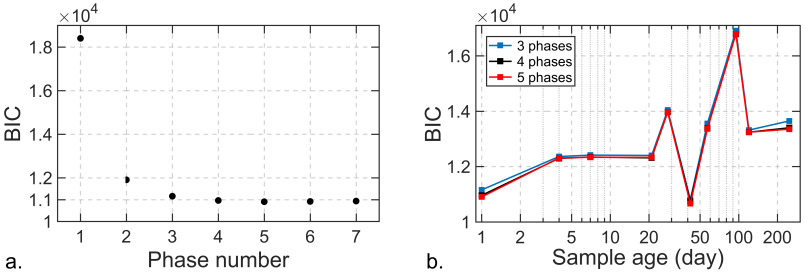

Figure 5.11: BICs of fitting functions with various numbers of phases in mortar without load (a) on day 1 and (b) their evolution with sample age.

Table 5.2: Phase fractions of the stiffest (phase 5) and second stiffest phase (phase 4) in the five-phase fit of the mortar modulus distribution without long-term loading and at different ages. The phase fractions of the stiffest phase (phase 4) of the four-phase fits are also shown for comparison.

	Phase fraction (%)		
	Four-phase fit	Five-phase fit	
Sample age (d)	Phase 4	Phase 4	Phase 5
1	0.19	11.2	0.18
4	4.5	4.3	7.3
7	8.4	13.6	2.0
21	5.4	13.8	5.1
28	4.0	17.7	3.7
42	12.1	14.2	0.14
57	0.29	7.7	0.25
95	6.5	17.2	6.2
120	15.5	9.0	9.3
247	0.34	12.7	0.33

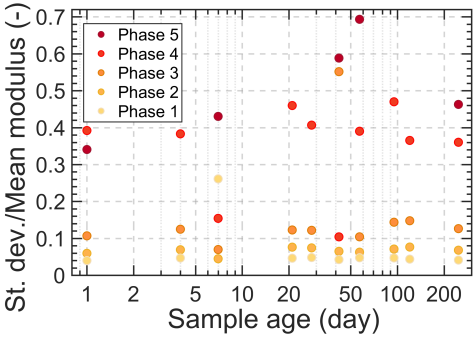

Figure 5.12: Ratio of standard deviation over mean modulus for all phases in the fitting function with lowest BIC as function of the mortar age.

Also, according to Vandamme et al [101], a homogeneous mechanical phase is expected to show a low standard deviation, at least at shallow depths. Thus, the presence of a phase with high standard deviation indicates that many homogeneous phases might interact in the material and might have been gathered into a single phase during the statistical analysis. In this sample, the ratio of standard deviation and mean value of phase 5 is over 30 % on eight out of ten measurement days (Figure 5.12). And at the two remaining ages, either phase 4 (day 47) or the second most compliant phase (day 7) have a standard deviation over mean modulus ratio over 34 % and 25 %, respectively.

Altogether, the low fraction of phase 5, associated to its large standard deviation compared to its mean value and the low differences in the BIC of fits with three to five phases at nearly all investigated days, all of these suggest that this phase 5 of the five-phase fit captures the noise of the stiffest part of the modulus distribution. Thus, a three or four-phase fit would be better indicated to investigate the modulus of the mortar aging.

To proceed with the choice of number of phases, the samples under external load should be considered too. In the absence of BIC calculation with the chosen fitting procedure, the goodness-of-fit r_a^2 criterion of the three-phase

Table 5.3: Mean, minimum and maximum values of the goodness-of-fit criterion r_a^2 of the three-phase modulus distribution in the mortar samples without load and under external load. The sample age (in days) where the minimum and maximum values are reached is also added for comparison.

	r_a^2 goodness-of-fit criterion				
Ext. load	Mean	Min	Age	Max	Age
None	0.999 74	0.999 22	1	0.999 95	57
Compression	0.999 86	0.999 79	29	0.999 96	1
Tension	0.999 85	0.999 78	7	0.999 96	1
Shear	0.999 78	0.999 60	33	0.999 90	1

fit provides good results (see Section 2.2.6) and has been compared for all investigated samples (Table 5.3).
The samples under external load show a better r_a^2 than the sample without load, in particular at day 1, and the three-phase model is considered as valid for the modulus of all samples at all investigated ages.

5.3.2 Elastic properties evolution

Deconvolution

The modulus distributions shown in Figures 5.7a (sample without load), 5.8a (compression sample), 5.9a (tension sample) and 5.10a (shear sample) were fitted with a three-phase model at each measured age.

Mortar sample without load Figure 5.13a presents the empirical distribution of the mortar modulus without load on day 95 fitted with a sum of three weighted Gaussian phases.
The individual Gaussian distributions overlap with each other, but each of them describes a mechanically homogeneous phase with a mean modulus and its standard deviation, as well as a phase fraction in the material equal to

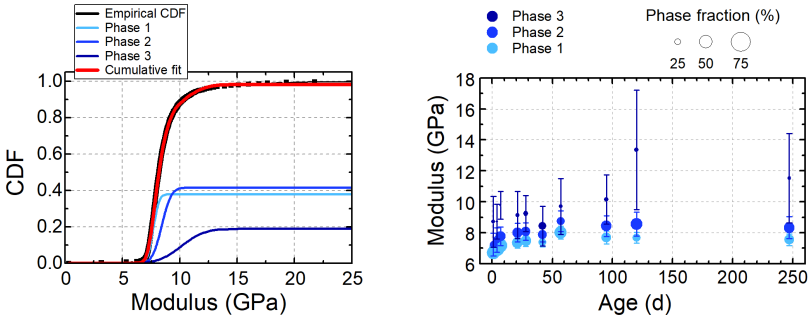

Figure 5.13: Fitting functions of the mortar indentation modulus distribution with three Gaussian functions (a) on day 95 and (b) at ages between 1 day and 9 months (247 days). The circle center represents the phase mean modulus, the error bars its standard deviation, and the circle area is proportional to the phase fraction. In (a), the highest modulus values are not shown for better visibility.

the Gaussian weight. Less than 10 % of all moduli were not represented well by the fitting function, most of them being stiffer than 10 GPa or 12 GPa.

The fitting functions on each day are compared over the mortar age (Figure 5.13b). Each point represents a Gaussian from the fitting function, i.e. a material phase. The circle center is located at the phase mean modulus, the error bars are the standard deviation of the phase modulus, and the circle area increases with the phase fraction.

An increase of the modulus of all phases is observed with increasing sample age, in particular over the first two months (~60 days). After 60 days, the mean modulus of the two most compliant phases is relatively constant with increasing age, whereas the modulus of the stiffest phase increases further (Figure 5.13b). The standard deviations of both most compliant phases show only small variations with the sample age and are smaller than 0.4 GPa and 0.8 GPa, respectively, which corresponds to less than one tenth of the phase mean modulus. The standard deviation of the stiffest phase shows more variation over the sample age and reaches values in the range of 0.9 GPa to 3.9 GPa, with a mean value around 1.8 GPa.

The phase fraction of the most compliant phase decreases from over 50 % before day 7 to less than 40 % after day 95. The phase fraction of the middle stiff phase encountered the opposite variation, increasing from less than 30 % before day 7 to over 40 % after day 95. Despite the high scatter of its mean value, the phase fraction of the stiffest phase does not show a clear increasing or decreasing trend with age, and remains at around 17 %.

Mortar samples under external load Figures 5.14a, 5.15a and 5.16a present the properties of the three phases of the compression, tension and shear samples, respectively, over the sample age, and compared to the phases properties of the sample without load.

In the compression sample, the stiffest phase (phase 3) has a high standard deviation (1.1 to 2.1 GPa). Its fraction is small (10 to 20 %) and decreases after day 4, whereas the fractions of phases 1 and 2 slightly increase from 45 % to 48 % for phase 1 and from 35 % to 40 % for phase 2.

Compared to that of the sample without load, the initial modulus of all three phases on day 1 is higher. Also, each phase of the compressed sample is stiffer than the same phase in the sample without load, and shows a lower modulus increase with age. One of the reasons for this may come from the different sample preparations: the sample without external load was poured on a microscope glass slide, whereas the sample under compression, as well as the other samples under load, were poured into silicone molds (see Section 5.1.1).

In the tension sample, the mean modulus of all three phases sharply decreases shorty after the load application and until the day 4 or 7, depending on the phase. Then, from day 7 on until the last day, it slightly increases, with the exception of day 42. Unlike in the compression sample, the fraction of phase 1 increases with the sample age, that of phase 2 decreases, whereas that of phase 3 scatters between 17 % and 25 %. In this sample also, all phases are stiffer than in the sample without load. However, the moduli of the phases

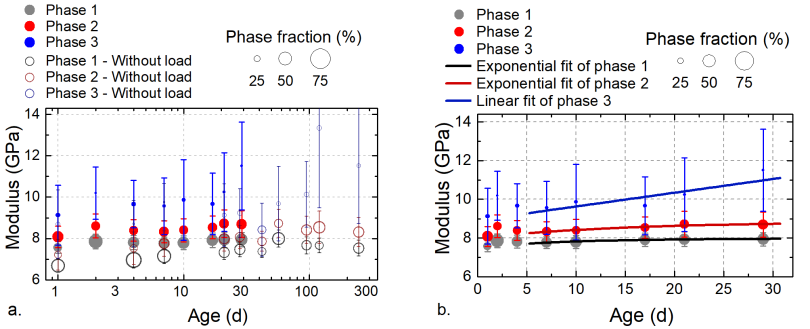

Figure 5.14: (a) Three-phase modulus deconvolutions of mortar under compression at various ages, compared to those of the mortar without load, and (b) phases evolution over sample age in the mortar under compression.

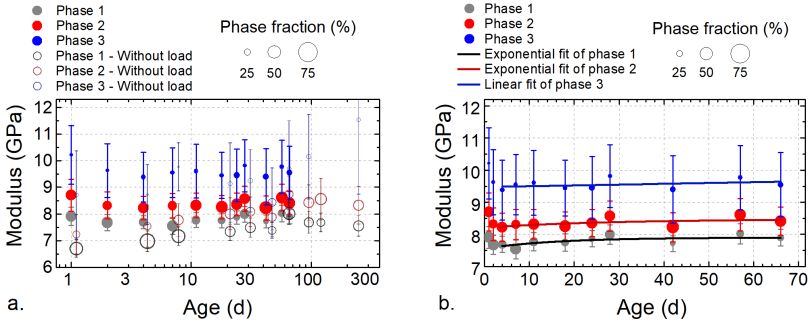

Figure 5.15: (a) Three-phase modulus deconvolution of mortar under tension at various ages compared to that of the mortar without load, and (b) fit of the elastic phases evolution over sample age.

increase in the similar way in both samples after the 7th day, indicating that the load might not have an effect on the sample aging after the 7th day.
In the shear sample, the mean modulus of all three phases increases after the load application and then scatters until day 18 around their values on day 4. Also the phase fractions of all phases scatter, and do not show a clear trend. All phases of this sample are also stiffer at all measured ages than those of the sample without load. Comparing the corresponding phases of both samples

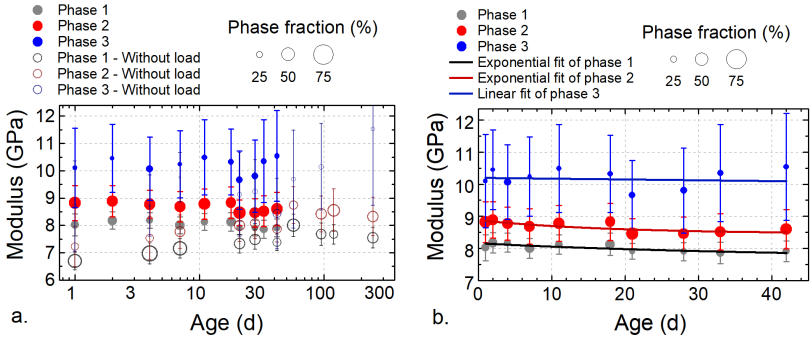

Figure 5.16: (a) Three-phase modulus deconvolution of mortar under shear at various ages compared to that of mortar without load, and (b) fit of the elastic phases evolution over sample age.

one by one, the difference on day 1 is greater than or equal to 1.2 GPa. But the sample under shear also exhibits a lower stiffness increase with age of all phases than all other investigated samples. For example, after 20 days, the difference in mean modulus between the first phases, resp. second phases, of both samples is lower than 1 GPa. Unlike the other samples under load, the phase moduli do not evolve similarly to those of the sample without load. This indicates that the applied shear load had a different effect on the sample microstructure than the applied tensile or compression loads.

Aging trends

Cement pastes and concrete are known to age for months and even years after mixing [139, 140], as the total porosity decreases with the degree of hydration and the age of the cement paste. But the aging of the stronger and stiffer cement paste compounds is slower than the aging of the softer and more compliant compounds. Thus, the two most compliant phases of all mortar samples were fitted with an exponential function

$$E_1(T) = E_{10} - E_{11} e^{-\frac{T}{T_{1/2}}}$$

with E_{10} the modulus at infinite age, E_{11} the modulus variation amplitude during the aging, T the sample age and $T_{1/2}$ the half time of the phase aging. And the stiffest phase was fitted with a linear function

$$E_2(t) = E_{20} + E_{21}T$$

with E_{20} the modulus value at infinite age and E_{21} the modulus increase per day. The choice of a linear fitting curve for this phase was also corroborated by the high scattering of the stiffest phase in all samples after 60 days.
The phases of the sample without load were fitted over the whole age range. The phases of the samples under external load, however, were fitted over the minimal age range for which all phases encountered a monotonic aging, i.e. from days 7, 4 and 2 for the compression, tension and shear samples, respectively. This aims to encounter for short-term variation of the phases properties potentially induced by the load application.
Figure 5.17 shows the aging trends of the elastic phases of the mortar sample without load. For the samples under load, the aging trends are shown in Figures 5.14b, 5.15b and 5.16b for the compression, tension and shear samples, respectively.
Table 5.4 summarizes the parameters and r_a^2 of the aging trend functions for all phases and in all investigated samples. In general, the r_a^2 show large variations with the considered sample and phase, but the highest r_a^2 in the compression sample indicate that its distributions are describe best by the aging trend functions, followed by those of the sample without load. The linear fits of phase 3 in the tension and shear samples have a negative r_a^2, which can be considered as 0[1]. This confirms the large scattering of the phase 3 over the sample's age noted in the discussion of the deconvolution. The tension and shear samples also have very low r_a^2 for the phases 1 and 2. Despite this, the aging trend functions were used for all samples to facilitate the aging com-

[1] see e.g. `https://www.originlab.com/doc/Origin-Help/Details_of_R_square`, visited on 8th September 2018

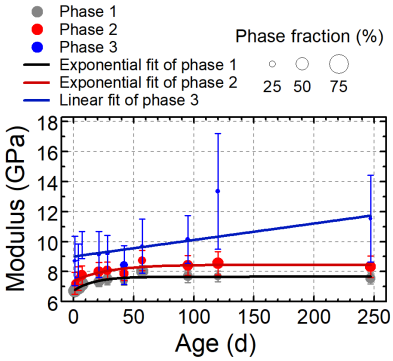

Figure 5.17: Exponential or linear fits of each phase of the function fitting the modulus distribution in mortar over the sample age.

Table 5.4: Aging fit parameters and r_a^2 for the three phases of the modulus deconvolution of the mortar samples with and without load.

	E_{10} (GPa)	E_{11} (GPa)	$T_{1/2}$ (d)	E_{20} (GPa)	E_{21} (GPa/d)	r_a^2 (-)
Sample without load						
Phase 1	7.65	0.92	17	–	–	0.786
Phase 2	8.45	1.08	29	–	–	0.646
Phase 3	–	–	–	9.0	0.011	0.294
Sample under compression load						
Phase 1	8.0	0.46	9.2	–	–	0.923
Phase 2	8.8	0.84	15	–	–	0.878
Phase 3	–	–	–	8.9	0.071	0.625
Sample under tensile load						
Phase 1	7.9	0.34	16.1	–	–	0.279
Phase 2	8.5	0.26	27.5	–	–	0.048
Phase 3	–	–	–	9.5	0.0024	−0.006
Sample under shear load						
Phase 1	7.7	−0.47	42	–	–	0.516
Phase 2	8.5	−0.42	17.2	–	–	0.478
Phase 3	–	–	–	10.2	−0.0025	−0.11

parison of individual phases in the mortar samples under various external loads.

While comparing the aging of individual phases in the sample without load, the two most compliant phases (phase 1 and 2) show similar exponential aging (modulus increase per day is around 1 GPa, aging half time of 23 ± 6 d), but with phase 1 being more compliant by 0.8 GPa than phase 2.

Comparing the $T_{1/2}$ times of the compression sample and the sample without load, the application of a compression load during the sample curing accelerates the modulus aging of all phases. But at the same time the parameter E_{11} indicates that the modulus increases is lower in the compression sample than in the sample without load. Moreover, the modulus of the phases at day 1 in the sample under compression is higher than in the sample without load (see Figure 5.14a), whereas the difference between the samples is lower on day 29, the highest investigated day of the compression sample, than on day 1. Similarly, the modulus at infinite age of the two most compliant phases is only 0.35 GPa higher in the compression sample than in the sample without load. Thus, the hypothesis is expressed that the maximal modulus of the phases, at infinite age, is limited by the reactants and not by the initial sample modulus, nor by the load applied during the curing reaction. This would explain the comparatively lower increase of the modulus aging in the compression sample compared to that in the sample without load.

Unlike the compression load, the application of a tensile load during the sample curing decreases the amplitude of the modulus increase E_{11} in phases 1 and 2 of more than 60 % and 26 % compared to those of the sample without load and the compressed sample, respectively. However, the modulus at infinite age E_{10} of these phases are nearer to those of the sample without load than to those of the compression sample, although their modulus on day 1 is much higher. Thus, the hypothesis that the maximal modulus of the phases is more influenced by the reactants and less by the initial sample modulus

or by the sample loading during the curing reaction, is corroborated by the sample under tension.
Finally, the shear sample exhibits a modulus at infinite age E_{10} in the two most compliant phases quite similar to those of the sample without load (with only 0.05 GPa difference), but it also had higher modulus on day 1. Moreover, the modulus variations with age E_{11} and E_{21} are negative for all phases of this sample: their modulus decrease with the sample age. This decrease might be related to high stresses in the sample which led to large macroscopic deformation (see Figure 5.10b), which increased with the loading duration, i.e. the sample age.

5.3.3 Hardness evolution

Deconvolution

The hardness CDFs of the sample without load (Figure 5.7b), and the samples under compression (Fig. 5.8b), tensile (Fig. 5.9b) and shear loads (Fig. 5.10b) were fitted at each investigated age with a single Gaussian distribution.

Mortar sample without load Figure 5.18a shows the deconvolution of the sample without load on day 95. Around 93 % of the hardness distribution is fitted well with a single Gaussian. Indeed, the one phase could not always fit the whole hardness distribution, and the phase fraction was not restricted to be one in the fitting algorithm. This automatically leads to phase fractions below 100 %. The rest of the distribution is located in the first 5 or the last 10 percentiles of the distribution, i.e. at the lowest and highest hardness values. Despite this, the goodness-of-fit criterion r_a^2 was high on that day, reaching 0.996, and the mean r_a^2 value for all investigated ages was 0.994.
Figure 5.18b presents the properties of this single hardness Gaussian phase at each age of the sample without load. Each circle represents the hardness phase at one age: its center is located at the mean hardness value and the error bar is the phase hardness standard deviation. The circle size is proportional

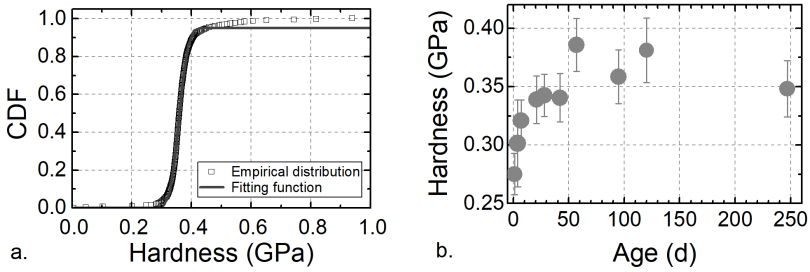

Figure 5.18: (a) Distribution of the mortar hardness on day 95 fitted with one Gaussian function, and (b) comparison of the hardness fitting phases at each investigated mortar age. In (a), the highest hardness values of the CDF are not shown to better display the core of the hardness distribution.

to the phase fraction, which varies between 89 % and 100 %, depending on the investigated age.

The mean value of the hardness phase increases monotonically with the sample age until the 42nd day. Then, the mean hardness scatter around 0.375 GPa and no clear trend can be observed. This variation could derive from a macroscopic heterogeneity (porosity, sample composition...) of the sample, as different sample locations were tested at each age.

Samples under external load Considering the high r_a^2 of this one-phase hardness model in the sample without load, it was also used for all remaining samples at all ages. In the sample under compression (Figure 5.19a), the fit r_a^2 were greater than 0.996 (day 29) and had a mean value (0.9966) higher than that of the sample without load. This corroborates the plausibility of the one-phase hardness model in the mortar. Also, the sample under compression is harder than the sample without load at all investigated ages, but both sample show a similar increase of the hardness after the 7th day.

In the tension sample, the r_a^2 of the one-phase fits were even larger than for the compression sample (Figure 5.20a), and had a mean value of 0.9975. Also, the hardness is higher by at least 10 MPa than that of the sample with-

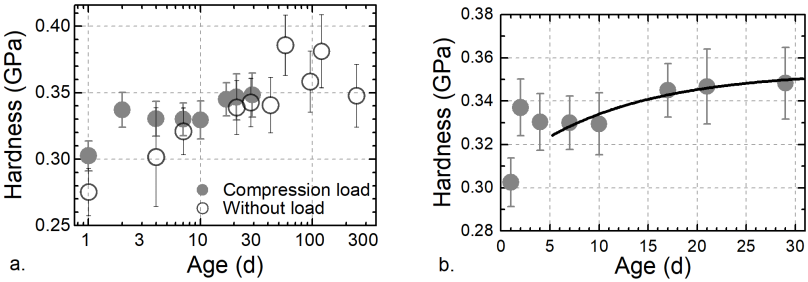

Figure 5.19: (a) Deconvolution of the hardness of the compressed mortar sample with one Gaussian phase, compared to that of the sample without load, and (b) exponential evolution over sample age of the hardness phase in the compressed sample.

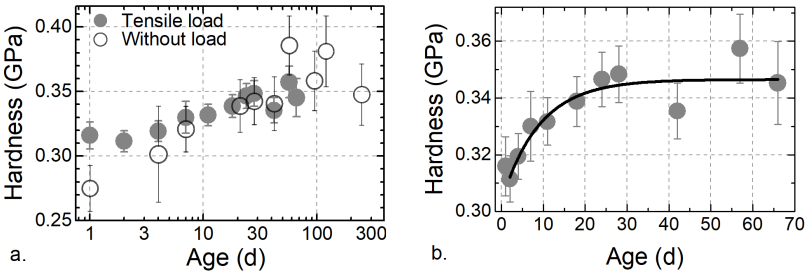

Figure 5.20: (a) Deconvolution of the hardness of a mortar sample under tension, with one Gaussian phase, compared to that of the sample without load, and (b) exponential evolution over sample age of the hardness phase in the mortar sample under tension.

out load until day 28. The difference is higher at the early ages, i.e. during the first seven days. Between 7 d and 29 d, the hardness of both samples show a similar increase. After day 28, however, also the hardness of the tension sample scatters around 0.35 GPa.

In the shear sample, the one-phase fit does not provide as good as results than in the other samples under external load (Figure 5.21a): the mean fit r_a^2 is lower (0.9959) and only 91 % of the whole distribution at least is fitted by the single Gaussian, against 93 % in the other samples under load. However, these statistics still indicate better fits than those of the sample without load.

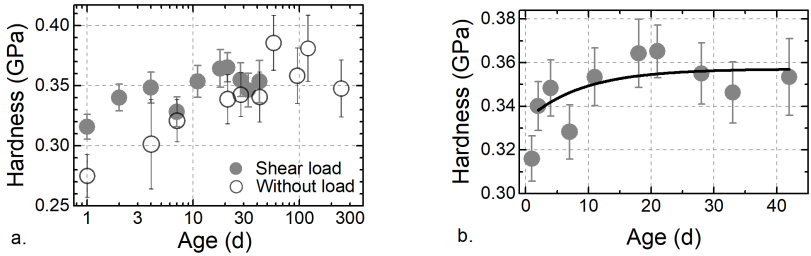

Figure 5.21: (a) Deconvolution of the hardness of the mortar sample under shear, with one Gaussian phase, compared to that of the sample without load, and (b) exponential evolution over sample age of the hardness phase in the mortar sample under shear.

The hardness of the sample under shear is larger than or equal to the hardness of the sample without load. The difference is larger at the early ages, with the shear sample being harder by 40 MPa on day 1. Between the first and the 21st day, the mean hardness of both samples show a similar increase. After 28 days, the hardness in the sample under shear decreases and eventually reaches a plateau at around 350 MPa.

Aging trends

To better compare the hardness aging between the samples, an exponential function $H(t) = H_0 - H_1 e^{-\frac{T}{T_{1/2}}}$ was used to fit the hardness phase of all mortar samples over the sample age. H_0 is the theoretical hardness at infinite age and H_1 is a scaling factor describing the hardening. $T_{1/2}$ is the half time of the aging. The hardness of the sample without load was fitted over the whole age range, and that of the samples under external load were fitted over the same age range as for their modulus phases, i.e. from days 7, 4 and 2 for the compression, tension and shear samples, respectively. Figure 5.22 shows the fitting function for the sample without load, and Figures 5.19b, 5.20b and 5.21b for the compression, tension and shear samples, respectively. The fit parameters H_0, H_1 and $T_{1/2}$, as well as the goodness-of-fit criterion r_a^2 of all samples are summarized in Table 5.5.

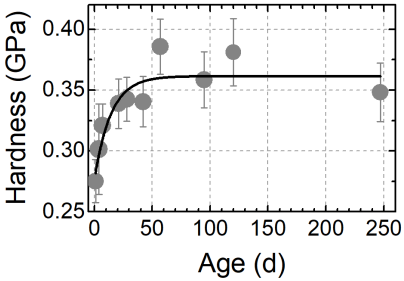

Figure 5.22: Exponential fit of the hardness Gaussian distributions of mortar over the sample age.

Table 5.5: Aging fit parameters and r_a^2 for the hardness deconvolution of the mortar samples with and without load.

Sample	H_0 (MPa)	H_1 (MPa)	$T_{1/2}$ (d)	r_a^2 (-)
Without load	360	85	14	0.798
Compression load	354	46	11.8	0.812
Tensile load	350	43	9.1	0.838
Shear load	357	24	9.9	0.150

The low fit r_a^2 of the sample without load highlights the large variations in the mean hardness values. The r_a^2 of both the compression and tension samples are higher, which indicates that the scattering of the mean hardness is decreased. This decrease might be related to the lower number of investigation runs for these samples than for the sample without load. The much lower r_a^2 of the shear sample, however, reflects the large scatter of its mean hardness with the sample age.

In all samples under external load, the aging half time is significantly lower than that of the sample without load, and the hardening scaling factor H_1 is at least twice smaller (and even four times smaller in the shear sample). This indicates a quicker hardening reaction with a much smaller amplitude.

The hardness at infinite age H_0, however, is relatively similar between all samples.
Thus, compared to that of the sample without load, the sample curing is accelerated by the application of an external load, and the total hardening is reduced. It must be noted, however, that the hardness on day 1 is higher for all samples under external load than for the sample without load. Also, the hardness decrease in the shear sample needs to be investigated further, as it might be related to the large deformations occurring in the material.
To conclude, the mortar hardness behaves as a single homogeneous phase, despite the presence of three elastic phases in the material. Indeed, the deformation mechanisms behind the elastic modulus and the hardness are different: the hardness characterizes the elasto-plastic deformation of a material, whereas the modulus characterizes the linear-elastic deformation. Moreover, the plasticity of a material may be more influenced by the interfaces between the material phases, than by their mechanical properties.

5.3.4 Evaluation

The evolution of the mechanical properties with the sample age is different depending on the external load applied. The aging trends of the modulus and hardness phases of the different samples are compared with each other, using their value on day 1 (the measurement day without external load in all samples) as reference.

Elastic modulus

The mean modulus of the two most compliant phases (phases 1 and 2) of the mortar samples under various long-term loading were compared to their value on day 1 (Figure 5.23). As the stiffest phase (phase 3) encounters a large scattering in all samples, its aging behavior is not discussed in this section. The relative modulus aging of both phases in all samples were fitted with exponential functions to highlight the very different aging trends.

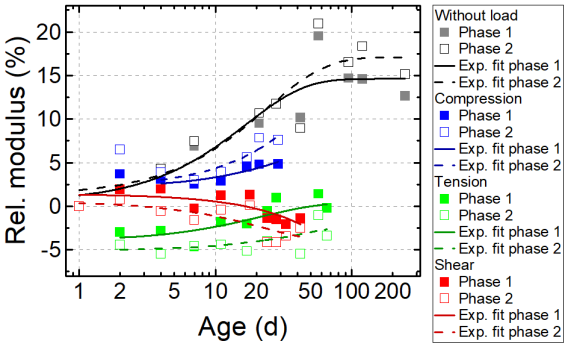

Figure 5.23: Mean modulus of the 1st and 2nd phases of mortar samples under various long-term loading compared to their values on day 1, and associated exponential fits.

The sample without load has the highest modulus increase with age for both phases. The modulus increases by up to 15 % to 17 % within the first 70 days. Both phases exhibit a similar modulus increase, which hints towards similar physico-chemical aging. The moduli of these phases in the sample under compression increase less with sample age and more slowly than that of the sample without load: they reach only half of the modulus increase without load at the age of 30 days for both phases, and do not seem to be stabilized on day 29. This delay in the modulus increase with sample age might be related to the high modulus increase of 5 % on the day following the load application.

By contrast, the application of a tensile load decreases the modulus of 4 % in one day. This drop is followed by a slow increase of the modulus of phases 1 and 2. The aging of these two phases seems to stabilize after 50 days.

Finally, the modulus aging of the sample under shear load exhibits a different trend: the mean modulus of all phases decreases with sample age. This may be related to the large deformation (up to 14 %) the sample encountered, in particular after 20 days, which probably induced material damages. Both investigated phases of this sample get more compliant with sample age in a similar way, without reaching a stabilized value at higher ages.

Hardness

Figure 5.24 summarizes the hardness evolution compared to that of the sample on the sample's first day (i.e. without load). The hardness evolution of all samples was fitted with an exponential fit to facilitate the comparisons.
The mortar sample without load encounters the largest hardness aging, with up to 30 % increase within the first 50 days. The sample under long-term compression encounters the smallest hardness aging with only 10 % increase within the first 30 days, whereas the samples under shear and tensile loads had their hardness increase by 10 % to 15 % already within 10 to 20 days. Unlike the modulus phases, the hardness seems to stabilize at higher ages in all samples.
The hardness evolution with age depends of the applied long-term load. Applying a long-term static load decreases the total hardness increase with sample age in all samples. At first sight, the type of loading does not seem to influence the hardness aging: see for example the similar paths of the relative hardness between the sample under compression and the sample under shear stress over the first 20 days.
However interestingly, the height of the long-term stress in the sample plays a role. When no or a moderate long-term stress (below 40 %, see Table 5.1) is applied, as for example in the sample under tension until the age of 51 days, the fraction of the most compliant phase tends to diminish, whereas the fraction of the second most compliant phase increases. This effect might be related to a decreasing pore fraction in the sample, an ongoing curing of the polymer, or ongoing hydration reactions of the cement. All of these would shift the modulus distribution of the sample towards higher values. By contrast, when a higher long-term stress is applied, as for example in the sample under shear, the phase fractions do not particularly evolve with age, whereas the mean modulus and hardness both decrease with age. The shear sample encounters physical degradation, which seems to affect all phases, in particular after the age of 20 days.

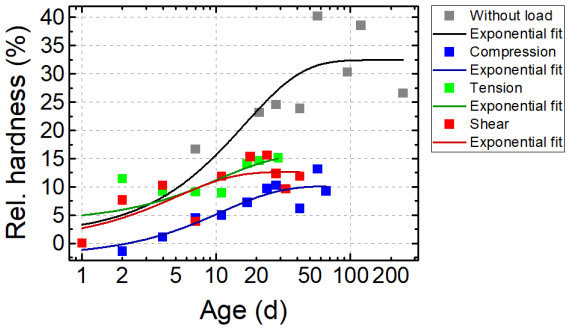

Figure 5.24: Mean hardness of different mortar samples compared to those on day 1, and associated exponential fits.

Thus, to conclude on the aging of the samples under load, two phenomena with concurring effects and different time constants play a role in the material, the hardness increase due to the sample curing and the hardness decrease due the material degradation induced by the applied long-term load. The latter effect limits the hardness increase and might even lead to a decrease of the sample's hardness, as in the shear sample.

5.4 Summary

5.4.1 Mortar microstructure and its aging

The microscopic investigations and the nanoindentation experiments give some hints about the mortar microstructure and its evolution under long-term loading.

At least two phases with low fractions could be distinguished out of a matrix from a µ-CT scan: particles of higher density, and pores. The particles are likely to be unhydrated cement particles, thus relatively stiff. Their presence was confirmed by the producer, who estimated their characteristic size as 5 µm to 6 µm, thus being in good agreement with our estimations from the µ-CT scan. The matrix surrounding the particles was considered as a homo-

geneous phase with volume fraction over 97 %, which contains the rest of the cement paste components and the polymer. Thus, it is expected to be softer and more compliant than the particles.

Nanoindentation statistical analysis showed a reproducible three-phase distribution of the mortar elastic properties, independent of the sample age and long-term load. The two most compliant phases showed an exponential aging in each sample, whereas the stiffest phase behaved in a more scattered way, which could be approached by a linear aging. The volume fraction of the phases in all samples were around 40 %, 40 % and 20 % for the phases 1, 2 and 3, respectively, with variations of up to 10 % to 20 % depending on the sample and the age.

At first sight, he sample microstructure as observed from the µ-CT scan do not show a clear correlation with the mechanical properties distribution from the nanoindentation experiments. They seem to provide different information on the mortar microstructure. Indeed, the nanoindentation experiments have a resolution in the range of 10^2 µm^3 to 10^3 µm^3, i.e. one to two orders of magnitude larger than the µ-CT scan resolution. Thus, the volume fractions from the microscopic and nanoindentation investigations cannot be directly compared. Another factor for this dissimilarity may be the differences between the surface and the core microstructure. The sample preparation for nanoindentation of the samples under load involved pouring on a smooth silicone surface, without further surface preparation. This may have influenced both the porosity and the particles distribution at the surface. Also, having placed the same samples under low pressure conditions might have reduced the total porosity and have accelerated the curing reaction of the epoxy, the hydration reaction of the cement or the interaction reactions between the polymer and the cement in the mortar. Finally, considering the size differences between the different elastic phases from µ-CT, the elastic properties under an indent are likely to be a mixed answer of the mechanical properties of the pores, the matrix and the unhydrated cement particles. Thus, the measured elastic properties in the nanoindentation experiments reflect the local

distribution of the pores, the particles and the matrix under each indent on the surface, and the elastic phases defined from the statistical analysis reflect the statistical spatial distribution of the microstructure. The most compliant phase probably contains more pores and fewer particles than the other phases, whereas the stiffest phase probably contains the most particles and fewer pores.

5.4.2 Applicability of the SNT

The mortar microstructure was investigated and its evolution under a long-term static load characterized. The nanoindentation statistical technique does not enable to characterize the individual phases of the mortar microstructure at the large chosen investigated depth, which was limited by the quality of the sample surface. However, the SNT enabled to investigate the modulus distribution by decomposing it in three phases, the aging of which giving some insights into the long-term physico-chemical aging phenomena of the mortars.

In particular, some trends regarding the aging behavior of the mortar under various stress states have been determined thanks to the SNT. The aging of the sample without load showed an exponential increase of all elastic and hardness phases. Regarding the aging of mortar under long-term load, the application of the load did not significantly increase the phase properties of the samples at highest ages and even seemed to reduce the overall modulus increase with age. However, the higher modulus and hardness values measured in these samples on day 1, before the load application, might have interfered here with the effects of the long-term load. Large applied stress (more than 40 % of the short-term failure stress), in particular at early mortar ages, under 50 days, seemed to induce damages in the material, and, thus, to significantly decrease its mechanical properties. Similar experiments repeated with various values of the same external load might give more insight on the effect of the load value on the aging behavior of the mortar.

6 Nanoindentation of polymer-modified cement pastes

Polymer-modified concretes (PCC) and cement pastes (PMC) are used for their improved "durability, workability and adhesive strength" [141] compared to those of pristine cement-based materials. However, the microstructure of the PMC and the effect of the polymer-modification on the material mechanical properties at microscopic scale are not fully understood yet. The elastic heterogeneity of PMC was investigated using the statistical nanoindentation technique, at various polymer compositions, concentration and for two ages of the materials. This research was done in cooperation with Luise Göbel, from the Bauhaus-University of Weimar, Germany. Some results were used as input parameters for a multi-scale modelling of the elastic properties of PCC [141]. A good agreement between the experimental multiscale study and the predicted properties from the model results was found.

6.1 Experimental details

6.1.1 Material description and sample preparation

PMCs with *CEM I 52,5 R* cement, three different polymers, two polymer-to-cement ratios $P:C$(5 and 20 % in mass) and a water-to-cement ratio of 0.4 were mixed, as well as a reference cement paste without polymer. The samples are named with the nomenclature

$$polymer\ short\ name - P:C$$

whereas the cement paste without polymer is named *Reference*.

Table 6.1 summarizes the composition and delivery condition of each polymer. Table 6.2 describes the mixing procedure for each sample, depending on the delivery condition of the used polymer.

All samples were poured into self-made molds of silicone rubber (ADDV-42, R&G Faserverbundwerkstoffe GmbH, Waldenbuch, Germany), with a sample size around $1 \times 1 \times 0.3\,\mathrm{cm}^3$. After curing, each sample was carefully sawed into four parts of equivalent area and one of these smaller samples was fixed with cyanoacrylate-based glue on an aluminum sample holder. To reach the surface requirements necessary for nanoindentation, the samples were polished prior to the first run of indentation. The manual polishing procedure included grinding with SiC paper of decreasing sizes from 600 to 4000 with water as lubricant. The first step was continued until the samples were plan. The further steps duration were around 3 minutes each. After grinding, the samples were polished with various alcohol-based diamond suspension of 3 µm, 1 µm and 0.25 µm diameter. Between each step, the samples were cleaned with alcohol in an ultrasonic bath and quickly dried with an air spray at around 50 °C and the surface was checked for roughness and quality using a light microscope (Nikon Eclipse LV150N) equipped with objectives of 4, 10, 20, 50 and 100 of magnification. The polished top surface of each sample was investigated with light microscopy, and is shown on Figure 6.1. The differences in color are related to varying microscope settings.

A graphical user interface line-cut procedure (GUI_linecut V2.0 by M. Funk, S. Meister, IAM, KIT, Germany, 2012) implemented in Matlab (Release 2015b, The MathWorks, Inc., Natick, MA, USA), improved to also handle the case of a 2-phase material, was used to determine the characteristic size of the particles and their phase fraction within the matrix. Therefore, the chord lengths of the particles and the matrix phases were manually selected from a picture, and a phase was associated with each chord. The fraction of the j^{th}-phase A_j was calculated as $A_j = \frac{\sum_p l_{j,p}}{\sum_p l_{j,p} + \sum_q l_{k,q}}(\%)$, where

Table 6.1: Composition, short name, commercial name, company, condition and minimal film forming temperature (MFFT) of some polymers used in the investigated polymer-modified cement pastes

Polymer short name	P1	P2
Scientific name	styrene acrylic acid ester copolymer (SA)	styrene acrylic acid ester copolymer (SA)
Commercial name	Vinnapas® 2012 E	Mowilith® LDM 6880
Producing company	Wacker Chemical Corporation Adrian, Michigan, USA	Ha-Be Betonchemie GmbH & Co. KG Hameln, Germany
Condition	powder	dispersion
MFFT (°C)	5	30

Polymer short name	P3
Scientific name	styrene-butadiene copolymer (SBR)
Commercial name	Styrofa® D 623 na
Producing company	BASF Corporation Charlotte, North Carolina, USA
Condition	dispersion
MFFT (°C)	18

Table 6.2: Mixing procedure of polymer-modified cements depending of the polymer state

Dispersion		Powder	
Duration	Action	Duration	Action
15 s	mix water and polymer		mix cement and polymer
15 s	pour cement powder	15 s	pour water
60 s	slow stirring	60 s	slow stirring
60 s	break	60 s	break
60 s	quick stirring	60 s	quick stirring

$j,k = 1,2; p = 1..n, q = 1..m$, $l_{j,p}$ and $l_{k,q}$ are the p^{th} and q^{th}-chord lengths l of phases j and k measured during the line-cut procedure.

To investigate the surface roughness of the samples prior to nanoindentation testing, a confocal laser microscope[1] was used. If necessary, the image tilt was corrected based on the mean surface tilt. From the surface topology, a root mean square areal roughness parameter $R_q = \sqrt{\frac{1}{n}\sum_{i=1}^{n} y_i^2}$ can be calculated. As the areal roughness depends on the scan size [99], its scan size was estimated for each measurement and was typically 3000 to 8000 μm^2 for the smaller scans and around 1.2×10^6 μm^2 for the larger scans.

Besides PMC samples and the reference sample, also pure polymer samples were prepared under the same conditions as for the PMC pastes. They were glued on Al cylinder sample holder so that the smoothest surface from the mold could be tested with nanoindentation. Finally, one sample with 0.5 W:C ratio and 0.05 P:C ratio of P1 was prepared in a similar way, and tested as part of the discussion of the analysis method (see Section A.2.1).

6.1.2 Nanoindentation methods

Polymer testing

The complex modulus of the three polymers P1, P2 and P3 were measured with nanoindentation at room temperature, following the method presented by Herbert et al. in 2008 [142] and refined in the following year [67]. The method requires the use of a flat punch and its most important features are an initial pre-compression of the sample "to establish full contact with the face of the flat punch", then "a stabilization period that allows the sample to reach a state of equilibrium", and finally "higher frequency measurements conducted with a phase-lock amplifier (PLA), which characterize the combined frequency response of the sample and the instrument" and are conducted at a target amplitude of the displacement oscillation and frequency [67]. The frequency of 45 Hz was chosen as the same frequency as the PMC nanoinden-

[1] VK 9710K, KEYENCE Corporation, Itasca, IL, USA

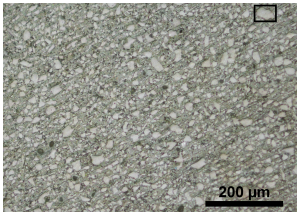

(a) Reference, cement paste

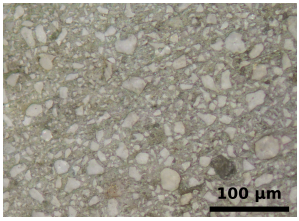

(b) P1-0.05

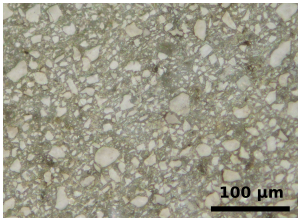

(c) P1-0.2

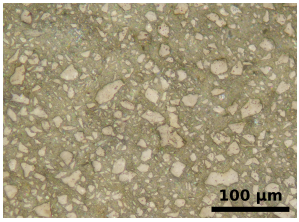

(d) P2-0.05

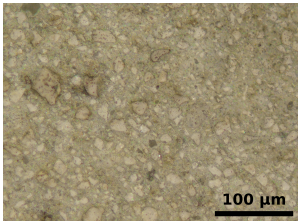

(e) P2-0.2

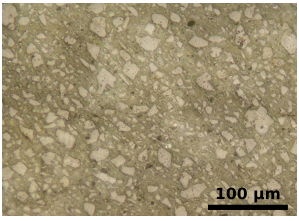

(f) P3-0.05

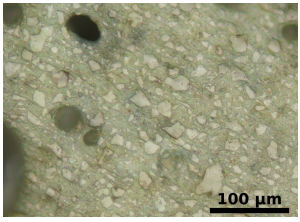

(g) P3-0.2

Figure 6.1: Surface of polished PMC samples with (b-g) various polymers and polymer contents, and (a) the pure cement paste imaged with light microscopy. The black square indicates a representative particle.

tation tests with CSM, as presented in the following paragraph. A diamond conical punch with flat tip of 100 µm diameter and angle of 60° is used. 10 to 14 indents were done at a pre-compression depth of 2 µm (P1) to 3 µm (P2 and P3) and a displacement amplitude of 20 nm. A Poisson's ratio of 0.4 was assumed for all polymer samples.

Nanoindentation of PMC pastes

Each polymer-modified cement paste was tested two times, at the age of 27 to 29 days (i.e. four weeks) and 55 to 57 days (i.e. eight weeks). As in the mortar, 8 fields of 26×26 indents were programmed on each sample for a total test duration of around 8 h per sample. The nominal indentation depth was set to 1 µm and only the indents with an actual indentation depth range between 0.6 µm and 2 µm were analyzed. The indentation modulus was analyzed for all samples assuming Poisson's ratio to be 0, ε equal to 0.75 and β to 1.05 (see Section 2.2.1). The hardness was not investigated.
The number of valid indents in the PMC pastes is summarized in Table 6.3 and depends on the sample and the measurement day. In P3-0.2, the numbers of successful indents were at least three to four times less than in all other samples, which causes the results from this sample to be less reliable, as shown in the following sections.

6.1.3 Statistical analysis

The EM procedure described in Section A.1.1 was used to investigate the number of phases in the modulus distribution of P1-0.2 and the reference sample at various ages. Functions with one to four or five phases were used to fit the modulus distribution at each age and the number of phases is discussed based on the BIC minimum and the phases properties as determined from the deconvolution.
In a second step, the aging of the PMC pastes elastic properties was also investigated using the LM procedure (see Section A.1.1) with a two-phase

Table 6.3: Number of valid indents in each PCC sample on each measurement day

Sample	Number of valid indents	
	day 28	day 56
Reference	2054	2927
P1-0.05	2189	2332
P1-0.2	1611	2008
P2-0.05	3806	4159
P2-0.2	2302	2929
P3-0.05	3444	4382
P3-0.2	475	812

fitting function. The deconvolution results from both procedures are then compared.

6.2 Results

6.2.1 Microstructure and surface roughness

The polished surface of the PMC samples is shown in Figure 6.1. The surface of each sample exhibits heterogeneity, with inclusions of white, grey or even reddish particles in a matrix. Additionally to this structural heterogeneity, the sample P3-0.2 also presents a large number of pores, estimated as 20 % using the line-cut procedure on a surface of $530 \times 2200\,\mu m^2$. The bubbles were probably embedded unintentionally during sample preparation and might influence the mechanical properties.

Depending on the sample, the roughness R_q lies between 0.37 µm and 0.74 µm (see Table 6.4). Only two of the PMCs exhibit a larger surface roughness than 0.5 µm. It should be noted that, measured as an example on the reference sample, the inclusions present a roughness four times lower than the surrounding material (matrix) between them or than the sample material over a large surface.

Table 6.4: Roughness R_q of the PMC samples and area of the respective zone of measurement.

Probe	Roughness (µm)	Area (µm^2)	comments
Reference	0.64	$>1 \times 10^6$	Very large area
Reference	0.12	190	On a particle (see Figure 6.1a)
P1-0.05	0.47	3300	
P1-0.2	0.74	7200	
P2-0.05	0.38	5700	
P2-0.2	0.37	7900	
P3-0.05	0.37	6400	
P3-0.2	0.50	15400	

The maximal indentation depth was chosen as 1 µm. This depth was considered as a trade-off between surface roughness and accuracy in the phase characterization (see Section 2.2.5), though only equal to two times the roughness of most samples. As a consequence, the error in the nanoindentation measurement of the PMC due to the large surface roughness is not negligible. However, considering the large area used for the roughness measurement, the roughness is considered to be constant over the sample surface, and thus the error is constant between two measurements at various ages (and also various locations). Also, as the surface roughness is similar for all samples, the nanoindentation results can be compared well with each other.

6.2.2 Polymer viscoelastic properties

The storage and loss moduli of the three polymers modifying the PMC pastes were measured. The storage modulus is a measure of the elastic, reversibly-stored energy in the polymer, whereas the loss modulus is a measure of the polymer viscosity.

P1 is the stiffest of the three polymers, as it has the highest storage modulus E_{st} (Figure 6.2). P1 and P2 have relatively similar loss moduli E_l, whereas

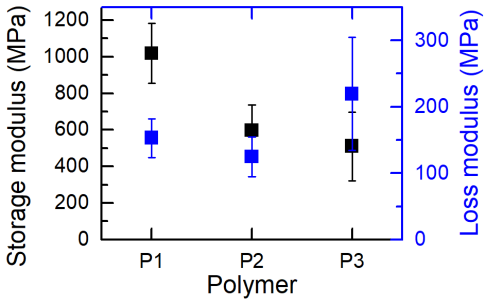

Figure 6.2: Storage and loss moduli of polymers used to modify the PMC pastes.

P3 is slightly more viscous. Thus, although they have the same polymer composition, P1 and P2 show different viscoelastic properties and Young's moduli. P3 presents a different viscoelastic behavior than both P1 and P2, with the lowest storage modulus and the highest loss modulus of the three polymers.

Young's modulus of the polymers is then calculated with the equation: $E = \sqrt{E_{st}^2 + E_l^2}$ [142] and is 1029 GPa, 610 GPa and 555 GPa for P1, P2 and P3, respectively. All three investigated polymers have elastic properties at least one order of magnitude lower than the cementitious phases [37, 87].

6.2.3 Effect of polymer on the elastic properties

The effects of the three different polymers on the elastic properties of the PMC pastes are compared, and depend on the polymer, the polymer content and the sample age.

First, the introduction of polymer lowers the elastic properties of the cement paste (Figure 6.3), independent of the polymer content. Indeed, the whole CDFs of the PMC pastes are located on the side of the lower modulus values of the reference sample CDF.

At lower polymer contents (Figure 6.3a), the influence of P3 is much larger than of P1 and P2: the median of the modulus distribution in each PMC

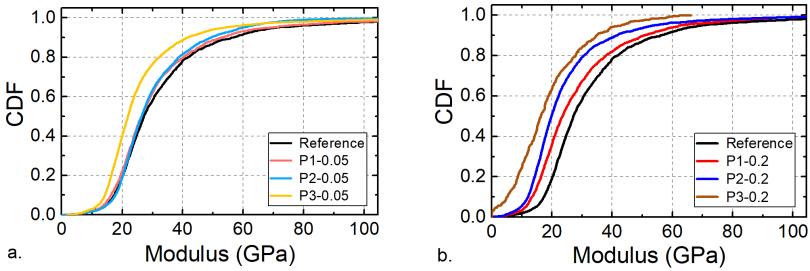

Figure 6.3: Elastic modulus (GPa) distribution variation with polymer type in polymer-modified cement pastes on day 28, with (a) low or (b) high polymer content.

paste is 26.4 GPa, 26.4 GPa and 21.9 GPa for P1, P2 and P3, respectively, and 27.2 GPa for the reference. P1 and P2 have similar effects on most part of the modulus distribution, whereas P2 generates a lower proportion of high modulus indents (from 35 GPa on) than P1.

At higher polymer contents (Figure 6.3b), all three samples show a decrease of their modulus properties compared to those of the reference. The intensity of this decrease is larger for P3, followed by P2 and finally by P1. A larger porosity with increasing polymer content might also play a role in the modulus decrease [49].

6.2.4 Effect of polymer content on the elastic properties

The influence of the polymer content on the modulus distributions in PMC pastes is investigated for each polymer in Figure 6.4. The modulus of the PMCs decreases with increasing polymer content. For example, the median of the modulus distributions in the PMC modified with P1, P2 and P3 are 23.6 GPa, 19.9 GPa and 16.4 GPa, respectively, for the high polymer content, but as large as 27.2 GPa in the reference. The difference between the PMCs and the reference sample is increased with increasing polymer content (see previous paragraph for the median of the low-polymer content distributions).

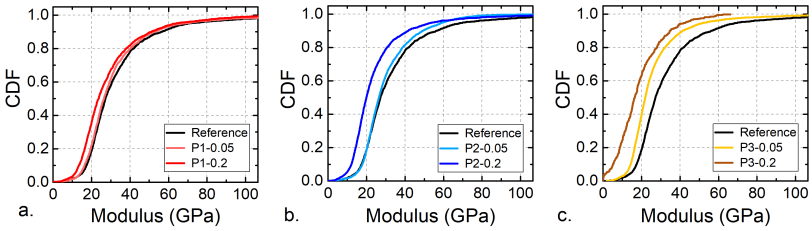

Figure 6.4: Variation of the elastic modulus cumulative distribution with the polymer content in polymer-modified cement pastes at age of 28 days, with (a) polymer 1, (b) polymer 2 and (c) polymer 3, compared to the modulus distribution of the reference sample without polymer modification.

The shape of the modulus distributions in P3-0.2 and P1-0.2 are similar to the reference. However, like in the low-polymer content samples, the distribution in P2-0.2 is more homogeneous, as indicated by the steeper increase of the CDF curve between 10 % and 80 %. P2 encounters the largest differences in the modulus distributions between the low-polymer and high-polymer contents, and P1 the smallest. In P3-0.2, the modulus distribution is less steep than in P3-0.05, indicating a less homogeneous distribution. However, probably due to the high sample porosity, the scatter in the modulus distribution of P3-0.2 is increased compared to that in P3-0.05, and the large number of indents under 5 GPa (around 9.4 %), which is present in no other distribution, indicates the poorer quality of the surface or even of the sample.

6.2.5 Effect of aging on the elastic properties

Figure 6.5 shows for example the modulus CDFs for two PMC samples, P2-0.05 and P2-0.2, at the ages of 28 and 56 days, and compared to that of the reference sample. The modulus distribution of P2-0.05 (Figure 6.5a) reveals that the difference in the modulus distribution of the sample at both investigated ages is smaller than for the cement paste without polymer (reference sample). Indeed, the reference sample becomes more compliant with age: most of the curve on day 56 lies on side of lower modulus values of the

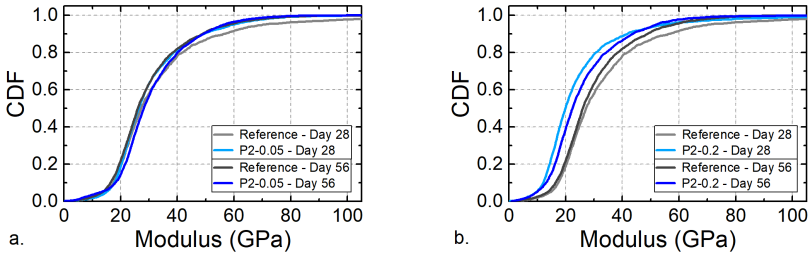

Figure 6.5: Elastic modulus distribution at 28 and 56 days in some PMC samples: (a) P2-0.05 and (b) P2-0.2, compared to that of the reference sample without polymer modification.

curve on day 28. It also becomes more homogeneous, as it has a steeper increase of the curve on day 56 than on day 28.

On the contrary, the modulus distribution of P2-0.2 (Figure 6.5b reveals that the sample modulus increases between age of 28 days and 56 days, as the distribution is shifted to higher modulus values. This modulus increase with age is not visible in the reference sample. The homogeneity of the sample is quite similar at the two investigated ages.

Thus, Figure 6.5 indicates a retardant effect of the polymer modification on the hardening reaction of the PMCs, in particular at large polymer content.

6.3 Discussion

To further analyze the modulus distribution of PMC pastes, the empirical modulus distributions were fitted with a weighted sum of Gaussian functions. First, the number of phases is discussed, and then the influence of the polymer modification, which depends on the polymer type, the polymer content and the sample age.

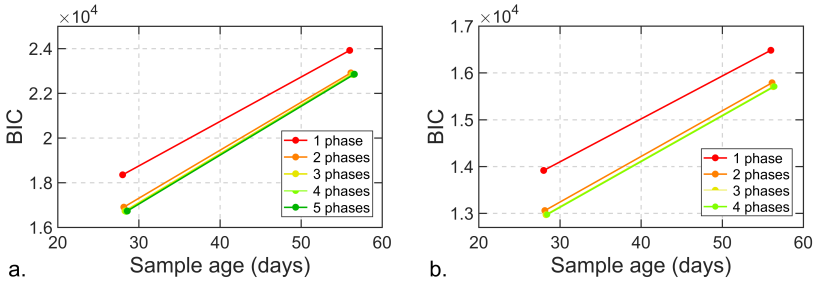

Figure 6.6: BIC of the elastic modulus distribution fit with varying number of phases at two investigated sample ages for (a) the reference and (b) the P1-0.2 sample.

6.3.1 Number of phases

The modulus distribution of the reference sample and P1-0.2 were investigated with the EM fitting procedure (as described in Appendix A.1.4), with a sum of one to four and five Gaussian functions for P1-0.2 and the reference, respectively. At each age, when comparing the fits with the lowest BIC and various number of phases, the number of phases of the fit that led to the lowest BIC indicates the optimum number of elastic phases in the material (Figure 6.6). In the reference sample, the lowest BIC is achieved at both ages for a four-phase fit (Figure 6.6a). However, the difference is small between the three-phase and the four-phase fits (0.13 % on day 28 and 0.05 % on day 56). Thus, the four-phase fit was considered in a first approach as the best number of phases in the reference sample, but a three-phase fit may also be relevant. This will be examined in a further step. In P1-0.2, the minimal BIC is achieved at both ages for a three-phase fit (Figure 6.6b). As the difference with the BIC of the two-phase fit is only 0.67 %, both fits will be compared in a further step.

The fits with lowest BIC for the modulus distribution of the reference and the P1-0.2 sample at age of 28 and 56 days are presented in Figure 6.7. Each phase is plotted as a circle located at the phase mean value, which size

is proportional to the phase fraction and with an error bar representing the standard deviation of the phase.
In the reference sample (Figure 6.7a), the four phases have mean values between 20 GPa and 100 GPa at both ages. The phases 1 and 2, i.e. the two most compliant ones, overlap with each other. The two stiffest phases do not overlap and describe the modulus distribution from 40 GPa upwards. On day 28, the phase fraction of phase 4, the stiffest phase, is 4.7 % but only 0.58 % on day 56, fractions that represents less than 100 indents at both ages. Moreover, for this phase, the ratio of the modulus standard deviation over its mean value is 32 % on day 28 and 40 % on day 56. For comparison, the same ratio for the most compliant phase is only around 19 %. This indicates that the stiffest phase of the distribution is very wide, i.e. has a large noise-to-signal ratio, and also has a small to negligible fraction. Thus, in the following, a sum of only two to three phases is used to fit the modulus distribution of the reference sample at both investigated ages.
In P1-0.2 (Figure 6.7b), the three phases have mean values between 15 GPa and 70 GPa at both ages. The two most compliant phases also overlap with each other, but less than in the reference sample. A similar reasoning for phase 3 of P1-0.2 as for phase 4 of the reference at both ages shows that phase 3 also has a large noise-to-signal ratio, with a small to negligible phase fraction, and in the following a sum of only two phases will be used to fit the modulus distribution of P1-0.2.
So, for better comparison between all samples, the modulus distributions of the reference and all investigated PMCs on both days will be investigated with a sum of two Gaussian phases.

6.3.2 Polymer influence

Figure 6.8a presents the two-phase deconvolution results of the PMC moduli at age of 28 days. Each circle center is located at the mean modulus of a phase, with the associated error bar as the standard deviation. The circle

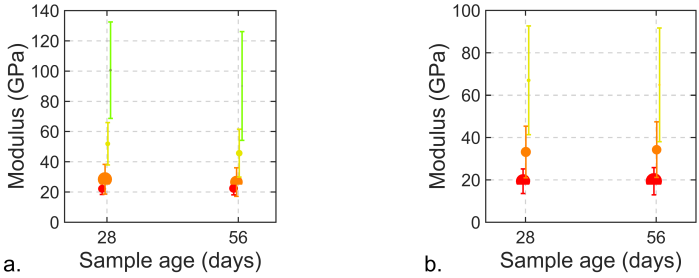

Figure 6.7: Optimal fit of the elastic modulus distribution fit at two investigated sample ages from high-speed nanoindentation of (a) the reference and (b) the P1-0.2 sample. The data points are shifted of one or two days around the measurement day for better visibility.

diameter is proportional to the phase fraction as indicated by the scale. For all samples except P3-0.2, the mean modulus of the most compliant phase (phase 1) lies between 18 GPa and 23 GPa with a standard deviation of 5 GPa to 6 GPa. The mean modulus of the stiffest phase (phase 2) varies from 31 GPa to 37 GPa with a standard deviation between 11 GPa and 16 GPa. The fraction of phase 1 is somewhat higher than the fraction of phase 2 with values between 50 % and 63 % and 35 % and 47 %, respectively. Note that the sum of the fractions of the two phases lies slightly below 100 %, at around 97 % to 98 %. This indicates that not all modulus values could be attributed to one of the two phases. The choice of number of phases discussed in the previous section probably led to the fact that some modulus values cannot be modeled by any of the phases, most of them being in the 2 % to 3 % highest modulus values.

Compared to that of the reference without polymer, the modulus of all PMC pastes is either constant or reduced with the modification with 5 % of polymer (Figure 6.8a). This is expected, as the polymers have a lower modulus compared to those of the cement paste phases: typ. $<$1.1 GPa (Figure 6.2) and 20 GPa to 150 GPa [37, 87], respectively.

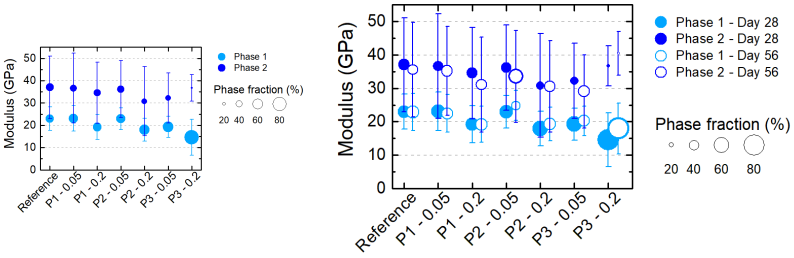

Figure 6.8: Distribution of the elastic phases of polymer-modified cement pastes (a) on day 28, and (b) on both days 28 and 56. The fraction of each phase is proportional to the circle area, following the phase fraction scale on the right.

At lower polymer concentrations, P3 has the greatest influence on the PMC paste modulus (Figure 6.8a). This correlates well with the previous tests on the polymer only, where P3 was found to be the most compliant polymer in this study (see Section 6.2.2). However, a larger porosity of the sample compared to that of reference would also lead to a decrease of the phases' stiffness.

Besides the polymer stiffness, factors such as the delivery state of the polymer and the minimal film forming temperatures (MFFT) also play a role in the PMC properties, as they would affect the polymer dispersion in the cement paste or the microstructure of the PMC paste [141]. Indeed, according to Göbel et al [141], "the M[F]FT of P1 is lower than the processing and storage temperatures; it does not form films in the hardened cement paste matrix. In contrast, polymers P2 and P3 form films which interpenetrate the cementitious matrix".

6.3.3 Polymer content

The polymer content also influences the elastic properties of the PMC pastes (see e.g. Figure 6.8a). At higher concentrations of polymer (20 % of the cement weight), all polymers reduce the modulus of the cement paste: of

4 GPa to 5 GPa for the most compliant phase and 2 GPa to 5 GPa for the stiffest phase (P3 excluded).

A larger decrease of the phases' elastic properties is encountered in P2-0.2, compared to that in P1-0.2. Indeed, polymers P1 and P2 have the same chemical composition, but are produced by different companies and delivered in different states (powder and suspension). They also have different MFFT (Table 6.1), which influences the microstructure of the PMC paste. As the MFFT is dependent of the polymer glass transition temperature [143], P1 is expected to have a lower glass transition temperature and be stiffer than P2. This was confirmed by the measurement of the polymer complex modulus in Section 6.2.2. Thus, the lower modulus values in P2-0.2 compared to those in P1-0.2 can be explained by the different polymers having a greater influence on the material than at low polymer content.

The sample P3-0.2 apparently behaves differently, as the modulus of its phase 1 is lower and has a higher standard deviation (14.6 ± 8.0 GPa) than those of the other samples. Also, its phase fractions are higher for phase 1 and lower for phase 2, with 84 % and 14 %, respectively. This can be caused by the high pore concentration in the P3-0.2 sample (see Section 6.2.1). The porosity decreased the number of successful indents and, thus, the quality of the SNT results. It also decreased the overall sample stiffness as well as the stiffness of phase 1, compared to those of the other samples.

To summarize, the compliance of the PMC samples is increased by the larger P:C ratio of 20 %, which can be explained by the lower modulus of the polymers compared to that of a cement paste. From a mechanical point of view, a P:C of 5 % of the polymers P1 and P2 provides similar phases' modulus than those of the reference sample. Thus, this P:C ratio might be the most adequate polymer content for PMCs. However, for the selection of PMCs and the P:C ratio, also the durability and long-term performance of these cement pastes should be considered.

6.3.4 Aging of the phases

The phases of each PMC elastic modulus distribution at the ages of 28 and 56 days are compared in Figure 6.8b. For all samples, except P3-0.2, the mean modulus of both phases are nearer to each other on day 56 than on day 28, which indicates a reduction of the modulus scatter with the sample age, and more homogeneous material properties. This might be due to an ongoing chemical reaction leading to a more homogeneous degree of hydration of the cement paste over the sample surface at greater ages and/or a more homogeneous polymerization.

The largest differences between the phases on days 28 and 56 are observed in P3-0.2: the mean modulus of both phases increases by up to 4 GPa within the second month of the sample. This may be related to the high porosity being reduced with age because of the ongoing chemical reactions in the sample. The sample being tested in a less porous location on day 56 than on day 28 could be another reason.

To conclude, the hydration reaction of the PMCs seems to be delayed by the polymer modification, as already noted e.g. by [144, 145]. However, the age of a PMC has less influence on the properties of its phases than the polymer type and the polymer content.

6.3.5 Evaluation of analysis procedures

The phases from different fit procedures were compared for both P1-0.2 and the reference sample.

For P1-0.2, the fits from LM procedure (Section A.1.1) with two phases (LM 2 ph.) were compared to the fits from EM procedure (Section A.1.4) with two and three phases (EM 2 ph. and EM 3 ph., Table 6.5).

The phases from LM 2 ph. and the two most compliant phases EM 3 ph. show similar properties, in particular on day 28. For example, they have $<0.5\,\%$ difference on the mean modulus of phase 1, and $<4.5\,\%$ for phase 2. Also, their fraction of phase 1 differ by $<3\,\%$. On day 56, the differences

are higher, up to 10 % for the mean value of phase 2 and 38 % for its phase fraction.

The phases of EM 2 ph. show larger differences at both ages with the two most compliant phases of both LM 2 ph. and EM 3 ph. In particular, the phase fractions of LM 2 ph. and EM 2 ph. differ of more than 40 % and 69 % for phase 1 and 2, respectively. Indeed, in EM fitting procedure, the sum of all phase fractions must be equal to one, and smaller or equal to one in the LM fitting procedure. This condition of the EM procedure forces the measurement outliers to be modeled as a phase of the modulus distribution with large standard deviation and small amplitude, like the stiffest phase in the EM 3 ph.: phase fraction less than 10 %, ratio of the phases standard deviation and mean value larger than 58 %. This particularity of the EM procedure was already observed and discussed for the reference sample in Section 6.3.1.

For the reference sample, the results from the LM procedure with two (LM 2 ph.) and three phases (LM 3 ph.) are compared to those from the EM procedure with three (EM 3 ph.) and four phases (EM 4 ph.), respectively (Table 6.6). The stiffest phase of each fit with the EM procedure was added for information, but is not discussed in the following, following the arguments presented in Section 6.3.1.

The phases from LM 2 ph. and the two most compliant phases from EM 3 ph. show similar mean values and standard deviations at both ages, with less than 10 % difference for the mean values and 13 % for the standard deviations. Also the phase fractions do not differ by more than 6 % on day 28. Moreover, the phases from LM 3 ph. and the three most compliant phases from EM 4 ph. also show less than 9 % and 13 % difference in mean values and standard deviations, respectively.

Thus, it can be concluded that, as for the other investigated materials, the fitting procedure has a large influence on the determination of the number of phases, which then influences the determination of the phase properties. For

Table 6.5: Fit results comparison between LM and EM procedure in P1-0.2.

		On day 28		On day 56	
Procedure	Phase	Modulus (GPa)	Phase fraction (%)	Modulus (GPa)	Phase fraction (%)
LM with 2 phases	1	19.3 ± 5.6	52.7	19.2 ± 5.4	51.5
	2	34.6 ± 14.0	43.8	31.1 ± 14.0	46.9
EM with 2 phases	1	21.8 ± 7.7	74.2	20.4 ± 7.0	69.8
	2	49.2 ± 23.0	25.8	39.0 ± 19.0	30.2
EM with 3 phases	1	19.3 ± 5.8	54.1	19.3 ± 6.4	62.5
	2	33.2 ± 12.0	36.4	34.2 ± 13.0	34.0
	3	67.0 ± 26.0	9.4	64.8 ± 27.0	3.5

Table 6.6: Fit results comparison between LM and EM procedure in the reference sample.

		On day 28		On day 56	
Procedure	Phase	Modulus (GPa)	Phase fraction (%)	Modulus (GPa)	Phase fraction (%)
LM with 2 phases	1	23.0 ± 5.3	49.3	22.9 ± 5.5	54.2
	2	37.1 ± 14.0	46.7	35.6 ± 14.0	44.0
LM with 3 phases	1	22.0 ± 4.3	36.0	22.2 ± 4.3	28.6
	2	30.9 ± 9.1	39.6	25.9 ± 8.4	40.7
	3	48.1 ± 24.0	23.0	40.3 ± 17.0	30.2
EM with 3 phases	1	23.1 ± 5.2	47.8	23.5 ± 6.3	63.2
	2	35.5 ± 14.0	44.3	38.8 ± 15.0	35.0
	3	82.9 ± 35.0	8.0	69.1 ± 31.0	1.8
EM with 4 phases	1	22.1 ± 3.8	27.5	22.4 ± 4.2	31.1
	2	28.4 ± 9.8	53.7	26.5 ± 9.5	47.0
	3	51.9 ± 14.0	14.1	45.6 ± 16.0	21.3
	4	101 ± 32	4.7	90.0 ± 36.0	0.6

equivalent numbers of phases (i.e. one more in the fit from EM than in the fit from LM), both procedures provide rather similar results.

6.4 Summary

6.4.1 Microstructure and aging of PMC pastes

The use of statistical methods to analyze nanoindentation data enabled a precise characterization of each PMC paste, which highlighted the influence of the polymer type, the polymer content and the age of the paste on the PMC modulus distribution. The study showed that the polymer-modification decreases the stiffness of the cement pastes, an effect that increases with the polymer content and the polymer compliance. The study also highlighted the retardant effect of the polymer modification on the material hardening reaction time, in particular with the polymers P2 and P3. This effect was found to get stronger with increasing polymer content.
As for mortar and cement pastes, the nanoindentation results of PMC was shown to largely depend of the surface quality and the sample porosity. This highlights the importance of a careful sample preparation in the nanoindentation measurements. With the surface preparation method used in this study, the microstructure of PMC pastes was found to be composed of one compliant phase and one stiff phase. The compliant phase is believed to be composed of the hydrated cement paste mixed with the polymer, whereas the stiff phase is mostly composed of unhydrated cement particles and their neighboring material.

6.4.2 Applicability of the SNT

A statistical analysis of nanoindentation results was successfully applied to PMC pastes. The LM analysis procedure (see Section A.1.1), though less automatized than the EM procedure (see Section A.1.4), provides the physically most meaningful results. In the EM procedure, the stiffest phase did

not match any phases from the LM analysis procedure (see Section 6.3.5). The other phases of the distributions, however, showed only few differences with each other.

The indentation depth was found to be a very important parameter for the usefulness of nanoindentation experiments. It must be chosen as a compromise between the accuracy of the phases' properties and a low influence of the surface roughness. The polymer mechanical properties modifying the investigated PMC pastes were measured by nanoindentation and used as input parameters in a semi-analytical multiscale model of polymer-modified concretes [141]. The model showed good agreements with the experimental results.

7 Conclusions and Outlook

Heterogeneous materials of various classes were investigated with nanoindentation: bi-metal composites, a plant attachment pad, and various kinds of polymer-cement paste compounds. The materials were analyzed using variations of the Statistical Nanoindentation Technique (SNT). The SNT was shown to be universally applicable for the investigation of heterogeneous materials.

In both the bi-metal composites and the plant attachment pad, the microscopically heterogeneous microstructure of the materials was successfully investigated with SNT, and its understanding enabled to study the interaction between the various mechanical phases. Associating the SNT with microscopical imaging, the mechanical phases in the bi-metal composites and the plant attachment pad have even been assigned to a material phase. For the polymer-cement compounds, the SNT has also been successfully applied, but identifying the mechanical phases is still a challenge, as their expected characteristic sizes are small compared to the nanoindentation spatial resolution, and, thus, require a very low surface roughness that is difficult to achieve.

For a successful SNT analysis, some guidelines are proposed. Regarding the nanoindentation, the experiments must be designed under consideration of the requirements of the statistical analysis method and with the overall goal of determining the phase's properties. In particular, the choice of the indentation depth is challenging, as it has to be large enough to overcome the surface roughness and at the same time be small enough compared to the expected characteristic sizes of the mechanical phases. A smaller indentation depth also contributes to the statistical accuracy by enabling to increase the

number of tested locations. Regarding the statistical analysis of the empirical distribution, it was shown that different fitting algorithms can provide accurate, yet different, fit results. Attention must be given, however, to the constraints on the phase fractions, which notably influenced the determination of the number of phases and, consequently, the phase properties. Coupling the SNT with microscopy techniques might help understanding the phases as determined from the SNT and choose the results from the best fitting algorithm.

Recommended goodness-of-fit criteria are the BIC, the χ^2 and the r_a^2, depending on the fitting algorithm. They can help in the determination of the optimal number of phases and the optimal phase properties. Additionally to the goodness-of-fit criteria, however, the plausibility of the phases from the deconvolution must also be critically considered. This can be achieved for example with a parameter study of the SNT, or by analyzing the soft clustering distributions of the empirical data compared to those of the phases properties.

Also, the studies presented here would benefit to be reproduced with improved sample preparation, in particular for the polymer-modified cement pastes and the mortar samples. This would enable to reduce the indentation depth of these samples and, thus, to investigate the material phases more accurately. Furthermore, the SNT analysis could be developed for the investigation of the creep and viscoelastic deformation behavior of individual phases of heterogeneous materials, especially for cement-based materials. Finally, the SNT could also be used to investigate the microstructure of plant tissues in order to facilitate bio-mimicry or the development of new, bio-inspired materials.

A Statistical Nanoindentation Techniques

Different fitting procedures can be applied to determine the mechanical properties from nanoindentation of heterogeneous materials via SNT. In this chapter, the influence of the presence of experimental noise, the choice of the fitting algorithm, or the experimental distribution, and the influence of fitting constraints are discussed. The analysis presented is based on nanoindentation experiments of polymer-reinforced cement pastes (see also Section 6). In the following, three fitting procedures are described, and compared. Then, relevant fitting parameters are identified and discussed, and some guidelines for an optimum statistical analysis for nanoindentation data are proposed.

A.1 Fitting procedures

A.1.1 Levenberg-Marquardt fitting algorithm

A Levenberg-Marquardt (LM) algorithm, implemented in the *Peak Fit Analyzer* module of Origin (OriginPro 2016, OriginLab Corporation, Northampton, MA, USA) was used. It derives from a least square minimization algorithm, and details on the LM fitting algorithm are presented in [146–148]. The objective function to be minimized is: $\sum_{j=1}^{n} \delta_{CDF_{X_j}}^2$ with $\delta_{CDF_{X_j}}$ the residual at the j-th point of the empirical distribution, i.e. the distance in the y-direction only between the j-th point of the empirical distribution, of coordinates (X_j, CDF_{X_j}), and the fitting curve $CDF_{fit}(x)$. The end-of-fit criterion is based on the calculation of the χ^2 with a tolerance of minimum 10^{-6}.

Successive sets of starting parameters were chosen in the range of higher density of empirical data. The best fit was chosen as the most reproducible fit that converged with different sets of starting parameters. Several fits were performed for each empirical distribution. The number of iterations allowed until convergence was achieved, and the sum of all phase fractions was constrained to be less or equal to one. Fits with different numbers of phases were compared based on their goodness-of-fit criteria, such as χ^2 and r_a^2.

A.1.2 Verification of the accuracy of the LM fitting procedure

For a first verification of the accuracy of the LM fitting procedure, a two-phase distribution was generated, fitted using the LM procedure as described in the previous paragraph, and then the parameters of the generated and fitting functions are compared and discussed.

Figure A.1a presents the CDF plot of 500 data points generated as a mixture of two Gaussian distributions, whose parameters are listed in Table A.1. The artificial distribution was generated for the purpose of this investigation[1]. First the function parameters were generated, such as

$$
\begin{aligned}
A_1 &= 0.5\,\mathrm{rand}() + 0.2 \\
A_2 &= 1 - A_1 \\
m_1 &= 80\,\mathrm{rand}() + 20 \\
m_2 &= 100\,\mathrm{rand}() \\
s_1 &= \frac{m_1}{2}\,\mathrm{rand}() \\
s_2 &= m_2\,\mathrm{rand}()
\end{aligned}
$$

[1] Microsoft Excel as OLE (Object Linking and Embedding), embedded in Origin

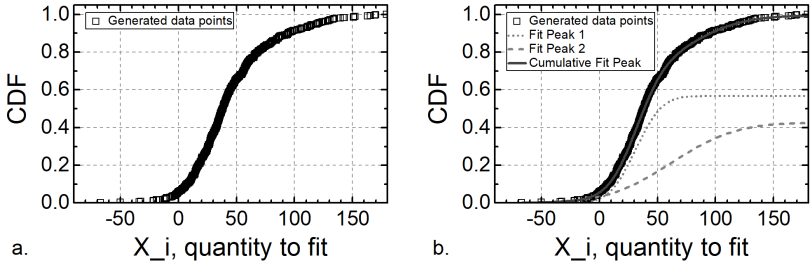

Figure A.1: (a) CDF plot of a generated distribution of two Gaussian phases with 500 data points. (b) Optimal deconvolution with two Gaussian phases of the same distribution, obtained from LM fitting algorithm. The distribution and fitting parameters are in Table A.1.

rand() is the pseudo-random equally distributed number generator, with output being larger or equal to zero and smaller than one[2]. The parameters of the two phases were chosen in such way that the phases have different amplitudes, standard deviations and mean values.

Then, the $500A_1$ points of the distribution associated to the phase 1 were generated such as

$$X_1 = \left[\cos\left(2\pi\,\mathrm{rand}()\right)\sqrt{\left(-2\ln\left(\mathrm{rand}()+10^{-14}\right)\right)}\right]s_1 + m_1$$

This equation transforms a uniform distribution between zero and one to a normal distribution of standard deviation s_1 and mean value m_1 and is called Box-Müller transform [149], whereas a constant term of 10^{-14} was added to the random number in the logarithm to avoid it assuming a value of zero. The constant was chosen as the smallest number provided by Excel with exact precision[3]. The points from the phase 2 were generated in a similar way, using the function parameters previously generated.

[2] `https://support.office.com/en-us/article/RAND-function-4cbfa695-8869-4788-8d90-021ea9f5be73`, visited on 7th September 2018

[3] `https://en.wikipedia.org/wiki/Numeric_precision_in_Microsoft_Excel`, visited on 7th September 2018

Table A.1: Parameters of a generated two-phase Gaussian distribution with 500 points, and of the optimum two-phase fitting function plotted in Figure A.1b

	Mean value	Standard deviation	Phase Fraction (%)
Phase 1			
Generated	17.59	30.93	60.2
Fit	17.7	31.2	56.7
Phase 2			
Generated	46.73	68.94	39.8
Fit	43.6	61.8	42.6

Figure A.1b presents the optimum fitting function, as calculated by the LM fitting algorithm. The function is a sum of two Gaussians (Table A.1).
The LM fitting algorithm provided a good estimation of the distribution parameters (Table A.1), in particular for the phase with the highest phase fraction (phase 1). The differences between the generated and the fitted parameters may come from an insufficient number of high values in the phase 2 of the generated distribution. This has the consequence that the whole generated distribution had a lower amplitude of values, and in particular the phase 2 of the fitting function was shifted towards lower values, which increased the overlap of the two phases. A larger number of generated data points might have helped getting enough data points over the whole generated distribution and, thus, might have improved the parameters estimation from the deconvolution analysis.

A.1.3 Orthogonal Distance Regression fitting algorithm

An alternative to the Least-Square Estimation fit is the Orthogonal Distance Regression algorithm (ODR)[4]. Compared to the LM algorithm, the ODR algorithm minimizes the orthogonal distance between the empirical

[4] implemented in the *Non-linear Curve Fit* module of Origin

data and the fitting curve [150]. The objective function to be minimized is then: $\sum_{j=1}^{n}(\delta_{X_j}^2 + \delta_{CDF_{X_j}}^2)$, with δ_{X_j} and $\delta_{CDF_{X_j}}$ the residuals at the point (X_j, CDF_{X_j}), i.e. the distance in x and y directions between each point (X_j, CDF_{X_j}) of the empirical distribution and the fitting curve $CDF_{fit}(x)$. The iteration algorithm itself is still a Levenberg-Marquardt algorithm [150, 151].

The end-of-fit criterion here is based solely on the calculation of the χ^2 with a tolerance of maximum 10^{-6}. The starting parameters of the fitting function were chosen in the range of higher empirical data density. The best fit was chosen as the most reproducible one, given different sets of starting parameters. Several fits were done for each empirical distribution and the number of iterations was not constrained. As in the LM fitting procedure, the sum of the phase fractions was constrained to be less or equal to one.

An advantage of this fitting algorithm is the possibility to investigate the effect of uncertainty of the measured quantity on the fitting results (X error input). A drawback of the fitting algorithm is that the number of phases is fixed from the first step of the analysis on, which complicates the investigations about the number of necessary and relevant phases in the empirical distribution.

A.1.4 Expectation-Maximization fitting algorithm

Implemented in Matlab[5], the Expectation-Maximization (EM) procedure maximizes the likelihood of the fitting function instead of the distance between the empirical data set and the fitting function. Also, the EM fitting algorithm is used [152] instead of the LM fitting algorithm. The advantage of the EM algorithm is that it also can be used to cluster the empirical data. Indeed, the algorithm "assigns posterior probabilities to each component density with respect to each observation" [153]. Clustering of the empiri-

[5] Matlab R2016a, The MathWorks Inc., Natick, MA

cal data is investigated in the following as potential way of determining the number of mechanical phases in the material.
The termination tolerance for the log-likelihood function was set to 10^{-6}. 100 and 50 independent fits for modulus and hardness, respectively, were done for each empirical data set and fitting function. For each fit, a random set of starting parameters was generated. The maximum number of iterations was restricted to 2000 and 1000 for modulus and hardness respectively. In this procedure, the sum of all phase fractions was equal to one. The consequences of this constraint will be investigated in the following. Despite the high number of independent fits, the duration of the whole fitting procedure is in the range of a minute for each fitting function and empirical data set. For a set of empirical data, fits with a various number of phases were compared, taking advantage of the short duration of the fit itself.
In the following, the accuracy of the ODR and EM fitting will be discussed and compared to that of the LM fitting procedure.

A.2 Identification of relevant parameters

A.2.1 Experimental noise

Determination of experimental noise To investigate the importance of the experimental noise in SNT, the noise of nanoindentation experiments was estimated on two sample materials. First, two grid fields of 670 indents each, with a distance of at least 20 µm between two indents, were made on fused quartz with the ET method using a Berkovich tip to a depth of 1 µm. The material is used as reference material for the calibration of nanoindentation experiments. The parameters β, ε and Poisson's ratio ν were set to 1, 0.75 and 0.188, respectively [67], whereas a β value of 1.05 would have been more suitable, considering the pyramidal tip used (see Section 2.2.1). The experimental noise was determined as one standard deviation of the elastic modulus. The mean value was 74 GPa and one standard deviation 0.63 GPa.

An aluminum sample was ground and polished manually with diamond suspensions with different grain sizes down to 0.1 µm. 22 indents were made with a Berkovich tip using the CSM method at a loading rate of $2\,\mathrm{mN\,s^{-1}}$ to a maximum load of 600 mN. Poisson's ratio was assumed as 0.33, and the calculation parameters β and ε were set to 1.05 and 0.75. The elastic modulus was averaged over a loading segment between 100 mN and 200 mN, corresponding to a depth range from 1600 nm to 2400 nm. The mean modulus was 93.2 GPa and one standard deviation was 1.88 GPa.

Fitting with uncertainty on experimental values A polymer-modified cement sample with 0.5-W:C (water to cement) ratio and 0.05-P:C ratio was prepared[6] and investigated with nanoindentation. 3251 indents were made with ET to a depth of 1 µm. The ODR fitting procedure (see Section A.1.3) was used on a CDF representation of the empirical modulus distribution to investigate the influence of the experimental uncertainty on the deconvolution results. The starting parameters were the same for each fit, chosen such that the initial phase distribution is regularly distributed over the range of the empirical distribution, with equal standard deviations and phase fractions for all phases.

In this fit, an uncertainty factor w was considered for each experimental data point j during the fitting procedure. Thus, instead of minimizing the function $\sum_{j=1}^{n}(\delta_{X_j}^2 + \delta_{CDF_{X_j}}^2)$ as in the standard ODR procedure, the function $\sum_{j=1}^{n}(w\,\delta_{X_j}^2 + \delta_{CDF_{X_j}}^2)$ was minimized, with δ_{X_j} and $\delta_{CDF_{X_j}}$ the distance between the j-th point of the empirical distribution and the fitting curve in direction of the modulus axis and of the CDF axis, respectively. Through the addition of this factor w, the influence of δ_{X_j} on the fitting curve is reduced, compared to that of $\delta_{CDF_{X_j}}$.

The factor w was chosen as constant for all points of the empirical distribution and equal to $\frac{1}{\Delta^2}$, with Δ is the experimental error measured on the refer-

[6] Provided by Luise Göbel, Bauhaus University, Weimar, Germany

ence material quartz as described above. In a second step, Δ was increased to 5 GPa to investigate the effects of a potentially higher experimental uncertainty. A fitting function with both two and three phases was used for each value of the experimental noise.

A.2.2 Fit from PDF distribution representation versus CDF distribution representation

The influence of the empirical data representation was investigated by comparing the fitting results of the polymer-modified cement sample from both a PDF and a CDF representation. The bin size for the PDF representation was chosen as twice the standard deviation measured experimentally with high speed indentation on quartz, i.e. 1.25 GPa (see Section A.2.1). The number of phases of the fitting function was set to three for both representations. The LM fitting procedure was used for the PDF representation and the ODR procedure for the CDF representation. The same initial parameters were used for both fits, when applicable, and a χ^2 tolerance of 10^{-9}. The mean values and the standard deviations from both fits can be directly compared. However, the surface fraction of the phases fitted from the PDF representation are not directly given by the algorithm. Hence, the relative surface fraction of the phase i, f_i was calculated from the fraction of the area under the $i-th$ curve A_i, as $f_i = \frac{A_i}{\sum_{j=1}^{3} A_j}$.

A.2.3 Fitting procedure

The modulus empirical CDF of the polymer-modified cement sample described in the uncertainty paragraph of A.2.1 was used to investigate the effect of the fitting algorithm on the deconvolution results. First, both ODR and LM fitting procedures were used with the same starting parameters. The parameters were chosen such that the initial phases are regularly distributed over the range of the empirical distribution, with equal standard deviations and phase fractions. The best fits for each fitting algorithm and with a sum

of two and three phases were compared to each other. No experimental noise was added to the empirical distribution. Then, the results from LM and EM fitting procedures with a various number of phases were compared. In the EM fitting procedure, the fit with the largest log-likelihood[7] is compared to the fits from the other procedures. Indeed, a larger log-likelihood also means a lower BIC[8], and a better fit.

A.2.4 Comparison criteria between fit results to find best fit

The modulus empirical CDF of the polymer-modified sample described in the uncertainty paragraph of A.2.1 was used to investigate the best goodness-of-fit criterion to determine the number of mechanically homogeneous phases in the material. The modulus distribution was investigated with the ODR procedure and two to three phases. First, the goodness-of-fit criteria reduced χ^2 and the adjusted coefficient of determination r_a^2 were compared. Additionally, the AIC and BIC[9] of both models were calculated using the *Rank model* feature provided in Origin[10]. There, the ODR fitting procedure is also used to find the best fitting parameters considering the proposed function. But in this tool, the fits cannot be controlled by the user, neither the initial parameters nor the fitting algorithm used. Both fits converged with a χ^2 tolerance of 1×10^{-9}. Finally, the relative likelihood of the model 2 compared to that of the model 1 were calculated based on their respective AIC: AIC_2 for model 2 and AIC_1 for model 1. The relative likelihood of model 2 is expressed as $\exp\left(\frac{AIC_1 - AIC_2}{2}\right)$. The consistency and accuracy of each criterion were compared based on the different numbers of phases investigated.

[7] `https://de.mathworks.com/help/stats/fitgmdist.html`, visited on 4th May 2018.
[8] `https://de.mathworks.com/help/stats/gmdistribution.bic.html`, visited on 4th May 2018.
[9] `https://www.originlab.com/doc/Origin-Help/PostFit-CompareFitFunc`, visited on 4th May 2018.
[10] OriginPro 2016, OriginLab Corporation, Northampton, MA, USA

A.2.5 Clustering as a tool to estimate the number of mechanical phases

A second sample, a polished cement paste without polymer modification at age of 28 days, was tested with high-speed indentation at age of 28 days, and its modulus EDF was fitted with the EM procedure. Fitting functions with two to five phases were used.

The EM procedure was chosen for this investigation as it allows both the clustering of each data point into one of the phases, i.e. a hard clustering, and soft clustering. Hard clustering is based on the phase with highest posterior probability for the concerned data point. In soft clustering, the posterior probability is used to compare the probabilities of each phase knowing all phases and for a given data point. These tools were used to better investigate the modulus distribution with a various number of phases and thus better estimate the number of mechanical phases in a material at microscopic scale.

A.3 Parameter evaluation

A.3.1 Experimental noise

The modulus distribution of the investigated polymer-modified cement paste sample was fitted with and without experimental error, and the modulus phases were compared for two different numbers of phases (Table A.2). The difference in the mean modulus values was less than 0.01 GPa for each phase of both fitting functions. Also the standard deviation difference was less than 0.05 GPa and the surface fraction difference was less than 0.2 %. For the higher noise of 5 GPa, the differences between the deconvolution results increase to reach less than 0.03 GPa for the mean modulus, 0.1 GPa for the standard deviation and 0.2 % for the surface fraction in each phase. Thus a constant noise over the whole experimental distribution does not largely impact the deconvolution results, even for very noisy experiments.

Table A.2: Influence of the uncertainty on modulus determination on fitting results as function of the number of phases in the fitting function and the amplitude of the uncertainty.

Fit parameter	No noise		Experimental noise		High noise	
	2 phases	3 phases	2 phases	3 phases	2 phases	3 phases
Phase 1						
Mean modulus (GPa)	17.2	14.611	17.2	14.619	17.2	14.633
St. deviation (GPa)	4.7	2.70	4.7	2.74	4.7	2.80
Phase fraction (%)	65.5	14.7	65.5	14.75	65.5	14.9
Phase 2						
Mean modulus (GPa)	30.6	18.7	30.6	18.7	30.6	18.7
St. deviation (GPa)	10.7	4.9	10.7	4.9	10.7	4.9
Phase fraction (%)	32	51	32	51	32	51
Phase 3						
Mean modulus (GPa)		30.3		30.3		30.3
St. deviation (GPa)		13.1		13.1		13.1
Phase fraction (%)		32.5		32.5		32.4

A.3.2 Distribution representation

A modulus distribution was fitted with the same fitting function from both a PDF and a CDF representation (Figure A.2). Table A.3 summarizes the main phase properties for each fit. All phases show little differences between the fits from PDF and CDF representations regarding their mean values and standard deviations. However, the phase fraction from PDF may vary up to 4 % compared to that from CDF.

The reduced χ^2 of the fits was 2.5×10^{-6} for the fit from the PDF and 8.2×10^{-6} for the fit from the CDF. This indicates that the fit from the PDF representation is nearer to the empirical data than the fit from the CDF representation.

The adjusted coefficient of determination r_a^2, however, was 0.992 for the PDF representation, and 0.9999 for the CDF representation. This indicates that the fit from the CDF representation more accurately fits the empirical curve than the fit from the PDF representation. Thus, no clear conclusion on the best distribution representation can be drawn from the analysis of the fit parameters χ^2 and r_a^2 only.

The advantage of the PDF representation is that the most important peak in relative phase fraction is also the peak exhibiting the highest relative frequency (Figure A.2a). Thus, it is easier to infer its location and properties, compared to for the other peaks of the distribution. This corresponds to the main drawback of the CDF representation that the phases are nearly impossible to infer (Figure A.2b).

However, the PDF representation requires a binning step (see Section 2.2.5), which parameter is chosen during the analysis and influences its results. The use CDF representation does not have this binning step, and thus, prevents potential issues linked to the choice of this parameter to occur.

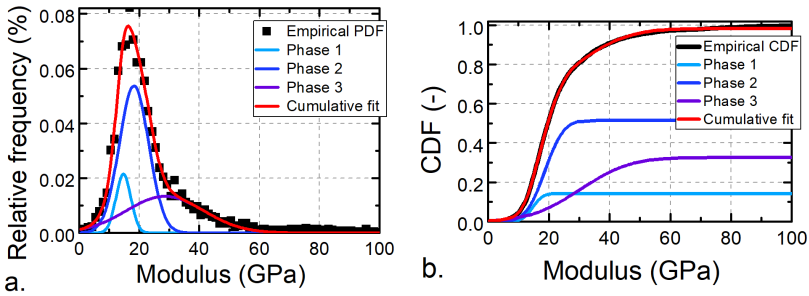

Figure A.2: Three-phase fit of a modulus distribution from a polymer-modified cement paste represented with (a) PDF and (b) CDF plots.

Table A.3: Fitting results for the same modulus data set fitted by a sum of three Gaussian functions, from either a PDF or a CDF representation

Property	Data representation	
	PDF	CDF
Phase 1		
Mean modulus (GPa)	14.7	14.6
St. deviation (GPa)	2.5	2.7
(Rel.) Phase fraction (%)	10.8	14.7
Phase 2		
Mean modulus (GPa)	18.3	18.7
St. deviation (GPa)	4.9	4.9
(Rel.) Phase fraction (%)	53.9	51.0
Phase 3		
Mean modulus (GPa)	28.6	30.3
St. deviation (GPa)	12.9	13.1
(Rel.) Phase fraction (%)	35.3	32.5

A.3.3 Fitting procedure

First, the same data as in the previous section were fitted with the ODR and the LM fitting algorithms (Table A.4). No significant differences in the mean values, standard deviations or phase fractions between the phases of a two-phase distribution from ODR and LM were found. In the case of a three-phase distribution, the phase fractions of phase 1 and 2 have a difference of less than 0.4 % (in absolute variation) between the two fitting algorithms. Thus, the results differences between the ODR and LM fitting procedures are considered negligible compared to those between optimal fits with different numbers of phases.

The modulus distribution from the same polymer-modified cement sample (see Table A.4) was also fitted with the EM fitting algorithm. The phases' properties and the BIC of the optimum fit for a number of phases between two and four are summarized in Table A.5.

At the same number of phases, large differences in the fit results are found when comparing the EM fit results with the LM fit results. For example, comparing the fit results from LM with two phases and EM with two phases, the differences in the mean values are as large as 1 GPa and 8 GPa for the most compliant and the stiffest phase, respectively. Also, the phase fractions show differences as large as 11 % (in absolute variation). Similar observations can be made while comparing the fit results from LM and EM with three phases.

However, comparing the fit results from LM two phases with EM three phases, the two most compliant phases present many similarities with each other (Figure A.3). For example, the absolute variation of their mean value and standard deviation is below 0.8 GPa and the absolute difference in the phase fraction of the most compliant phase is less than 1 %. Indeed, the major difference in the results from both fitting procedures is the presence in the EM fit results of the third phase.

Table A.4: Influence of fitting algorithm, Levenberg-Marquardt (LM) and Orthogonal-Distance Regression (ODR), on the deconvolution of an empirical modulus distribution from a polymer-modified cement paste.

Fitting algorithm	LM		ODR	
	2 phases	3 phases	2 phases	3 phases
Phase 1				
Mean modulus (GPa)	17.2	14.6	17.2	14.6
St. deviation (GPa)	4.7	2.7	4.7	2.7
Surface fraction (%)	65.5	14.2	65.5	14.7
Phase 2				
Mean modulus (GPa)	30.6	18.7	30.6	18.7
St. deviation (GPa)	10.7	4.9	10.7	4.9
Surface fraction (%)	32.0	51.4	32.0	51.0
Phase 3				
Mean modulus (GPa)		30.3		30.3
St. deviation (GPa)		13.1		13.1
Surface fraction (%)		32.6		32.5

Compared to the other phases of the EM fit with three phases, this third phase has a low surface fraction (less than 10 %), a high mean value, and a standard deviation larger than one-third of its mean value. This third phase is thus considered as a consequence of the constraint on the sum of all phase fractions in the EM fitting procedure. Such a phase actually describes the outliers with high modulus or hardness values from the empirical distribution.

These outliers are difficult to catch in a single phase, as they do not represent a large percentage of the whole distribution and, per definition, exhibit a large scattering. This leads to a phase with a high standard deviation and low fraction in the fit. In the following, the third phase as described in the previous paragraph is not considered as a physical part of the material properties deconvolution, but as a by-product of the fitting procedure.

The EM fit results with four phases present a similarly *unphysical* fourth phase (Table A.5 and Figure A.3). But even without considering this fourth phase, the results from the EM four-phase fit cannot be so easily compared to other fit results, independent of the fitting procedure. Indeed, the phase distribution is quite different from all other investigated distributions: large differences in mean values, standard deviations and phase fractions are observed.

Table A.5: Influence of fitting algorithm, LM or EM, on the deconvolution of an empirical modulus distribution from a polymer-modified cement paste. BIC of EM fits: 24182 (2 phases), 23957 (3 phases) and 23972 (4 phases).

Fitting algorithm	LM		EM		
	2 phases	3 phases	2 phases	3 phases	4 phases
Phase 1					
Mean modulus (GPa)	17.2	14.6	18.3	17.3	16.8
St. deviation (GPa)	4.7	2.7	5.5	4.8	4.4
Phase fraction (%)	65.5	14.2	76.1	66.4	53.6
Phase 2					
Mean modulus (GPa)	30.6	18.7	38.9	29.8	22.5
St. deviation (GPa)	10.7	4.9	19.0	10.2	7.7
Phase fraction (%)	32.0	51.4	23.9	27.8	26.8
Phase 3					
Mean modulus (GPa)		30.3		59.3	35.2
St. deviation (GPa)		13.1		23.0	11.0
Phase fraction (%)		32.6		5.8	15.7
Phase 4					
Mean modulus (GPa)					67.2
St. deviation (GPa)					21.6
Phase fraction (%)					4.0

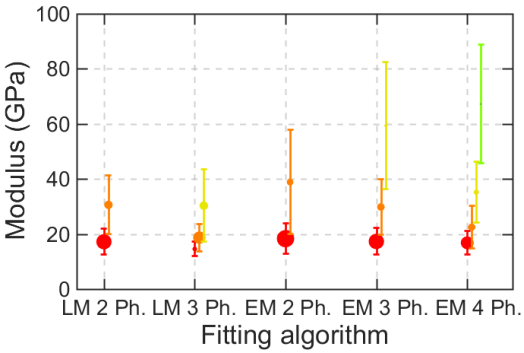

Figure A.3: Deconvolution of an empirical modulus distribution from a polymer-modified cement paste with two to four phases and using both the LM and EM fitting algorithms. Each point represents a phase mean value, with the error bar as standard deviation. The point size is proportional to the phase fraction. The colors indicate a phase number, ordered by increasing mean value.

A.3.4 Comparison criteria between fit results to find best fit

Table A.6 summarizes the values of various goodness-of-fit criteria for the same modulus distribution of the polymer-modified cement paste. The modulus distribution was fitted using the ODR procedure with two and three phases. The two fits are compared in Figure A.4. Whereas the models for both numbers of phases seem to describe well the curve at lower modulus values, the cumulative fit curve is nearer to the empirical curve in the three-phase case than in the two-phase case. This holds in particular around 50 GPa and at moduli greater than 80 GPa. Furthermore, all the criteria indicate that the three-phase model is the best model for this empirical curve: the three-phase model exhibits a lower reduced-χ^2, a slightly higher r_a^2 and a lower AIC and BIC than the two-phase model. Also, the relative likelihood of the two-phase with respect to the three-phase model is equal to zero. However, a fit with four phases was not investigated, thus it is found that the

Table A.6: Goodness-of-fit parameters for the same modulus distribution of a polymer-modified cement paste, fitted with the same procedure, but either two or three phases. The three-phase function gives better values than the two-phase function for all criteria.

Number of phases	reduced χ^2	r_a^2	AIC	BIC
2	2.8×10^{-5}	0.9997	−34060	−34011
3	8.2×10^{-6}	0.9999	−38074	−38007

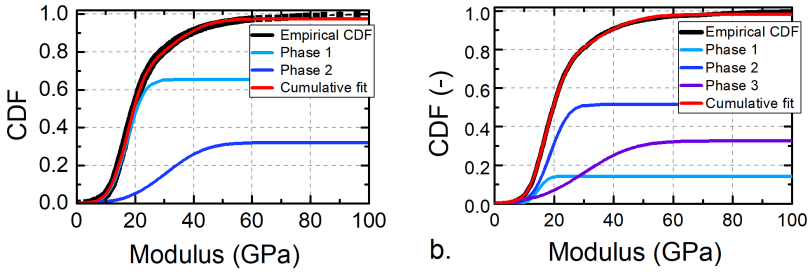

Figure A.4: (a) Two-phase and (b) three-phase fit of a modulus CDF from a polymer-modified cement paste

polymer-modified cement paste studied here presents at least three phases with different elastic moduli.

Having a deeper look at the comparison criteria for the two-phase and three-phase fits, the largest differences between the two models is found for the AIC and the BIC, as well as the relative likelihood. The relative likelihood is also the most explicit and the best comparison criterion, as it represents the probability of a given model with respect to another one.

A.3.5 Clustering

Hard clustering consists in assigning a cluster, i.e. a most probable phase, to each data point of an investigated distribution. The cluster of each location of a hardened cement paste is plotted as function of its modulus measured by nanoindentation in Figure A.5. Additionally, the posterior probability

of each phase of the cement paste is plotted as function of the measured modulus range, which is called soft clustering (Figure A.6).

The hard clustering of the distribution with two phases shows that there are at least two well defined phases in the material. Indeed, all locations with modulus greater than 46.6 GPa are clustered into the cluster 2, corresponding to phase 2, all data points with modulus between 0.6 GPa and 46.6 GPa into the cluster 1, corresponding to phase 2 and only one data point with modulus value below 0.6 GPa is clustered into the cluster 2. This one data point might be considered as an outlier for the distribution, due to its very low modulus value, and its cluster.

In the distribution with five phases, the indents with modulus above 125 GPa are hard-clustered into the phase 5. This represents 24 of 2054 indents, or 1.2 % of the modulus distribution. The physical relevance of this phase should thus be further investigated.

In the distributions with three to five phases, the assigned cluster increases with the modulus of the investigated data point. Exceptions are the locations with the lowest modulus values: the locations with modulus up to 11 GPa in the three-phase distribution, 16.75 GPa in the four-phase distribution and 17.54 GPa in the five-phase distribution are clustered into the cluster 2. The cluster 1 comes next, followed by cluster 2 again. Thus, the two most compliant phases actually overlap significantly at the lowest modulus values, and the phase 1 is "surrounded" by phase 2 in the modulus distribution. This brings questions about the actual physical presence of phase 1 in the investigated material.

Soft clustering might help understanding the phase distribution further (see Figure A.6). In particular regarding the most compliant phase, its posterior probability in the three-phase to five-phase distributions never reaches 1 and decreases with increasing number of phases until nearly 0.6 in the five-phase case. Its width also decreases with increasing number of phases. Thus, phase 1 loses its physical importance when the number of phases fitting the empirical modulus distribution increases. The soft clustering of the modulus

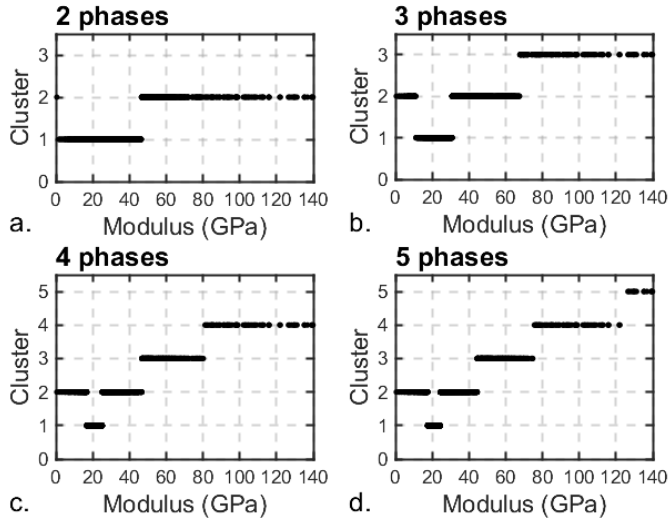

Figure A.5: Hard clustering of the modulus distribution of a cement paste at age of 28 days, fitted with a sum of (a) two, (b) three, (c) four and (d) five phases.

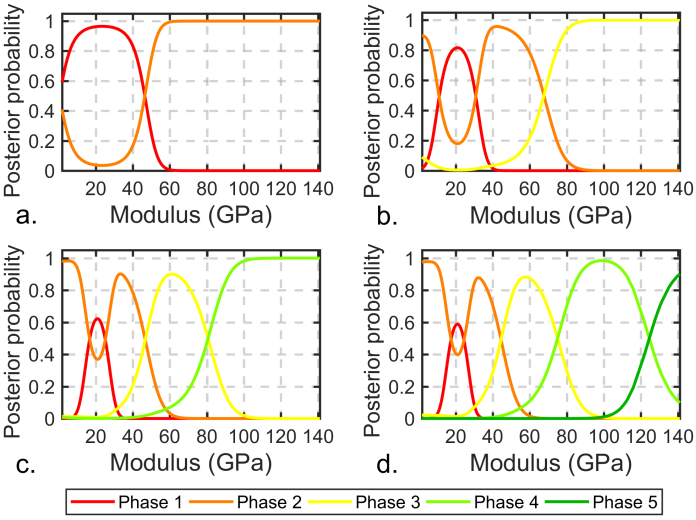

Figure A.6: Soft clustering of modulus distribution of a cement paste at age of 28 days, fitted with a sum of (a) two, (b) three, (c) four and (d) five phases.

distribution confirms that phases 1 and 2 of this distribution interact strongly with each other, independent of the number of phases, but in particular for fits with three or more phases.

A.4 Optimum statistical analysis

A.4.1 Fitting with experimental noise

The influence on the fit results, the phase properties and the number of phases of the noise amplitude was investigated. The differences between the phase properties of the investigated empirical modulus distribution between fits with and without noise were smaller than 0.07 % for the mean values, 3.7 % for the standard deviations and 1.4 % for the phase fractions. These values were reached for a three-phase fit with the largest noise values investigated. The error in determination of the phases' properties increases with the noise applied on the empirical modulus distribution.
In general, the standard deviation is the most affected fitting parameter: a higher experimental noise leads to larger standard deviations. Differently speaking, not considering the uncertainty on the empirical distribution may lead to underestimate the phases' standard deviation. However, from a more general point of view, a constant experimental noise throughout the empirical modulus distribution can be neglected in the deconvolution of the modulus of a heterogeneous material. The differences between the fit results with and without noise are indeed minimal compared to those generated by other fitting parameters (see discussion below).

A.4.2 Choice of data representation

The influence of the data representation on the fitting results is significant. The CDF representation brings better accuracy on the fits, diminishes the user influence and exhibits more intuitive fit parameters, in particular for the

phase fraction. Thus, it represents the best choice over the PDF representation.

Indeed, despite a higher number of degrees of freedom, the whole range of the empirical distribution is better fitted by the cumulative fitting distribution. The lower reduced χ^2 value of the fit from the PDF is induced by the small number of empirical data points in the PDF representation. Hence, the fitting curve can fit those points very well, inducing a low χ^2, whereas the fitting function can take any value between these points. Thus the CDF fit actually leads to a more precise representation of the empirical distribution and more precise fit results.

Moreover, the user influence is lower during a CDF fit compared to that during a PDF fit. This is first due to the suppression of the binning step and the subsequent choice of the bin width choice in the empirical data representation. Also, the much larger number of empirical data points in the CDF representation of the data decreases the influence of the starting parameters on the fit results . Last but not least, in a CDF-based fit, the calculation of the surface fraction of each phase is directly obtained from the weight of the phase and is thus a direct parameter of the fitting function. On the contrary, the phase fraction of a peak in a PDF-based fit is a derived parameter of the height, the width and the weight of each peak of the fitting function, as it is calculated as the relative surface under the curve.

A.4.3 Choice of fitting procedure

Fits made with the LM and ODR fitting procedures were compared based on the modulus distribution measured in the investigated polymer-modified cement paste (Table A.4). The effect of the fitting algorithm on the fitting results of the investigated distribution was negligible, as the differences between the fit results were minimal. However, the LM fitting algorithm presents advantages like the flexibility in the choice of number of phases.

The EM fitting procedure was also investigated and its results compared to those from the LM procedure. Due to the constraints on the sum of all phase fractions, the results with the EM procedure differed from the results made with LM fitting procedure. Indeed, this constraint implies that no part of the curve can be neglected by the fitting function which means that, in case of noisy empirical data, the noisy part of the curve would also be fitted.
Based on the modulus analysis of this sample, it is found that both LM and EM fitting procedures provide accurate, yet different, fit results, which cannot be distinguished as the actual phase properties distribution is unknown.
The comparison of the LM and the EM fitting procedures can be refined for materials with a better known composition (see e.g. the Cu-Cr composites investigated on Chapter 3).

A.4.4 Comparison criteria between fit results

When comparing fitting results from the LM procedure or from the EM procedure, the BIC is the most informative goodness-of-fit criteria. Indeed, similarly to the AIC, the BIC value is not limited to an interval and does not tend towards a finite number when the fit parameters are optimized. The r_a^2 rather tends towards 1 and the reduced χ^2 towards 0. A finite limit for the fit criterion implies that the difference between two fits is reduced to an infinitesimal value when both fits improve. This complicates the differentiation between both fits and, thus, finding the best model.
The BIC and AIC present similar characteristics, but the BIC is more suitable than the AIC to determine the best fit at constant number of phases, or the best number of mechanical phases in an empirical distribution. Indeed, the AIC favors fits with better accuracy but also with larger complexity, when the number of empirical data points is increased [106]. But in mechanical experiments, the analysis results should improve in accuracy with increasing number of data points, but without necessarily leading to an increased number of phases, as the number of phases is restricted by the physical number

of phases in the material. Thus, the BIC was preferably used in this thesis to select the best fit at a given number of phases, or the best number of mechanical phases in an empirical distribution. A lower BIC indicates a better fit when the number of degrees of freedom is limited, and thus, reduces the risk of over-fitting[11]. As an alternative criterion or when the BIC calculation is not available, the reduced χ^2 or the r_a^2 parameters should be used.

A.4.5 Determination of the number of mechanical phases

The accurate determination of the number of mechanical phases in a material depends on many factors. Besides factors related to the nanoindentation methods and the unknown experimental parameters, the selection of the best approximating model must be carefully examined. The physical meaning of each phase must be considered. For example, the phase parameters or the posterior probabilities can provide hints on which phase is more likely to capture spurious experimental effects or to contribute to the replicable part of the empirical distribution. Furthermore, using BIC model selection or clustering, can also bring the fitting results into perspective and help determining the best approximating model of a distribution.

[11] see for example `https://www.originlab.com/doc/Origin-Help/PostFit-CompareFitFunc`, visited on 7th May 2018.

B Tables

Cu-Cr composites data

The Tables B.1 to B.8 are related to the Cu-Cr composites investigated in Chapter 3. They present the phases' parameters of hardness and Young's modulus distributions measured with either the Continuous Stiffness Measurement (CSM) or the Express Test (ET) nanoindentation methods and fitted with either the Expectation Maximization (EM) or the Levenberg-Macquardt (LM) procedures.

Table B.1: Fitting results of Cu25Cr modulus distribution with CSM from EM fitting procedure

Indentation depth	Phase	Mean modulus (GPa)	St. dev. (GPa)	Phase fraction (%)
200 nm	1	148	5.0	64
	2	281	27.0	33
500 nm	1	143	6.4	63
	2	263	48.0	37
1000 nm	1	142	7.7	62
	2	260	70.0	38
1500 nm	1	142	7.6	58
	2	252	76.2	42
1950 nm	1	139	7.0	57
	2	244	72.1	43

Table B.2: Fitting results of Cu60Cr modulus distribution with CSM from EM fitting procedure

Indentation depth	Phase	Mean modulus (GPa)	St. dev. (GPa)	Phase fraction (%)
200 nm	1	137	4.9	46
	2	163	1.0	8
	3	246	14.2	13
	4	286	5.2	33
500 nm	1	148	10.8	58
	2	254	20.8	42
1000 nm	1	153	19.1	66
	2	239	17.3	34
1500 nm	1	128	1.7	20
	2	170	19.4	60
	3	235	7.2	20
1950 nm	1	171	31.1	100

Table B.3: Fitting results of Cu25Cr hardness distribution with CSM from EM fitting procedure

Indentation depth	Phase	Mean hardness (GPa)	St. dev. (GPa)	Phase fraction (%)
200 nm	1	2.1	0.07	56
	2	5.4	0.9	44
500 nm	1	1.5	0.04	51
	2	3.4	1.1	49
1000 nm	1	1.2	0.03	47
	2	2.7	1.1	53
1500 nm	1	1.0	0.04	46
	2	2.3	1.0	54
1900 nm	1	1.0	0.07	48
	2	2.2	0.9	52

Table B.4: Fitting results of Cu60Cr hardness distribution with CSM from EM fitting procedure

Indentation depth	Phase	Mean hardness (GPa)	St. dev. (GPa)	Phase fraction (%)
200 nm	1	2.5	0.4	54
	2	5.9	0.7	20
	3	6.1	0.07	26
500 nm	1	1.9	0.1	48
	2	3.8	1.0	34
	3	4.2	0.04	18
1000 nm	1	1.6	0.2	52
	2	3.2	0.8	48
1500 nm	1	1.4	0.1	42
	2	2.6	0.8	58
1900 nm	1	1.3	0.1	38
	2	2.3	0.6	62

Table B.5: Fitting results of Cu25Cr modulus distribution with ET from both EM and LM fitting procedures with between two and four phases.

Phase number	Fit parameter	EM		LM	
		3 phases	Opt. fit	2 phases	3 phases
1	Mean modulus (GPa)	145	138	144	139
	St. dev. (GPa)	14.2	7.5	12.4	8.1
	Phase fraction (%)	58.2	26.8	53.8	34.2
2	Mean modulus (GPa)	257	152	241	159
	St. dev. (GPa)	74.2	18.0	73.6	15.5
	Phase fraction (%)	39.9	33.9	42.9	24.4
3	Mean modulus (GPa)	731	262	-	257
	St. dev. (GPa)	302	73.6	-	85.9
	Phase fraction (%)	1.9	37.5	-	40.5
4	Mean modulus (GPa)	-	736	-	-
	St. dev. (GPa)	-	301	-	-
	Phase fraction (%)	-	1.8	-	-

Table B.6: Fitting results of Cu25Cr hardness distribution with ET from both EM and LM fitting procedures with between two and five phases.

Phase number	Fit parameter	EM		LM	
		3 phases	Opt. fit	2 phases	3 phases
1	Mean hardness (GPa)	1.2	1.1	1.2	1.1
	St. dev. (GPa)	0.12	0.04	0.12	0.04
	Phase fraction (%)	54.9	20.1	55.6	23.7
2	Mean hardness (GPa)	2.4	1.2	2.5	1.2
	St. dev. (GPa)	0.92	0.10	0.90	0.17
	Phase fraction (%)	42.9	23.5	42.2	37.4
3	Mean hardness (GPa)	11.0	1.4	-	2.7
	St. dev. (GPa)	5.9	0.31	-	0.91
	Phase fraction (%)	2.2	25.4	-	37.7
4	Mean hardness (GPa)	-	2.9	-	-
	St. dev. (GPa)	-	0.71	-	-
	Phase fraction (%)	-	28.8	-	-
5	Mean hardness (GPa)	-	10.6	-	-
	St. dev. (GPa)	-	5.9	-	-
	Phase fraction (%)	-	2.5	-	-

Table B.7: Fitting results of Cu60Cr modulus distribution with ET from both EM and LM fitting procedures with between two and four phases.

Phase number	Fit parameter	EM		LM	
		3 phases	Opt. fit	2 phases	3 phases
1	Mean modulus (GPa)	171	167	178	169
	St. dev. (GPa)	24.6	21.3	35.0	24.1
	Phase fraction (%)	26.9	22.8	35.0	24.1
2	Mean modulus (GPa)	307	287	325	298
	St. dev. (GPa)	65.4	64.6	63.3	70.1
	Phase fraction (%)	69.6	63.0	65.2	69.1
3	Mean modulus (GPa)	564	376	-	375
	St. dev. (GPa)	186	14.1	-	11.5
	Phase fraction (%)	3.5	9.4	-	6.1
4	Mean modulus (GPa)	-	518	-	-
	St. dev. (GPa)	-	185	-	-
	Phase fraction (%)	-	4.8	-	-

Table B.8: Fitting results of Cu60Cr hardness distribution with ET from both EM and LM fitting procedures with between two and four phases.

Phase number	Fit parameter	EM		LM	
		3 phases	Opt. fit	2 phases	3 phases
1	Mean hardness (GPa)	1.5	1.5	1.5	1.5
	St. dev. (GPa)	0.23	0.22	0.25	0.20
	Phase fraction (%)	27.0	24.9	27.9	20.3
2	Mean hardness (GPa)	3.1	3.1	3.2	3.1
	St. dev. (GPa)	0.68	0.78	0.67	1.0
	Phase fraction (%)	63.9	58.9	67.4	64.9
3	Mean hardness (GPa)	5.7	3.2	-	3.2
	St. dev. (GPa)	2.1	0.08	-	0.13
	Phase fraction (%)	9.1	8.0	-	11.7
4	Mean hardness (GPa)	-	5.9	-	-
	St. dev. (MPa)	-	2.1	-	-
	Phase fraction (%)	-	8.3	-	-

P. discophora data

The Tables B.9 and B.10 are related to the *Passiflora discophora* pads investigated in Chapter 4.

Table B.9: Modulus range of the pad structural areas

Structural area	Modulus limits (GPa)		Mean value (GPa)
	min	max	
1	0.2	0.9	0.55
2	0.9	1.9	1.4
3	1.4	2.9	2.15
4	2.6	4.3	3.45

Table B.10: Phase properties in *P. discophora* attachment pad cross sections and branchlet

Cross section	Phase 1			Phase 2			Phase 3			Phase 4		
	Mean modulus (GPa)	St. dev. (GPa)	Phase fraction (%)	Mean modulus (GPa)	St. dev. (GPa)	Phase fraction (%)	Mean modulus (GPa)	St. dev. (GPa)	Phase fraction (%)	Mean modulus (GPa)	St. dev. (GPa)	Phase fraction (%)
1	0.33	0.16	11	1.6	0.5	65	2.7	0.20	16	3.2	0.14	7.8
2	0.39	0.05	6.8	1.2	0.14	10	2.0	0.70	83	-	-	-
3	0.54	0.32	21	1.3	0.28	42	2.0	0.21	32	3.1	0.22	5.5
4	0.62	0.30	25	1.5	0.34	38	2.4	0.40	35	-	-	-
5	-	-	-	1.4	0.44	28	2.0	0.87	71	-	-	-
6	0.53	0.08	4.4	1.4	0.27	36	2.5	0.34	46	3.8	0.63	14
Branchlet	-	-	-	-	-	-	1.8	0.65	20	3.5	0.63	76

List of Figures

List of Tables

List of formulas

Bibliography

[1] G Constantinides, KS Ravi Chandran, FJ Ulm, and KJ Van Vliet. "Grid indentation analysis of composite microstructure and mechanics: Principles and validation". In: *Materials Science and Engineering A* 430 (2006), pp. 189–202. DOI: 10.1016/j.msea.2006.05.125.

[2] KU Kainer. "Basics of Metal Matrix Composites". In: *Metal Matrix Composites*. Ed. by KU Kainer. Weinheim: Wiley-VCH Verlag, 2006. Chap. 1. DOI: 10.1002/3527608117.ch1.

[3] A Mortensen and J Llorca. "Metal Matrix Composites". In: *Annual Review of Materials Research* 40 (2010), pp. 243–270. DOI: 10.1146/annurev-matsci-070909-104511.

[4] JW Hutchinson. "Plasticity at the micron scale". In: *Int. J. Solids Structures* 37 (2000), pp. 225–238. DOI: 10.1016/s0020-7683(99)00090-6.

[5] WD Nix. "Elastic and plastic properties of thin films on substrates: nanoindentation techniques". In: *Materials Science and Engineering: A* 234-236 (1997), pp. 37–44. DOI: 10.1016/S0921-5093(97)00176-7.

[6] MF Doerner and WD Nix. "Stresses and deformation processes in thin films on substrates". In: *Critical Reviews in Solid State and Materials Sciences* 14.3 (1988), pp. 225–268. DOI: 10.1080/10408438808243734.

[7] A Misra and H Kung. “Deformation Behavior of Nanostructured Metallic Multilayers”. In: *Advanced Engineering Materials* 3.4 (2001), pp. 217–222. DOI: 10.1002/1527-2648(200104)3:4<217::AID-ADEM217>3.0.CO;2-5.

[8] EO Hall. “Variation of Hardness of Metals with Grain Size”. In: *Nature* 173 (1954), pp. 948–949. DOI: 10.1038/173948b0.

[9] Y Li, AJ Bushby, and DJ Dunstan. “The Hall-Petch effect as a manifestation of the general size effect”. In: *Proc. R. Soc. A* 472 (2016), pp. 1–33. DOI: 10.1098/rspa.2015.0890.

[10] W Smith and J Hashemi. *Foundations of Materials Science and Engineering*. Ed. by McGraw-Hill. 4th ed. New York, 2006.

[11] D Qu, Z Zhou, J Tan, and J Aktaa. “Characterization of W/Fe functionally graded materials manufactured by resistance sintering under ultra-high pressure”. In: *Fusion Engineering and Design* 91 (2015), pp. 21–24. DOI: 10.1016/j.fusengdes.2014.12.014.

[12] S Suresh. “Graded materials for resistance to contact deformation and damage.” In: *Science* 292.5526 (2001), pp. 2447–2451. DOI: 10.1126/science.1059716.

[13] MA Meyers, PY Chen, A YM Lin, and Y Seki. “Biological materials: Structure and mechanical properties”. In: *Progress in Materials Science* 53.1 (2008), pp. 1–206. DOI: 10.1016/j.pmatsci.2007.05.002.

[14] RK Nalla, JJ Kruzic, and RO Ritchie. “On the origin of the toughness of mineralized tissue: microcracking or crack bridging?” In: *Bone* 34.5 (2004), pp. 790–798. DOI: 10.1016/j.bone.2004.02.001.

[15] J Dunlop and P Fratzl. “Biological Composites”. In: *Annual Review of Materials Research* 40.1 (2010), pp. 1–24. DOI: 10.1146/annurev-matsci-070909-104421.

[16] J Dunlop, R Weinkamer, and P Fratzl. “Artful interfaces within biological materials”. In: *Materials Today* 14.3 (2011), pp. 70–78. DOI: 10.1016/S1369-7021(11)70056-6.

[17] J Sun and B Bhushan. “Hierarchical structure and mechanical properties of nacre: a review”. In: *RSC Advances* 2.20 (2012), p. 7617. DOI: 10.1039/c2ra20218b.

[18] D Green, J Winandy, and D Kretschmann. *Mechanical properties of wood*. Tech. rep. Madison, WI: USDA Forest Service, Forst Products Laboratory, 1999, pp. 4.1–4.45.

[19] K Kamino. “Mini-review: barnacle adhesives and adhesion.” In: *Biofouling* 29.6 (2013), pp. 735–49. DOI: 10.1080/08927014.2013.800863.

[20] Kellar Autumn and Jonathan Puthoff. “Properties, Principles, and Parameters of the Gecko Adhesive System”. In: *Biological Adhesives*. Ed. by A Smith and J Callow. Cham: Springer, 2016. Chap. 11, pp. 245–280. DOI: 10.1007/978-3-319-46082-6_11.

[21] S Gorb. “Biological attachment devices: exploring nature’s diversity for biomimetics”. In: *Philosophical transactions. Series A, Mathematical, physical, and engineering sciences* 366.1870 (2008), pp. 1 557 –1 574. DOI: 10.1098/rsta.2007.2172.

[22] B Melzer, T Steinbrecher, R Seidel, O Kraft, R Schwaiger, and T Speck. “The attachment strategy of English ivy: A complex mechanism acting on several hierarchical levels”. In: *Journal of the Royal Society Interface* 7.50 (2010), pp. 1383–1389. DOI: 10.1098/rsif.2010.0140.

[23] A Goriely and S Neukirch. “Mechanics of Climbing and Attachment in Twining Plants”. In: *Physical Review Letters* 97 (2006). DOI: 10.1103/PhysRevLett.97.184302.

[24] H Bohn, F Guenther, S Fink, and T Speck. “A Passionate Free Climber: Structural Development and Functional Morphology of the Adhesive Tendrils in Passiflora discophora”. In: *International Journal of Plant Sciences* 176.3 (2015), pp. 294–305. DOI: 10.1086/680231.

[25] T Steinbrecher, G Beuchle, B Melzer, T Speck, O Kraft, and R Schwaiger. “Structural Development and Morphology of the Attachment System of Parthenocissus tricuspidata”. In: *International Journal of Plant Sciences* 172.9 (2011), pp. 1120–1129. DOI: 10.1086/662129.

[26] T Steinbrecher. “Mechanics and morphology of permanent attachment systems in plants”. PhD Thesis. KIT, Karlsruhe, Germany, 2011.

[27] S Schmier, C Bos, S Kleiser, R Kappel, HF Bohn, R Schwaiger, and T Speck. “The attachment system of Passiflora discophora as an inspiration for bioinspired technical anchorage systems”. In: *Bionik: Patente aus der Natur, 8.* Bremen: Bionik-Innovations-Centrum, 2016, pp. 174–179.

[28] P. Trtik, B. Münch, P. Gasser, A. Leemann, R. Loser, R. Wepf, and P. Lura. “Focussed ion beam nanotomography reveals the 3D morphology of different solid phases in hardened cement pastes”. In: *Journal of Microscopy* 241.3 (2011), pp. 234–242. DOI: 10.1111/j.1365-2818.2010.03433.x.

[29] S Diamond. “The microstructure of cement paste and concrete - A visual primer”. In: *Cement and Concrete Composites* 26.8 (2004), pp. 919–933. DOI: 10.1016/j.cemconcomp.2004.02.028.

[30] I Richardson. “Nature of C-S-H in hardened cements”. In: *Cement and Concrete Research* 29.8 (1999), pp. 1131–1147. DOI: 10.1016/s0008-8846(99)00168-4.

[31] H Jennings. “Model for two types of calcium silicate hydrate in the microstructure of Portland cement pastes”. In: *Cement and Concrete Research* 30.6 (2000), pp. 855–863. DOI: 10.1016/S0008-8846(00)00257-X.

[32] H Jennings, J Thomas, J Gevrenov, G Constantinides, and FJ Ulm. “A multi-technique investigation of the nanoporosity of cement paste”. In: *Cement and Concrete Research* 37.3 (2007), pp. 329–336. DOI: 10.1016/j.cemconres.2006.03.021.

[33] P Acker. “Swelling, shrinkage and creep: a mechanical approach to cement hydration”. In: *Materials and Structures* 37.268 (2004), pp. 237–243. DOI: 10.1617/14161.

[34] E Stora, QC He, and B Bary. “Influence of inclusion shapes on the effective linear elastic properties of hardened cement pastes”. In: *Cement and Concrete Research* 36.7 (2006), pp. 1330–1344. DOI: 10.1016/j.cemconres.2006.02.007.

[35] A Allen, J Thomas, and H Jennings. “Composition and density of nanoscale calcium-silicate-hydrate in cement.” In: *Nature materials* 6.4 (2007), pp. 311–316. DOI: 10.1038/nmat1871.

[36] G Constantinides and FJ Ulm. “The nanogranular nature of C-S-H”. In: *Journal of the Mechanics and Physics of Solids* 55.1 (2007), pp. 64–90. DOI: 10.1016/j.jmps.2006.06.003.

[37] G Constantinides and FJ Ulm. “The effect of two types of C-S-H on the elasticity of cement-based materials: Results from nanoindentation and micromechanical modeling”. In: *Cement and Concrete Research* 34.1 (2004), pp. 67–80. DOI: 10.1016/S0008-8846(03)00230-8.

[38] A Boumiz, C Vernet, and F Cohen Tenoudhi. “Mechanical Properties of Cement Pastes and Mortars at Early Ages Evolution with Time

and Degree of Hydration". In: *Advanced Cement Based Materials* 3 (1996), pp. 94–106. DOI: 10.1016/1065-7355(95)00072-0.

[39] Y Ohama. *Handbook of polymer-modified concrete and mortars: properties and process technology*. Ed. by V. S. Ramachandran. Mill Road, Park Ridge, New Jersey: Noyes Publications, 1995. ISBN: 0815513585.

[40] R Wang, DX Ma, and PM Wang. "Waterproof Performance of Polymer-Modified Cement Mortar". In: *Advanced Materials Research* 687 (2013), pp. 213–218. DOI: 10.4028/www.scientific.net/AMR.687.213.

[41] Y Ohama. "Polymer-based admixtures". In: *Cement and Concrete Composites* 20.2-3 (1998), pp. 189–212. DOI: 10.1016/S0958-9465(97)00065-6.

[42] A Dimmig. "Einflüsse von Polymeren auf die Mikrostruktur und die Dauerhaftigkeit kunststoffmodifizierter Moertel (PCC)". PhD Thesis. Bauhaus-University Weimar, 2002.

[43] DW Fowler. "Polymers in concrete: A vision for the 21st century". In: *Cement and Concrete Composites* 21.5-6 (1999), pp. 449–452. DOI: 10.1016/S0958-9465(99)00032-3.

[44] L Czarnecki. "Concrete-polymer Composites : Trends Shaping the Future". In: *International Journal of the Society of Materials Engineering for Resources* 15.1 (2007), pp. 1–5. DOI: 10.5188/ijsmer.15.1.

[45] A Dimmig-Osburg. "Innovations Based on PCC". In: *Advanced Materials Research* 687 (2013), pp. 369–377. DOI: 10.4028/www.scientific.net/AMR.687.369.

[46] J Kardon. "Polymer-Modified Concrete: Review". In: *Journal of Materials in Civil Engineering* 9.2 (1997), pp. 85–92. DOI: 10.1061/(ASCE)0899-1561(1997)9:2(85).

[47] E Sakai and J Sugita. “Composite mechanism of polymer modified cement”. In: *Cement and Concrete Research* 25.1 (1995), pp. 127–135. DOI: 10.1016/0008-8846(94)00120-N.

[48] MUK Afridi, Y Ohama, K Demura, and MZ Iqbal. “Development of polymer films by the coalescence of polymer particles in powdered and aqueous polymer-modified mortars”. In: *Cement and Concrete Research* 33.11 (2003), pp. 1715–1721. DOI: 10.1016/S0008-8846(02)01094-3.

[49] S Marceau, F Lespinasse, J Bellanger, C Mallet, and F Boinski. “Microstructure and mechanical properties of polymer-modified mortars”. In: *European Journal of Environmental and Civil Engineering* 16.5 (2012), pp. 571–581. DOI: 10.1080/19648189.2012.675148.

[50] A Flohr and A Dimmig-Osburg. “Study on the Load-Deformation Behavior of Modified Cement Concrete”. In: *Advanced Materials Research* 687 (2013), pp. 198–203. DOI: 10.4028/www.scientific.net/AMR.687.198.

[51] B Prakash, A Titiksh, and AA Qureshi. “Evaluating the Performance of Polymer Modified Concrete in Terms of Structural Properties”. In: *Journal of Structural Technology* 1.1 (2016), pp. 1–10.

[52] H Ma and Z Li. “Microstructures and mechanical properties of polymer modified mortars under distinct mechanisms”. In: *Construction and Building Materials* 47 (2013), pp. 579–587. DOI: 10.1016/j.conbuildmat.2013.05.048.

[53] Fischerwerke GmbH. *Injection mortar FIS EM*. 2016. URL: http://www.fischer.de/en/Product-Range/Chemical-fixings/Injection-mortar-FIS-EM (visited on 07/27/2016).

[54] R James, C de la Guardia, and C McCreary. “Strength of Epoxy-Grouted Anchor Bolts in Concrete”. In: *Journal of Structural Engineering* 113.12 (1987), pp. 2365–2381. DOI: 10.1061/(ASCE)0733-9445(1987)113:12(2365).

[55] RA Cook. “Behavior of chemically bonded anchors”. In: *Journal of Structural Engineering* 119.9 (1993), pp. 2744–2762.

[56] RA Cook, R Eligehausen, and J Appl. “Overview: Behavior of Adhesive Bonded Anchors”. In: *Beton- und Stahlbetonbau* 102.S1 (2007), pp. 16–21. DOI: 10.1002/best.200710107.

[57] S Yilmaz, MA Oezen, and Y Yardim. “Tensile behavior of post-installed chemical anchors embedded to low strength concrete”. In: *Construction and Building Materials* 47 (2013), pp. 861–866. DOI: 10.1016/j.conbuildmat.2013.05.032.

[58] M Yang, M Thota, and Y Zhao. “Creep Design of Epoxy Bonded Anchor System”. In: *Mechanics of Advanced Materials and Structures* 22.3 (2015), pp. 159–167. DOI: 10.1080/15376494.2012.723299.

[59] P Upadhyaya and S Kumar. “Pull-out capacity of adhesive anchors: An analytical solution”. In: *International Journal of Adhesion and Adhesives* 60 (2015), pp. 54–62. DOI: 10.1016/j.ijadhadh.2015.03.006.

[60] S Epackachi, O Esmaili, SR Mirghaderi, and AAT Behbahani. “Behavior of adhesive bonded anchors under tension and shear loads”. In: *Journal of Constructional Steel Research* 114 (2015), pp. 269–280. DOI: 10.1016/j.jcsr.2015.07.022.

[61] MF Doerner and WD Nix. “A method for interpreting the data from depth-sensing indentation instruments”. In: *Journal of Materials Research* 1.04 (1986), pp. 601–609. DOI: 10.1557/JMR.1986.0601.

[62] R King. “Elastic analysis of some punch problems for a layered medium”. In: *International Journal of Solids and Structures* 23.12 (1987), pp. 1657–1664. DOI: 10.1016/0020-7683(87)90116-8.

[63] W Oliver and G Pharr. “An improved technique for determining hardness and elastic modulus using load and displacement sensing indentation experiments”. In: *Journal of Materials Research* 7.6 (1992), pp. 1564–1583. DOI: 10.1557/JMR.1992.1564.

[64] J Hay, P Agee, and E Herbert. “Continuous stiffness measurement during instrumented indentation testing”. In: *Experimental Techniques* 34.3 (2010), pp. 86–94. DOI: 10.1111/j.1747-1567.2010.00618.x.

[65] X Li and B Bhushan. “A review of nanoindentation continuous stiffness measurement technique and its applications”. In: *Materials Characterization* 48.1 (2002), pp. 11–36. DOI: 10.1016/S1044-5803(02)00192-4.

[66] G Odegard, T Gates, and H Herring. “Characterization of Viscoelastic Properties of Polymeric Materials Through Nanoindentation”. In: *Society for experimental mechanics* 45.2 (2005), pp. 130–136. DOI: 10.1177/0014485105052320.

[67] E Herbert, W Oliver, A Lumsdaine, and G Pharr. “Measuring the constitutive behavior of viscoelastic solids in the time and frequency domain using flat punch nanoindentation”. In: *Journal of Materials Research* 24.03 (2009), pp. 626–637. DOI: 10.1557/jmr.2009.0089.

[68] E Herbert, P Sudharshan Phani, and K Johanns. “Nanoindentation of viscoelastic solids: A critical assessment of experimental methods”. In: *Current Opinion in Solid State and Materials Science* 19.6 (2015), pp. 334–339. DOI: 10.1016/j.cossms.2014.12.006.

[69] J Hay, A Bolshakov, and G Pharr. “A critical examination of the fundamental relations used in the analysis of nanoindentation data”. In: *Journal of Materials Research* 14.6 (1999), pp. 2296–2305. DOI: 10.1557/JMR.1999.0306.

[70] D Lucca, K Herrmann, and M Klopfstein. “Nanoindentation: Measuring methods and applications”. In: *CIRP Annals - Manufacturing Techno-logy* 59.2 (2010), pp. 803–819. DOI: 10.1016/j.cirp.2010.05.009.

[71] W Oliver and G Pharr. “Measurement of hardness and elastic modulus by instrumented indentation: Advances in understanding and refinements to methodology”. In: *Journal of Materials Research* 19.1 (2004), pp. 3–20. DOI: 10.1557/jmr.2004.19.1.3.

[72] X Li and B Bhushan. “Development of continuous stiffness measurement technique for composite magnetic tapes”. In: *Scripta Materialia* 42.10 (2000), pp. 929–935. DOI: 10.1016/S1359-6462(00)00316-X.

[73] X Huang and A Pelegri. “Mechanical Characterization of Thin Film Materials with Nanoindentation Measurements and FE Analysis”. In: *Journal of Composite Materials* 40.15 (2006), pp. 1393–1407. ISSN: 0021-9983. DOI: 10.1177/0021998305059728.

[74] A Pelegri and X Huang. “Nanoindentation on soft film/hard substrate and hard film/soft substrate material systems with finite element analysis”. In: *Composites Science and Technology* 68.1 (2008), pp. 147–155. DOI: 10.1016/j.compscitech.2007.05.033.

[75] WG Jiang, JJ Su, and XQ Feng. “Effect of surface roughness on nanoindentation test of thin films”. In: *Engineering Fracture Mechanics* 75.17 (2008), pp. 4965–4972. DOI: 10.1016/j.engfracmech.2008.06.016.

[76] K Durst, M Goeken, and H Vehoff. “Finite element study for nanoindentation measurements on two-phase materials”. In: *Journal of Materials Research* 19.1 (2004), pp. 85–93. DOI: 10.1557/jmr.2004.19.1.85.

[77] P Trtik, B Muench, and P Lura. “A critical examination of statistical nanoindentation on model materials and hardened cement pastes based on virtual experiments”. In: *Cement and Concrete Composites* 31.10 (2009), pp. 705–714. DOI: 10.1016/j.cemconcomp.2009.07.001.

[78] M Oyen. “Nanoindentation of Biological and Biomimetic Materials”. In: *Experimental Techniques* 37.1 (2013), pp. 73–87. DOI: 10.1111/j.1747-1567.2011.00716.x.

[79] J Kaufman and C Klapperich. “Surface detection errors cause overestimation of the modulus in nanoindentation on soft materials.” In: *Journal of the mechanical behavior of biomedical materials* 2.4 (2009), pp. 312–317. DOI: 10.1016/j.jmbbm.2008.08.004.

[80] E Donnelly, SP Baker, AL Boskey, and MCH van der Meulen. “Effects of surface roughness and maximum load on the mechanical properties of cancellous bone measured by nanoindentation”. In: *Journal of Biomedical Materials Research Part A* 77A.2 (2006), pp. 426–435. DOI: 10.1002/jbm.a.30633.

[81] SP Ho, M Balooch, HE Goodis, GW Marshall, and SJ Marshall. “Ultrastructure and nanomechanical properties of cementum dentin junction”. In: *Jounral of Biomedical Research Part A* 68.2 (2004), pp. 345–351. DOI: 10.1002/jbm.a.20061.

[82] D Ebenstein and L Pruitt. “Nanoindentation of biological materials”. In: *Nano Today* 1.3 (2006), pp. 26–33. DOI: 10.1016/S1748-0132(06)70077-9.

[83] N Rodriguez-Florez, M Oyen, and S Shefelbine. “Insight into differences in nanoindentation properties of bone”. In: *Journal of the Mechanical Behavior of Biomedical Materials* 18 (2013), pp. 90–99. DOI: 10.1016/j.jmbbm.2012.11.005.

[84] L Wagner, C Bos, T Bader, and K De Borst. “Effect of Water on the Mechanical Properties of Wood Cell Walls - Results of a Nanoindentation Study”. In: *BioResources* 10.3 (2015), pp. 4011–4025. DOI: 10.15376/biores.10.3.4011-4025.

[85] CM Hayot, E Forouzesh, A Goel, Z Avramova, and J Turner. “Viscoelastic properties of cell walls of single living plant cells determined by dynamic nanoindentation”. In: *Journal of Experimental Botany* 63.7 (2012), pp. 2525–2540. DOI: 10.1093/jxb/err428.

[86] C Hu and Z Li. “A review on the mechanical properties of cement-based materials measured by nanoindentation”. In: *Construction and Building Materials* 90 (2015), pp. 80–90. DOI: 10.1016/j.conbuildmat.2015.05.008.

[87] K Velez, S Maximilien, D Damidot, G Fantozzi, and F Sorrentino. “Determination by nanoindentation of elastic modulus and hardness of pure constituents of Portland cement clinker”. In: *Cement and Concrete Research* 31.4 (2001), pp. 555–561. DOI: 10.1016/S0008-8846(00)00505-6.

[88] F Pelisser, PJP Gleize, and A Mikowski. “Effect of the Ca/Si Molar Ratio on the Micro/nanomechanical Properties of Synthetic C-S-H Measured by Nanoindentation”. In: *The Journal of Physical Chemistry C* 116 (2012), pp. 17219–17227. DOI: 10.1021/jp302240c.

[89] EM Foley, JJ Kim, and MM Reda Taha. “Synthesis and nano-mechanical characterization of calcium-silicate-hydrate (C-S-H) made with 1.5 CaO/SiO_2 mixture”. In: *Cement and Concrete Research*

42.9 (2012), pp. 1225–1232. DOI: 10.1016/j.cemconres.2012.05.014.

[90] JJ Kim, EM Foley, and MM Reda Taha. “Nano-mechanical characterization of synthetic calcium-silicate-hydrate (C-S-H) with varying CaO/SiO2 mixture ratios”. In: *Cement and Concrete Composites* 36.1 (2013), pp. 65–70. DOI: 10.1016/j.cemconcomp.2012.10.001.

[91] D. Davydov, M. Jirasek, and L. Kopecky. “Critical aspects of nano-indentation technique in application to hardened cement paste”. In: *Cement and Concrete Research* 41.1 (2011), pp. 20–29. DOI: 10.1016/j.cemconres.2010.09.001.

[92] J Nemecek, V Kralik, and J Vondrejc. “Micromechanical analysis of heterogeneous structural materials”. In: *Cement and Concrete Composites* 36 (2013), pp. 85–92. DOI: 10.1016/j.cemconcomp.2012.06.015.

[93] C Hu. “Nanoindentation as a tool to measure and map mechanical properties of hardened cement pastes”. In: *MRS Communications* 5.01 (2015), pp. 83–87. DOI: 10.1557/mrc.2015.3.

[94] H Engqvist and U Wiklund. “Mapping of mechanical properties of WC-Co using nanoindentation”. In: *Tribology Letters* 8 (2000), pp. 147–152. DOI: 10.1023/A:1019143419984.

[95] Jennifer Hay and Phillip Agee. “Mapping the Mechanical Properties of Alloyed Magnesium (AZ 61)”. In: *MEMS and Nanotechnology*. Ed. by III G Shaw, B Prorok, L Starman, and C Furlong. Vol. 5. Conference Proceedings of the Society for Experimental Mechanics Series. Cham: Springer, 2014. Chap. 12, pp. 97–101. DOI: 10.1007/978-3-319-00780-9_12.

[96] N Randall, M Vandamme, and FJ Ulm. “Nanoindentation analysis as a two-dimensional tool for mapping the mechanical properties of complex surfaces”. In: *Journal of Materials Research* 24 (2009), pp. 679–690. DOI: 10.1557/jmr.2009.0149.

[97] FJ Ulm, M Vandamme, H Jennings, J Vanzo, M Bentivegna, K Krakowiak, G Constantinides, C Bobko, and K Van Vliet. “Does microstructure matter for statistical nanoindentation techniques?” In: *Cement and Concrete Composites* 32.1 (2010), pp. 92–99. DOI: 10.1016/j.cemconcomp.2009.08.007.

[98] C Hu and Z Li. “Micromechanical investigation of Portland cement paste”. In: *Construction and Building Materials* 71 (2014), pp. 44–52. DOI: 10.1016/j.conbuildmat.2014.08.017.

[99] M Miller, C Bobko, M Vandamme, and F Ulm. “Surface roughness criteria for cement paste nanoindentation”. In: *Cement and Concrete Research* 38.4 (2008), pp. 467–476. DOI: 10.1016/j.cemconres.2007.11.014.

[100] AEOJ Delesse. *Procédé mécanique pour déterminer la composition des roches*. Ed. by F Savy (in French). Paris, 1866.

[101] M Vandamme, FJ Ulm, and P Fonollosa. “Nanogranular packing of C-S-H at substochiometric conditions”. In: *Cement and Concrete Research* 40.1 (2010), pp. 14–26. DOI: 10.1016/j.cemconres.2009.09.017.

[102] W da Silva, J Nemecek, and P Stemberk. “Nanotechnology and construction: use of nanoindentation measurements to predict macroscale elastic properties of high strength cementitious composites”. In: *Revista IBRACON de Estruturas e Materiais* 5.2 (2012), pp. 284–295. DOI: 10.1590/S1983-41952012000300002.

[103] C Hu, Y Gao, Y Zhang, and Z Li. “Statistical nanoindentation technique in application to hardened cement pastes: Influences of material microstructure and analysis method”. In: *Construction and Building Materials* 113 (2016), pp. 306–316. DOI: 10.1016/j.conbuildmat.2016.03.064.

[104] P Lura, P Trtik, and B Münch. “Validity of recent approaches for statistical nanoindentation of cement pastes”. In: *Cement and Concrete Composites* 33.4 (2011), pp. 457–465. DOI: 10.1016/j.cemconcomp.2011.01.006.

[105] TO Kvalseth. “Cautionary Note about R2”. In: *American Statistician* 39.4 (1985), pp. 279–285. DOI: 10.1080/00031305.1985.10479448.

[106] K Aho, DW Derryberry, and T Peterson. “Model selection for ecologists: The worldviews of AIC and BIC”. In: *Ecology* 95 (2014), pp. 631–636. DOI: 10.1890/13-1452.1.

[107] C Fraley and AE Raftery. “How Many Clusters? Which Clustering Method? Answers Via Model-Based Cluster Analysis”. In: *The Computer Journal* 41.8 (1998), pp. 578–588. DOI: 10.1093/comjnl/41.8.578.

[108] KP Burnham and DR Anderson. *Model selection and multimodel inference: a practical information-theoretic approach*. 2nd ed. New York: Springer Verlag, 2002. ISBN: 0387953647.

[109] K Klinski-Wetzel, C Kowanda, M Heilmaier, and FEH Mueller. “The influence of microstructural features on the electrical conductivity of solid phase sintered CuCr composites”. In: *Journal of Alloys and Compounds* 631 (2015), pp. 237–247. DOI: 10.1016/j.jallcom.2014.12.249.

[110] K Jacob, S Priya, and Y Waseda. “Thermodynamic study of liquid Cu-Cr alloys and metastable liquid immiscibility”. In: *Zeitschrift für Metallkunde/Materials Research and Advanced Techniques* 91.7 (2000), pp. 594–600.

[111] K Klinski-Berger. “Charakterisierung von Kupfer-Chrom-Verbundwerkstoffen für die Schalttechnik”. PhD Thesis. TU Darmstadt, 2015, p. 175.

[112] MF Ashby and DRH Jones. *Engineering Materials 1*. 4th ed. Elsevier Ltd., 2012. ISBN: 9780080966656. DOI: 10.1016/C2009-0-64288-4.

[113] E Brandes and G Brook. *Smithells Metal Reference Book*. Oxford: Reed Educational and Professional Publishing, 1992. ISBN: 0 7506 3624 6.

[114] *Revolutionary Agilent Express Test Option for the Nano Indenter G200*. 2014. URL: literature.cdn.keysight.com/litweb/pdf/5990-9948EN.pdf (visited on 09/06/2018).

[115] M Sebastiani, R Moscatelli, F Ridi, P Baglioni, and F Carassiti. “High-resolution high-speed nanoindentation mapping of cement pastes: Unravelling the effect of microstructure on the mechanical properties of hydrated phases”. In: *Materials and Design* 97 (2016), pp. 372–380. DOI: 10.1016/j.matdes.2016.02.087.

[116] K McElhaney, J Vlassak, and W Nix. “Determination of indenter tip geometry and indentation contact area for depth-sensing indentation experiments”. In: *Journal of Materials Research* 13.05 (1998), pp. 1300–1306. DOI: 10.1557/JMR.1998.0185.

[117] *E112-12: Standard Test Methods for Determining Average Grain Size*. Tech. rep. ASTM International, 2012. DOI: 10.1520/E0112-12.1.4.

[118] H Bückle. “Use of the hardness test to determine other material properties”. In: *The Science of Hardness Testing and Its Research Applications* (1973), pp. 453–491.

[119] AR Denton and NW Ashcroft. “Vegard’s law”. In: *Physical Review A* 43.6 (1991), pp. 3161–3164. DOI: 10.1103/PhysRevA.43.3161.

[120] M Liu, B Shi, J Guo, X Cai, and H Song. “Lattice constant dependence of elastic modulus for ultrafine grained mild steel”. In: *Scripta Materialia* 49.2 (2003), pp. 167–171. DOI: 10.1016/S1359-6462(03)00211-2.

[121] AB Lebedev, YA Burenkov, AE Romanov, VI Kopylov, VP Filonenko, and VG Gryaznov. “Softening of the elastic modulus in submicrocrystalline copper”. In: *Materials Science and Engineering A* 203 (1995), pp. 165–170. DOI: 10.1016/0921-5093(95)09868-2.

[122] V Kralik and J Nemecek. “Comparison of nanoindentation techniques for local mechanical quantification of aluminium alloy”. In: *Materials Science and Engineering: A* 618 (2014), pp. 118–128. DOI: 10.1016/j.msea.2014.08.036.

[123] J Moon, S Kim, J Jang, J Lee, and C Lee. “Orowan strengthening effect on the nanoindentation hardness of the ferrite matrix in microalloyed steels”. In: *Materials Science and Engineering A* 487.1-2 (2008), pp. 552–557. DOI: 10.1016/j.msea.2007.10.046.

[124] T Gladman. “Precipitation hardening in metals”. In: *Materials Science and Technology* 15.1 (1999), pp. 30–36. DOI: 10.1179/026708399773002782.

[125] G Pharr, E Herbert, and Y Gao. “The Indentation Size Effect: A Critical Examination of Experimental Observations and Mechanistic Interpretations”. In: *Annual Review of Materials Research* 40.1 (2010), pp. 271–292. DOI: 10.1146/annurev-matsci-070909-104456.

[126] WD Nix and HJ Gao. “Indentation size effects in crystalline materials: A law for strain gradient plasticity”. In: *Journal of the Mechanics and Physics of Solids* 46.3 (1998), pp. 411–425. DOI: 10.1016/s0022-5096(97)00086-0.

[127] JD Gale, A Achuthan, and DJ Morrison. “Indentation Size Effect (ISE) in Copper Subjected to Severe Plastic Deformation (SPD)”. In: *Metallurgical and Materials Transactions A* 45.5 (2014), pp. 2487–2497. DOI: 10.1007/s11661-014-2201-9.

[128] JH Strader. “A Study of the Indentation Size Effect in Copper”. PhD thesis. University of Tennessee, Knoxville, 2008.

[129] O Franke, J Trenkle, and C Schuh. “Temperature dependence of the indentation size effect”. In: *Journal of Materials Research* 25.07 (2010), pp. 1225–1229. DOI: 10.1557/JMR.2010.0159.

[130] K Durst, B Backes, and M Goeken. “Indentation size effect in metallic materials: Correcting for the size of the plastic zone”. In: *Scripta Materialia* 52.11 (2005), pp. 1093–1097. DOI: 10.1016/j.scriptamat.2005.02.009.

[131] K Durst, B Backes, O Franke, and M Göken. “Indentation size effect in metallic materials: Modeling strength from pop-in to macroscopic hardness using geometrically necessary dislocations”. In: *Acta Materialia* 54.9 (2006), pp. 2547–2555. DOI: 10.1016/j.actamat.2006.01.036.

[132] B Backes, Y Huang, M Göken, and K Durst. “The correlation between the internal material length scale and the microstructure in nanoindentation experiments and simulations using the conventional mechanism-based strain gradient plasticity theory”. In: *Journal of Materials Research* 24.3 (2009), pp. 1197–1207. DOI: 10.1557/jmr.2009.0123.

[133] S Isnard and W Silk. “Moving with climbing plants from Charles Darwin’s time into the 21st century”. In: *American journal of botany* 96.7 (2009), pp. 1205–21. DOI: 10.3732/ajb.0900045.

[134] C Bos, R Kappel, and R Schwaiger. “Optimized for permanent attachment: structure and biomechanics of the pads of the climbing passionflower Passiflora discophora”. In: *to be submitted* ().

[135] E Kotsiomiti and JF McCabe. “Experimental wax mixtures for dental use”. In: *Journal of Oral Rehabilitation* 24.7 (2008), pp. 517–521. DOI: 10.1111/j.1365-2842.1997.tb00367.x.

[136] L Gibson. “The hierarchical structure and mechanics of plant materials.” In: *Journal of the Royal Society, Interface / the Royal Society* 9.76 (2012), pp. 2749–66. DOI: 10.1098/rsif.2012.0341.

[137] CS Lee, E Jones, and R Kingsland. “Poisson’s ratio of engineering plastics”. In: *Advances in Polymer Technology* 6.1 (1986), pp. 85–90. ISSN: 07306679. DOI: 10.1002/adv.1986.060060106.

[138] M Sebastiani, F Massimi, and R Moscatelli. *CSM and DCM-Express Nanoindentation Mapping on Lithium/Polymer Battery Composites*. URL: http://literature.agilent.com/litweb/pdf/5991-3519EN.pdf (visited on 12/02/2014).

[139] JJ Beaudoin and VS Ramachandran. “A new perspective on the hydration characteristics of cement phases”. In: *Cement and Concrete Research* 22.4 (1992), pp. 689–694. DOI: 10.1016/0008-8846(92)90021-M.

[140] MAA Abd Elaty. “Compressive strength prediction of Portland cement concrete with age using a new model”. In: *HBRC Journal* 10.2 (2014), pp. 145–155. DOI: 10.1016/j.hbrcj.2013.09.005.

[141] L Göbel, C Bos, R Schwaiger, and A Osburg. “Micromechanics-Based Prediction of the Elastic Properties of Polymer-Modified Cementitious Materials”. In: *High Tech Concrete: Where Technology and Engineering Meet*. 2018, pp. 264–272. DOI: 10.1007/978-3-319-59471-2_33.

[142] EG Herbert, WC Oliver, and GM Pharr. “Nanoindentation and the dynamic characterization of viscoelastic solids”. In: *Journal of Physics D: Applied Physics* 41.7 (2008), p. 74021. DOI: 10.1088/0022-3727/41/7/074021.

[143] G Sewell. “Importance and measurement of minimum film-forming temperature”. In: *Pigment and Resin Technology* 27.3 (1998), pp. 173–174. DOI: 10.1108/03699429810218747.

[144] R Ollitrault-Fichet, C Gauthier, G Clamen, and P Boch. “Microstructural aspects in a polymer-modified cement”. In: *Cement and Concrete Research* 28.12 (1998), pp. 1687–1693. DOI: 10.1016/S0008-8846(98)00153-7.

[145] A Beeldens, D Van Gemert, H Schorn, Y Ohama, and L Czarnecki. “From microstructure to macrostructure: An integrated model of structure formation in polymer-modified concrete”. In: *Materials and Structures* 38.280 (2005), pp. 601–607. DOI: 10.1617/14215.

[146] A Ranganathan. “The Levenberg-Marquardt Algorithm”. In: *Tutoral on LM algorithm* 11.1 (2004), pp. 101–110.

[147] MD Bates and DG Watts. *Nonlinear Regression Analysis and Its Applications*. Wiley, 1988. DOI: 10.1002/9780470316757.

[148] DW Marquardt. “An Algorithm for Least-Squares Estimation of Nonlinear Parameters”. In: *Journal of the Society for Industrial and Applied Mathematics* 11.2 (1963), pp. 431–441. DOI: 10.1137/0111030.

[149] GEP Box and ME Mueller. “A Note on the Generation of Random Normal Deviates”. In: *The Annals of Mathematical Statistics* 29.2 (1958), pp. 610–611.

[150] JW Zwolak, PT Boggs, and LT Watson. “Algorithm 869: ODRPACK95: A Weighted Orthogonal Distance Regression Code with Bound Constraints”. In: *ACM Transactions on Mathematical Software* 33.4 (2007), p. 12. DOI: 10.1145/1268776.1268782.

[151] OriginLab Corporation. *Nonlinear Implicit Curve Fitting*. URL: https://www.originlab.com/doc/Origin-Help/Fitting-Implicit (visited on 10/21/2016).

[152] AP Dempster, NM Laird, and DB Rubin. “Maximum likelihood from incomplete data via the EM algorithm”. In: *J Roy Stat Soc Ser B* 39.1 (1977), pp. 1–38.

[153] Mathworks. *Introduction to Cluster Analysis*. 2016. URL: https://de.mathworks.com/help/stats/introduction-to-cluster-analysis.html (visited on 10/21/2016).